universität wien

DISSERTATION | DOCTORAL THESIS

Titel | Title

Development of combinatorially-multiplexed DNA-PAINT and application to super-resolved RNA-FISH imaging

verfasst von | submitted by

Dott. Dott.mag. Alessandro Passera

angestrebter akademischer Grad | in partial fulfilment of the requirements for the degree of

Doctor of Philosophy (PhD)

Wien | Vienna, 2026

Studienkennzahl lt. Studienblatt | Degree programme code as it appears on the student record sheet:	UA 794 620 490
Dissertationsgebiet lt. Studienblatt | Field of study as it appears on the student record sheet:	Molekulare Biologie
Betreut von | Supervisor:	Dr. Francisco Balzarotti

Acknowledgements

There are many I want to acknowledge for making my journey possible and little space. First, I need to thank Francisco for his mentoring and supervision in the project. I was the first biologist to join the lab, and in spite of our different background, I found in him a kindred mind and as much desire to learn as to teach, which meant a great and prideworthy amount of faith in me, which meant much power over my goals while having a supportive figure throughout.

A thank you also goes to Clemens Plaschka and Ralf Jungamann, my other TAC members. While having a leader in the field of mRNA biology and the creator of DNA-PAINT observe my work demands some nervousness, I only found support and direction, which is a blessing.

I want to also thank the entirety of the Balzarotti lab, past and present, and especially Paul and Alba, who show that working with another is better than just having two more hands and one more brain, and who are beautiful friends. An individual thank you goes to Belén, as we leaned on each other for some of the hardest parts of our journeys.

As I keep expanding the scope of my thanks, a thank you goes to the VBC and its inhabitants. When I look forward to the next step of my journey, I look back at what I had in Vienna, and many things either do not compare, or will just not be the same. What there is at the VBC is unique in many aspects, and I can only hope its spirit of cohesion, sharing and community will expand to the rest of academia. A special thanks to the Amateur Dramatic Club, where I discovered I love to act, and where I discovered another love, Laura, and that ultimately led me to live with two cats, who I also love.

And after expanding my scope, I want to restrict it and leave my last thanks to my family. We are a small family, just the three of us, and I can only imagine how it feels to have your son far away, miss many important moments, and see him often at his worst. I can only thank you for the unconditional love which only family can, but now always does, give. And you have given it and, now and always, I want to give back to you some of my best.

Contribution statement

All contributions to the works in this thesis are listed in the “Contributions” section before each work, which is a copy of the one in the manuscripts.

The Zusammenfassung was generated using DeepL as per university guidelines for non-German speakers.

Table of contents

Abstract

Messenger RNA (mRNA) is a biological polymer of central importance for cell biology, as it transfers information from DNA in the nucleus to the protein-making machinery in the cytoplasm. It is established that mRNA forms complexes called ribonucleoprotein (RNP) particles together with numerous protein partners and that the specific composition of mRNPs has profound consequences on mRNA's stability, nuclear transport, export, and translation. However, for all that is known on the structure and role of the protein component of mRNPs, little is known on the ultrastructure of the mRNA they contain.

In this thesis, I provide tools for multiplexed optical nanoscopy, especially in low signal-to-background (SBR) scenarios, like the cell nucleus, and apply them to the imaging of cellular mRNA. To do this, I first contribute to developing and validating an improved MINFLUX microscope, which among other things is particularly adept at low SBR imaging. I then show the development of a multiplexing method based on combinations of signals to perform high-target number DNA-PAINT imaging. Using this method, a lower number of imaging steps is required to image a given number of targets compared to conventional DNA-PAINT, speeding up and simplifying imaging. Combining optimized RNA fluorescence in situ hybridization (RNA-FISH) with combinatorial DNA-PAINT, I show the multiplexed imaging of multiple regions of several mRNAs of interest in mammalian cells, extracting geometric features of these particles in the nucleus and cytoplasm. mRNAs appear to be compacted in an intron density-dependent manner in the nucleus, and they overall assume elongated and often non-convex shapes. Finally, I use the MINFLUX microscope previously developed to obtain the first 3D MINFLUX RNA-FISH images of nuclear and cytoplasmic mRNAs.

These tools allow the study of mRNA ultrastructure in particular and simplify multiplexed DNA-PAINT imaging in general — advances I hope will be adopted by the imaging community.

Zusammenfassung

Messenger-RNA (mRNA) ist ein biologisches Polymer von zentraler Bedeutung für die Zellbiologie, da es Informationen von der DNA im Zellkern an die Proteinproduktionsmaschinerie im Zytoplasma weiterleitet. Es ist bekannt, dass mRNA zusammen mit zahlreichen Proteinpartnern Komplexe bildet, die als Ribonukleoprotein (RNP)-Partikel bezeichnet werden, und dass die spezifische Zusammensetzung von mRNPs tiefgreifende Auswirkungen auf die Stabilität, den Transport im Zellkern, den Export und die Translation von mRNA hat. Trotz aller Erkenntnisse über die Struktur und Rolle der Proteinkomponente von mRNPs ist über die Ultrastruktur der darin enthaltenen mRNA nur wenig bekannt.

In dieser Arbeit stelle ich Werkzeuge für die multiplexierte optische Nanoskopie vor, insbesondere für Szenarien mit niedrigem Signal-Hintergrund-Verhältnis (SBR), wie z. B. im Zellkern, und wende sie auf die Bildgebung von zellulärer mRNA an. Dazu trage ich zunächst zur Entwicklung und Validierung eines verbesserten MINFLUX-Mikroskops bei, das unter anderem besonders für die Bildgebung mit niedrigem SBR geeignet ist. Anschließend zeige ich die Entwicklung einer Multiplexing-Methode, die auf Signalkombinationen basiert, um eine DNA-PAINT-Bildgebung mit hoher Zielanzahl durchzuführen. Mit dieser Methode sind im Vergleich zu herkömmlichem DNA-PAINT weniger Bildgebungsschritte erforderlich, um eine bestimmte Anzahl von Zielen abzubilden, was die Bildgebung beschleunigt und vereinfacht. Durch die Kombination von optimierter RNA-Fluoreszenz-in-situ-Hybridisierung (RNA-FISH) mit kombinatorischem DNA-PAINT zeige ich die multiplexe Bildgebung mehrerer Regionen mehrerer mRNAs von Interesse in Säugetierzellen und extrahiere geometrische Merkmale dieser Partikel im Zellkern und Zytoplasma. mRNAs scheinen im Zellkern in Abhängigkeit von der Intron-Dichte verdichtet zu sein und nehmen insgesamt längliche und oft nicht-konvexe Formen an. Schließlich verwende ich das zuvor entwickelte MINFLUX-Mikroskop, um die ersten 3D-MINFLUX-RNA-FISH-Bilder von nukleären und zytoplasmatischen mRNAs zu erhalten.

Diese Werkzeuge ermöglichen insbesondere die Untersuchung der mRNA-Ultrastruktur und vereinfachen allgemein die multiplexe DNA-PAINT-Bildgebung – Fortschritte, von denen ich hoffe, dass sie von der Bildgebungsgemeinschaft übernommen werden.

1 Introduction

1.1 Super-resolution microscopy

The first concepts of super-resolution microscopy were published at the very end of the 20th century (Betzig, 1995; Hell & Wichmann, 1994) and relied on STimulated Emission Depletion (STED) to shrink the spatial size of the Point Spread Function (PSF) of a scanning microscope, or on inducing emitter sparsity in the sample to enable precise localization under the assumption that the observed PSFs belong each to a single emitter, providing the framework for Single-Molecule Localization Microscopy (SMLM). On the one end, these works theorized something unique, imaging which broke the diffraction limit of light, a fundamental barrier to the discrimination of two point sources closer to each other than approximately half of the wavelength of light they emit. On the practical side, these approaches promised to revolutionize biological imaging, as many of the cell's most interesting features, such as cytoskeletal structures, large protein complexes, or vesicular bodies all lie below this limit, requiring electron microscopy for their study. The first experimental demonstrations of the techniques used fluorescence as the source of photons (Betzig et al., 2006; Hess et al., 2006; Klar & Hell, 1999; Rust et al., 2006), and given the strengths of organic fluorophores and fluorescent proteins (small, biocompatible, efficient emitters that can selectively label biological structures of interest), it has remained the prevalent version of the techniques in biology. STED evolved into a powerful confocal point-scanning technique and became widely adopted through successful commercial implementations of the concept. SMLM, due to its inherently lower time resolution (usually zero, due to its reliance on chemical fixation of the samples), but practically better localization precision, became the technique of choice for highest-resolution imaging. SMLM later received improvements in terms of 3D capabilities through PSF engineering (Huang et al., 2008) and multi-color imaging through ratiometric detection of fluorophore identity (Bossi et al., 2008), which overall allowed the imaging of samples previously intractable with diffraction-limited microscopy (Liu et al., 2022). Given its contributions to our understanding of cellular structures, the field of super-resolution was awarded the Nobel prize for Chemistry in 2014.

1.1.1 DNA-PAINT

SMLM techniques require three features:

1. Emitters must be able to transition (ideally reversibly) between two states, emitting ("on") and non-emitting ("off), a feature called "blinking". The length of these states is t_{on} and t_{off}, respectively;
2. The blinking duty cycle, t_{on}/t_{off}, should be <1 and lower the higher the concentration of emitter to prevent blinking events from overlapping;
3. The sampling technique (for example, and commonly, a camera) should allow the sampling time to be shorter than the length of the emitting state.

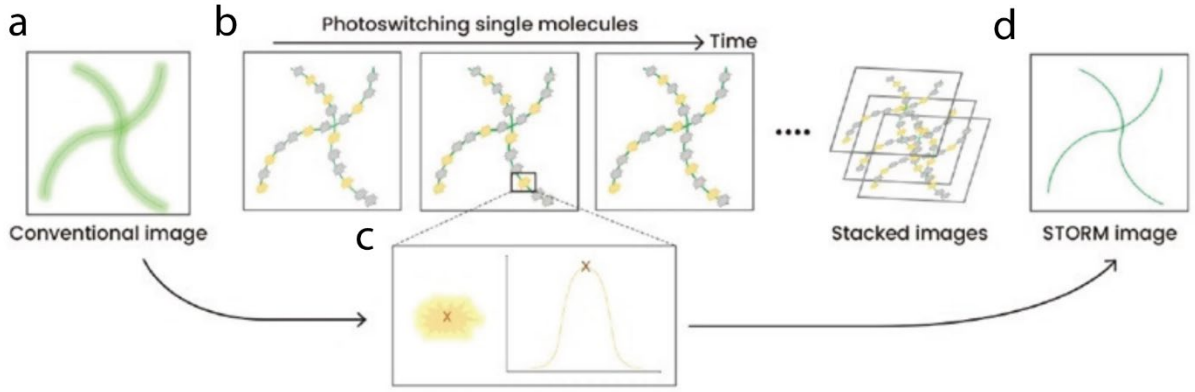

Figure 1: SMLM principle. (A): a conventional, diffraction-limited picture of filamentous structures. (B): the majority of emitters transitions to a non-emitting state, with only a small, sparse subset emitting. The signal of each isolated emitter can then be fitted to a gaussian function model (C) to accurately extract the position of the emitter. This is repeated over many frames, with imaged emitters transitioning to the non-emitting state, and different emitters transitioning to the emitting state. The final image (D), reconstructed from a movie of frames, has a higher spatial resolition than the conventional image. Adapted from Hyun et al., 2022 (Int. J. Mol. Sci. 2022, 23(13), 6896).

If these conditions are met, each sampling point, such as a camera frame, will show a sparse subset of the emitters in the emitting state. This allows precise PSF localization through, most commonly, fitting the signal to a gaussian function. These emitters will transition to the non-emitting state after a characteristic time, while others will "appear" as they transition to the emitting state. Other frames will therefore show different subsets of the emitters, allowing the reconstruction, in a way often paralleled to pointillism, of an image from a movie of blinking emitters (Figure 1).

Several techniques, like STochastic Optical Reconstruction Microscopy (STORM) (Rust et al., 2006), PhotoActivation Localization Microscopy (PALM) (Betzig et al., 2006) or SMLM based on self-blinking dyes (Uno et al., 2014) rely on intrinsic (photo)chemical properties of the fluorophore for blinking: the fluorophore is able to transition between the emitting and non-emitting states, intrinsically or through photochemistry, or can be photoactivated from a dark state and subsequently

bleached. Another technique, Point Accumulation In Nanoscale Topography (PAINT) (Sharonov & Hochstrasser, 2006), relies instead on constantly-emitting fluorophores that can reversibly bind to the structure or target of interest. Concretely, light is emitted from the binding site only when the fluorophore is bound to it. Diffusing probes will be too fast to show as blinking events on the camera, generating instead fluorescence background. This strategy has many advantages over photochemical control of the emitter: 1) any fluorophore can be used, not only photoactivatable or photoswitchable ones, allowing the brightest dyes to be harnessed, or dyes with useful properties like distinguishable emission spectra or fluorescence lifetimes; 2) binding events persist as long as the binding site is not damaged, allowing virtually unlimited sampling of the target of interest; 3) if multiple binders targeting different structures are available, they can all be conjugated to the same fluorophore, enabling “multicolor” imaging simply by exchanging which binder is present in solution, avoiding the use of suboptimal fluorophores and completely abolishing chromatic aberration; 4) dense samples become tractable by reducing the concentration of the binder accordingly. In contrast, the duty cycle of photochemically-switching emitters might simply not allow the spatial sparsity necessary for SMLM. However, PAINT still has limitations: 1) the kinetics of binding dictate the length of the experiment, possibly resulting in long imaging times; 2) there is reliance on a liquid environment for imaging; 3) high fluorescence background is generated by the diffusing binder, which requires optical sectioning techniques such as Total Internal Reflection Fluorescence (TIRF) or confocal detection.

The development that allowed the PAINT concept to truly flourish is DNA-PAINT (Jungmann et al., 2010), which uses short DNA strands as the reversible binders necessary for PAINT (Figure 2a). This adds many beneficial properties to the one already mentioned for PAINT: 1) binding is now programmable, and different DNA sequences can be used to avoid crosstalk and generate a high number of orthogonal pairs (Jungmann et al., 2014) (Figure 2a); 2) DNA sequences can be changed to improve the kinetics of binding (Schueder et al., 2019); 3) stable, efficient binders can now be conjugated to DNA strands and used to label biological targets of interest, as the reversibility of binding has been outsourced to the DNA (Schlichthaerle et al., 2019). Over the years, DNA-PAINT was further improved, shortening imaging time by two orders of magnitude compared to its inception (Strauss & Jungmann, 2020), using

clustering of localizations to achieve sub-nanometer localization precision in cells (Reinhardt et al., 2023) and using intermediate adapters to achieve high-degree multiplexing (Schueder et al., 2024; Unterauer et al., 2024) (Figure 2b).

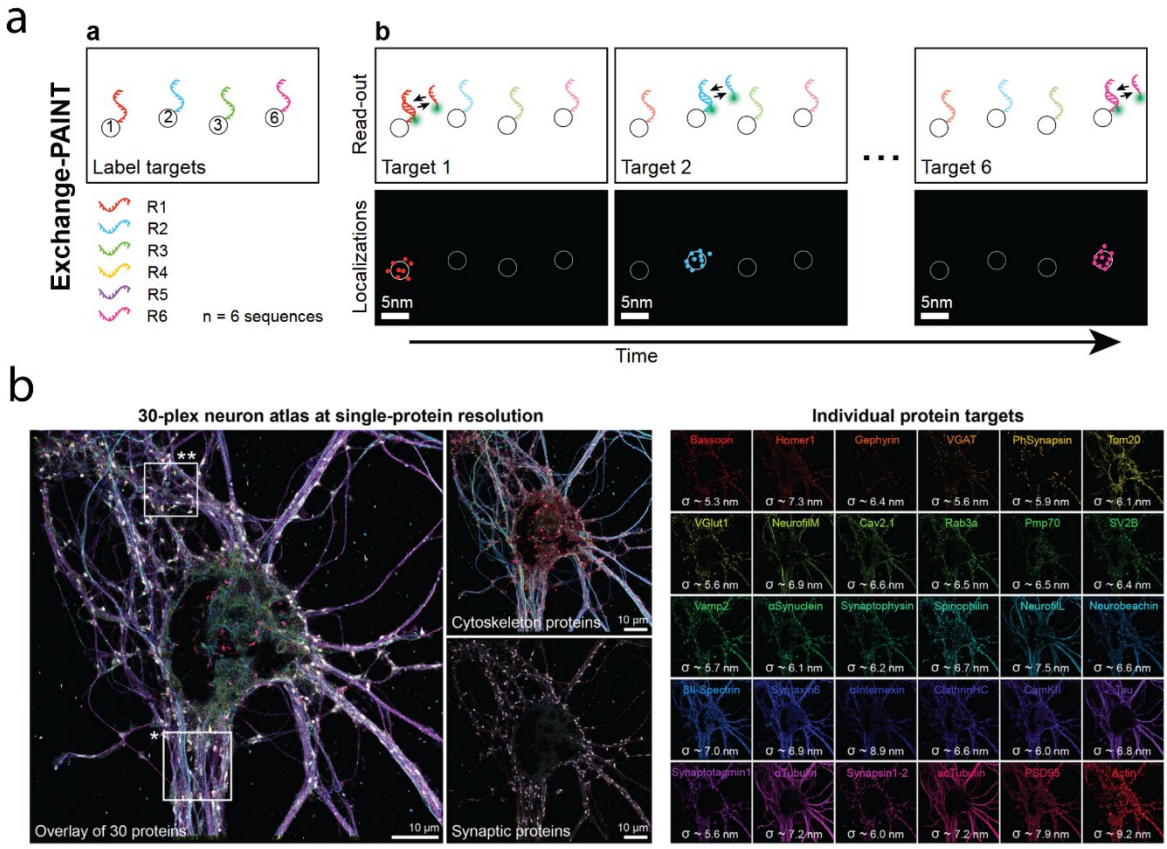

Figure 2: DNA-PAINT. (A): DNA-PAINT principle of reversible DNA binding, and Exchange-PAINT explanation. Buffer exchanges are performed between infividual imaging rounds. From Steen et al., 2026 (bioRxiv 2026.01.23.701249). (B): a recent, advanced use of DNA-PAINT multiplexing through intermediate adapters, used for 30-colour DNA-PAINT with uniform performance across rounds in neurons. Excerpt from Unterauer et al., 2024.

1.1.2 MINFLUX

SMLM requires control over the emission state of fluorophores. However, how these fluorophores are illuminated and detected is up to the experiment designer. Several strategies that go beyond the combination of uniform widefield illumination with camera detection used in the first demonstrations of SMLM have been reported, including structured illumination (Cnossen et al., 2020) and spinning disk confocal (Schueder et al., 2017; Zaza et al., 2025) as well as SPAD arrays (Antolovic et al., 2017) to name a few. A technique which combines structured illumination and confocal detection is MINFLUX (Balzarotti et al., 2017). In this technique, a single emitter is probed with a focused beam featuring a zero of intensity, such as a vortex beam or a

top hat beam (Gwosch et al., 2020), which is displaced following a constrained pattern in two or three dimensions around the emitter. Here, the emitted photons by the fluorophore are collected via confocal detection for each position of the excitation beam in said pattern, and a mathematical model is applied to estimate the location of the fluorophore (Figure 3a).

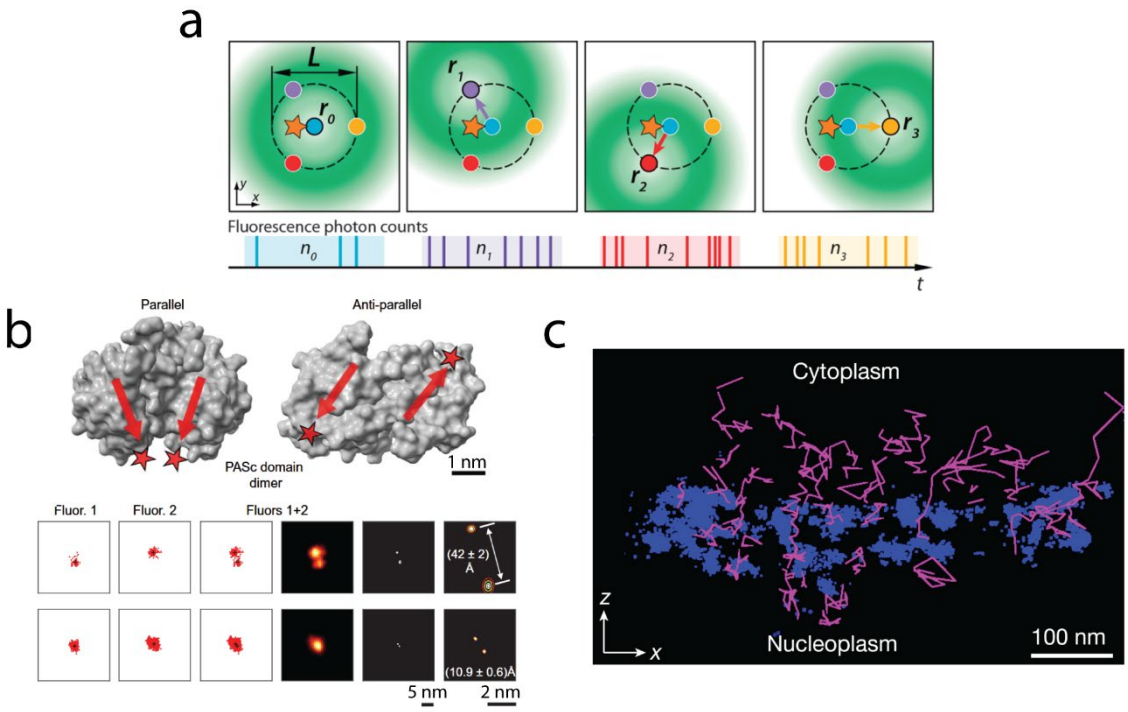

Figure 3: MINFLUX. (A): diagram of MINFLUX excitation. (B): MINFLUX PALM imaging of 2D-projected intramolecular distance of in vitro PASc dimers, predicted to be 1 or 4 nm depending on monomer orientation. Excerpt from Sahl et al., 2023 (bioRxiv 2023.07.07.548133), in which scale bars have been labelled with the length reported in the caption of the figure. (C): Advanced MINFLUX co-imaging of the nuclear pore complex (blue) and tracking of importin α (pink) at sub-millisecond time resolution. Exceprt from Sau et al., 2025.

Remarkably, the closer the center of the pattern is to the location of the fluorophore and the smaller the pattern, the more informative the collected photons will be, allowing to achieve single-nanometer localization precision with ~20 times less photons than necessary for camera-based localization. For the purpose of imaging, this is ensured by iteratively using a few photons to localize the fluorophore, deflecting the pattern to the estimated position and simultaneously reducing its size, then using some more photons to improve the estimation, and so on several times to converge onto the fluorophore in a process called iterative MINFLUX (Gwosch et al., 2020). MINFLUX fundamentally breaks the equation for localization precision by removing the dependence on the emission wavelength and replacing it with a dependence on the pattern size, which the experimenter can reduce as desired to achieve higher

precision. Given its photon efficiency, since its first demonstration, the MINFLUX concept has been used for both extremely high precision imaging (Sahl et al., 2023) (Figure 3b) as well as single-particle tracking at unprecedented spatio-temporal resolution (Deguchi et al., 2023; Eilers et al., 2018; Wolff et al., 2023) and has established itself as a powerful technique capable of imaging processes otherwise difficult to capture (Sau et al., 2025) (Figure 3c). Currently, MINFLUX is limited in its applicability by its confocal scanning nature, which limits its throughput, and fluorescence background, which limits the range of samples and techniques to which it can be effectively applied.

1.2 Messenger RNA

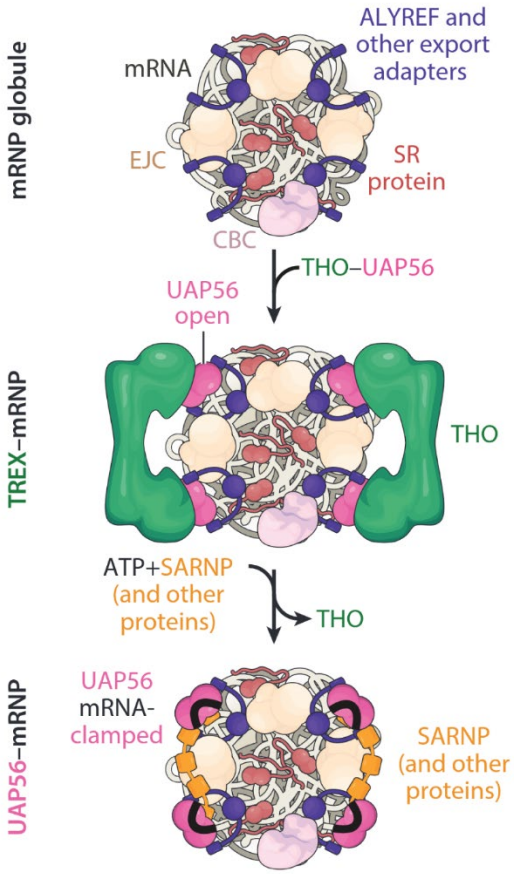

Figure 4: Steps of mRNA processing and packaging most relevant for this work. Adapted from Faraway et al., 2025. Abbreviations are explained in the text.

Messenger RNA (mRNA) is the protagonist of the transfer of information between DNA and protein. In eukaryotic cells, in which DNA is stored in the nucleus, mRNA is transcribed from DNA by RNA polymerase II. The transcript then undergoes several maturation and packaging steps (capping, splicing and poly-adenylation) and is exported through the nuclear pore complex into the cytoplasm, where it is finally read by ribosomes which synthesize the protein encoded by the mRNA (Faraway et al., 2025). mRNA is then eventually degraded to regulate its amount, together with modulation of transcription level. mRNA is never found as truly naked ribonucleic acid since, as it undergoes its maturation steps, it has several protein maturation marks deposited onto it to form ribonucleoprotein (RNP) particles (Singh et al., 2015) (Figure 4). From the 5' end to the 3' end of mRNA, one can find the Cap-Binding Complex (CBC), a variable number of Exon Junction Complexes (EJC) and the polyA-binding

protein (PABPN1), in addition to and sometimes through which the TRansport and EXport (TREX) complex (Pacheco-Fiallos et al., 2023), SR proteins (Long & Caceres, 2008), hnRNPs (Geuens et al., 2016) and numerous other proteins bind. The reasons for the presence of these protein partners are multiple: mRNA needs to be marked as mature and therefore ready for export after processing events take place; mRNA needs to be protected from premature degradation; and finally, mRNA needs to be compacted. While entropy would already greatly reduce the average mature human mRNA outstretched length of ~2 μm (~3.5 kb, see Results chapter), the problem of moving mRNA through the chromatin-containing nucleus would still be akin to moving a flexible polymer through a net or sponge, which raises the question of how is mRNA compacted to prevent tangling with chromatin and other RNA, exposure to premature degradation, and formation of biologically harmful hybrids with DNA (Domínguez-Sánchez et al., 2011).

1.2.1 Imaging mRNPs

The study of the structure and composition of mRNPs can be summarized as one of three approaches: structural, sequencing-based, and imaging-based.

Structural methods rely on the combination of structural biology techniques, like cryo-electron microscopy (cryo-EM) or cryo-electron tomography (cryo-ET) to study the protein components of mRNPs and biochemistry methods to confirm insights obtained from these techniques (Bonneau et al., 2023; Pacheco-Fiallos et al., 2023; Pühringer et al., 2020) (Figure 5a). While these approaches are undeniably powerful, providing structural insights and information about interaction surfaces, which can then be validated through mutational studies and other biochemical techniques, they are strongly geared towards the study of the protein components of mRNPs. Even when imaging native mRNPs extracted from cells (Bonneau et al., 2023; Pacheco-Fiallos et al., 2023), RNA is not discernible from proteins in individual micrographs and is averaged to a featureless density by EM processing. Furthermore, since these approaches extract mRNPs indiscriminately (by pulling, for instance, on THO complex components), these particles are heterogeneous, meaning it is unclear whether the heterogeneity observed in EM is due to each transcript species adopting a different ultrastructure in each of its mRNPs, or due to different transcript species giving rise to different mRNPs.

Sequencing-based approaches use RNA chemical modification and/or ligation followed by sequencing to study RNA-RNA and protein-RNA interactions in cells (Metkar et al., 2018; Wang et al., 2024; Watts et al., 2009; Wu et al., 2024) (Figure 5b). These approaches are powerful, allowing the study of relevant RNAs like the HIV genome, virus-host RNA-RNA interactions, the homogeneity of the structure of RNAs at different developmental stages and the estimation of the shape type (e.g., globular versus elongated) of mRNA. However, these approaches do not return spatial positions and structures of individual mRNPs, and since particles are extracted from cells, they lack information about the cellular context of mRNA beyond a possible nuclear fractionation (Wu et al., 2024).

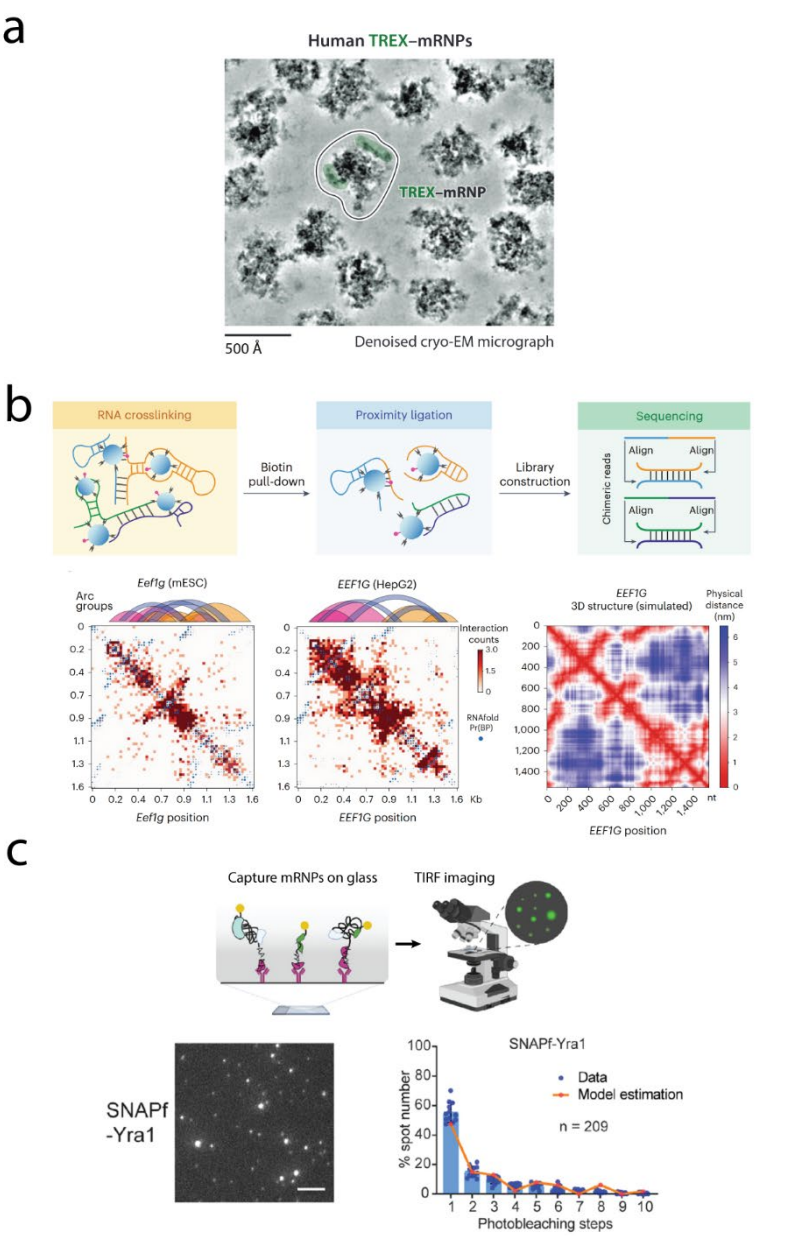

Figure 5: mRNP imaging. (A): structural approach, where cryo-EM was used to extract the structure of the TREX complex from native mRNPs. mRNA structure, however, is not possible to extract by averaging of this heterogeneous sample. Adapted from Faraway et al., 2025. (B): sequencing-based approach. Intramolecular contacts for the EEF1G mRNA are measured by RNA crosslinking and sequencing, showing good agreement across cell lines and with predicted 3D structure. Adapted from Wu et al., 2024 (C): imaging-based approaches. mRNP proteins (the yeast ALYREF analog Yra1 in this example) are fluorescently labelled, mRNPs are immobilized on glass and imaged. The number of photobleaching steps can be used to infer the stoichiometry of the labelled protein. Adapted from Asada et al., 2023.

Imaging-based approaches have attempted to use the specificity of genetic tagging and fluorescent labelling to tackle the question of the stoichiometry of the protein components of mRNPs (Asada et al., 2023). This approach provides valuable

information for assessing models of mRNP architecture, but misses on providing localization information. Therefore, by being blind to the relative arrangement of proteins with respect to each other, it lacks transcript identity information, similarly to structural methods, and once again does not provide the cellular context of mRNPs.

1.2.2 Imaging mRNA

To probe the mRNA component of mRNPs, a different type of labelling and imaging technique is necessary. For decades, the technique of choice has been mRNA Fluorescence In Situ Hybridization (mRNA-FISH), in which short (20-40 nt) single-stranded DNA probes are designed to target the sequence of a given RNA specifically (Femino et al., 1998; Singer & Ward, 1982; Young et al., 2020).

Typically, the probes are labelled fluorescently, allowing the user to obtain diffraction-limited spots as the imaging readout once this mix of probes is applied to a cell or tissue sample and several of them bind each mRNA molecule. More recently, there have been attempts at labelling different regions of a given mRNA with different colors, allowing the measurement of distances between the centers of mass of these regions (Adivarahan et al., 2018; Asada et al., 2023; Wu et al., 2024) (Figure 6a). These measurements have been interpreted as a readout of the overall size of the mRNP, providing for example insight into the state of compaction of mRNPs before and after nuclear export or translation. However, it is not currently known what exactly regulates the distance and arrangements of the various segments of mRNA, making this readout, while informative, a proxy of mRNA ultrastructure.

Super-resolution has been, on several occasions, applied to RNA/mRNA imaging. The tendency, however, has been for it to be used as a tool to increase the resolution, and therefore separability, of densely expressed mRNAs or small RNAs (Huang et al., 2020; Schueder et al., 2017) (Figure 6b), to increase the precision of colocalization studies (Stoldt et al., 2025) (Figure 6c) and in one case to extract shape parameters of paraspeckles, a long non-coding RNA/protein condensate (Berrevoets et al., 2025). No attempt to individually label different segments of mRNA, and subsequently super-

resolve it to extract the ultrastructure of single mRNAs in cells has been done to date, to the best of my knowledge, and is ultimately the goal of this work.

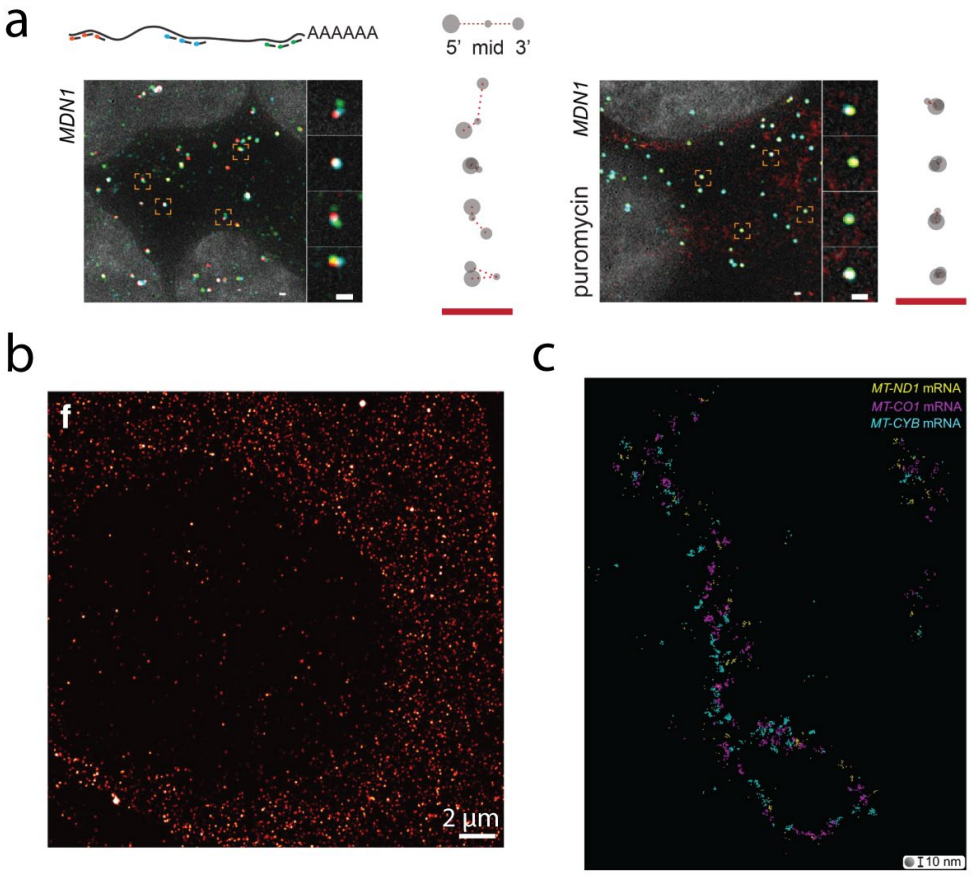

Figure 6: RNA imaging examples. (A): multicolor SIM imaging of the MDN1 mRNA. Multiple areas of the MDN1 mRNA are labelled, and a strong collapse of mRNA is shown upon translation inhibition. All scale bars are 500 nm. Adapted from Adivarahan et al., 2018. (B): spinning-disk confocal DNA-PAINT imaging of the CBX5 mRNA. Diffraction-limited imaging would result in major overlap between single mRNPs signal given the high mRNA density. Exceprt from Schueder et al., 2017, in which the scalebar was labelled with the length reported in the caption of the figure. (C): 3D MINFLUX DNA-PAINT imaging of three mitochondrial mRNAs. The enhanced resolution allows more precise colocalization measurement. Excerpt from Stoldt et al., 2025.

1.3 Outline of my PhD

1.3.1 Goals

I. Contribute to developing a MINFLUX microscope which is, among other things, more suited to operating at high fluorescence background

II. Deepen my practical knowledge of microscopy by building a custom 3D widefield microscope for super-resolution microscopy and maintaining the developed MINFLUX microscope

III. Develop a combinatorial DNA-PAINT multiplexing strategy to speed up imaging and minimize sample perturbation

IV. Employ the two techniques, MINFLUX and DNA-PAINT, in conjunction to perform super-resolved imaging of native mRNA structure at sub-transcript sequence resolution

One of the goals of my PhD is to become a proficient microscope scientist, not only by acquiring knowledge of different imaging techniques, but also from a practical point of view, gaining knowledge of the theory and workings of a microscope. This is a common thread between papers, with the first being focused on a new MINFLUX microscope, which I contribute to benchmarking through the generation of DNA origami samples and become a user and maintainer of, and the second paper featuring a self-built widefield super-resolution microscope. Another goal of my PhD is to bring the combinatorial DNA-PAINT idea from the early conception stage through the feasibility, development, testing, and advanced application stages. This idea is described in the second paper and further elaborated on in the Discussion. The application is the last goal of my PhD, with the choice of mRNA as a target being well-informed both from a biological, given its novelty, and technical perspective.

Over the course of my PhD, I approached both widefield as well as confocal microscopy techniques. The first has been through the building from scratch of a custom widefield super-resolution microscope meant to provide better performance than the commercial options available to us. The custom microscope is capable of TIRF operation, has a cylindrical lens doublet for 3D imaging via astigmatism, features an input/output board for controlling its electronic devices and has an uncommon infrared module capable of sub-millisecond, sub-nanometer stabilization in all three dimensions. The microscope was designed, built, aligned, and calibrated entirely by me, and provided a unique opportunity of learning about widefield microscopy.

Confocal, or more specifically MINFLUX, microscopy knowledge was acquired through our custom MINFLUX microscope, dubbed MINFLUX 3 (MF3). The system is detailed in the first paper and provides a notable improvement over current MINFLUX microscope designs by having an interferometric scanner implemented through a double pass on a spatial light modulator (SLM). This allows axial scanning of the top hat (also called bottle) beam zero of intensity, used for 3D MINFLUX imaging, as well as more general movements of the zero of intensity of various beam shapes. Compared to previous options for axial beam deflection in MINFLUX, like electro-

optical lenses or deformable mirrors, the interferometric approach is cheaper, one order of magnitude faster, and less complex. Due to having multiple beam paths that hit the SLM in different areas, MF3 is also capable of mixing beam shapes and physical colors in the same cycle of beam exposures, which translates into a better localization precision, isotropicity and robustness (by using shapes that are optimal for certain tasks, like donut beams for in-plane localization and top hat beams for axial localization), as well as the capability of dual-color tracking by alternating 561 and 643 nm excitation.

Over the course of my PhD, I started by providing the *in vitro* samples necessary to assess the performance of MF3, both for imaging and tracking. These are DNA origami samples (Rothemund, 2006; Schmied et al., 2014) for STORM or DNA-PAINT imaging, as well as more unique designs with a flexible, single-stranded DNA extension with a fluorophore at the end, capable of binding short docking strands on the DNA origami and act as a programmable moving dye for tracking. Multiple such extensions can also be added in an orthogonal manner for multi-emitter tracking. The origami has several biotin-modified oligonucleotides to allow immobilization on a neutravidin-coated coverslip. The initial design was that of a commonly-used, single-layered breadboard (Schmied et al., 2014; Schnitzbauer et al., 2017) for 2D samples, but made in-house for flexibility. Later, I also designed and produced a 3D origami composed of 32 parallel DNA helices (32-helix bundle) which can be robustly immobilized on one of its sides, providing a sample for imaging and tracking in the axial direction. Later in my PhD, I became a user of MF3 for imaging, but also a maintainer. MF3 is a prototype microscope, and as such it requires more hands-on time than a commercial microscope, which is more monolithic, as well as containing more self-aligning and automatically aligning parts. This comes in the form of, typically, a weekly check and adjustment of several optical alignments, and a daily check of a few parameters like beam alignment at the nanometer level and automated optimization of the interferometric scanner parameters. I also performed full-system alignments, which required and tested knowledge of the entire system.

The core of my PhD was the development of a combinatorial multiplexing strategy for DNA-PAINT multi-target imaging, which is described in the second paper. Initially conceived to work with fluorogenic, partially-mismatching DNA-PAINT imager strands (Chung et al., 2022), I eventually expanded the framework to also work with

conventional, speed-optimized strands. The concept is mathematically described in the Supplementary Note of the paper but can be summarized as the encoding of additional DNA-PAINT targets as combinations of signals from individual imagers. This can be a binary encoding, or it can be a stoichiometric encoding, where targets share the same combination of imager signals, but with different expected amounts of signals from each imager. The benefits of such a strategy are several: less washing steps are necessary if doing Exchange-PAINT, which cuts down on time and experiment complexity; since colocalization of fluorescence signals at the molecular level is expected, this can be exploited when designing the experiment to reject single-imager signal, which is more likely to originate from unspecific binding; spectral unmixing, (Gimber et al., 2022), for which MINFLUX proof-of-principle experiments have been run, or fluorescence lifetime (Oleksiievets et al., 2022) can be used to distinguish fluorophores and allow washless multiplexed imaging, reducing microscope instability and drift as well as allowing imaging samples for which washes are complex or impossible, such as thick samples or 4Pi microscopy coverslip sandwiches.

Finally, I show the use of combinatorial multiplexing on a biologically relevant sample by performing (MINFLUX) DNA-PAINT mRNA-FISH imaging in cells. mRNA provides a perfect sample for combinatorial DNA-PAINT: mRNA has not been imaged at the nanoscale, ultrastructure level, unlike proteins (Shaib et al., 2022; Unterauer et al., 2024) and DNA (Beckwith et al., 2025; Sasaki et al., 2022), making it interesting and novel. Moreover, RNA-FISH allows the introduction of many DNA-PAINT targets in the same sample by decorating subsets of RNA-FISH probes with different DNA-PAINT extensions, making it a very suitable choice from the technical point of view as well. MINFLUX imaging was performed to provide a high-quality, isotropic 3D view of mRNA, which was expected to be approximately globular, randomly oriented in space, and between 30 and 70 nm in size (Pacheco-Fiallos et al., 2023), while widefield imaging provided the throughput to extract relevant parameters from many mRNPs. Combinatorial DNA-PAINT provides welcome benefits, simplifying an already complex imaging pipeline and minimizing the number of washing steps and therefore MINFLUX drift.

2 Results

2.1 A Fast Interferometric Beam Shaper for Multi-Emitter 3D MINFLUX

Authors: Maximilian K. Geismann*, Alba Gomez-Segalas*, Alessandro Passera, Mehrta Shirzadian, Francisco Balzarotti

*Authors contributed equally

Contributions: MKG, AG and FB designed and built the optical system, and programmed the hardware control. MKG, AG, AP, MS and FB programmed the processing and visualization software. MKG and AG performed experiments and data analysis. AP designed and folded DNA origami and optimized used protocols. AP prepared and optimized cell samples. MS performed simulations and optimizations. MKG, AG, AP and FB wrote the manuscript. FB supervised the project.

Relevance: The paper describes the MINFLUX microscope used for mRNP imaging, which requires familiarity on both the hardware and software level for proper usage. It was my initial use of DNA origami, later used extensively for characterization of the combinatorial DNA-PAINT technique. Finally, it constitutes an essential step in my formation as a microscopist, which I later employed when designing and building a custom super-resolution microscope, as well as during the improvement of the MINFLUX microscope for low-SBR RNA-FISH DNA-PAINT imaging.

Status: Published on bioRxiv on 15.02.2024

A Fast Interferometric Beam Shaper for Multi-Emitter 3D MINFLUX

Maximilian K. Geismann[1,2]*, Alba Gomez-Segalas[1,2]*, Alessandro Passera[1,2], Mehrta Shirzadian[1,2], Francisco Balzarotti[1,#]

[1]Research Institute of Molecular Pathology (IMP), Vienna BioCenter (VBC), Campus-Vienna-Biocenter 1, 1030 Vienna, Austria.

[2]Vienna BioCenter PhD Program, Doctoral School of the University of Vienna and Medical University of Vienna, A-1030, Vienna, Austria

*Equal contribution

[#]Corresponding author: francisco.balzarotti@imp.ac.at

Abstract

Beams of light that feature an intensity zero are essential to a variety of optical microscopy methods. Super-resolution techniques like STED and RESOLFT, together with localization strategies like MINFLUX and MINSTED, rely on accurate and fast displacements of such beams and their zeros. Extending these methods to the third dimension requires axial deflection, which, in contrast to lateral deflection, remains technologically challenging on the microsecond scale. Here, we present a fast general-purpose beam-shaping polarization interferometer that, instead of displacing the entire beam, enables such axial deflections by deforming the beam shape to deflect its zero. Based on this approach, we showcase a four-channel dual-color excitation system for three-dimensional MINFLUX imaging and tracking. We include first demonstrations of improved MINFLUX localization schemes that utilize the combination of distinct beam shapes and three-dimensional multi-emitter tracking. We believe that the presented approach will facilitate the broader adoption of three dimensional MINFLUX and provides a versatile basis for future implementations of advanced single-molecule localization methods.

Introduction (without heading)

Displacing and deforming beams of light in a controlled manner is integral to a wide range of methods such as optical tweezers and microscopes. Super-resolution fluorescence imaging techniques, such as STimulated Emission Depletion (STED)[1], and REversible Saturable Optical Linear Fluorescence Transitions (RESOLFT)[2,3], as well as localization strategies like Maximally INFormative LUminescence eXcitation (MINFLUX)[4] and MINSTED[5], require displacing beams that feature zeros of intensity. These zeros—that either constrain regions from which fluorescence can be emitted or generate a spatially variant signature—enable the precise assignment of a fluorophore's location with respect to a targeted coordinate.

MINFLUX[4] stands out as a single-molecule localization strategy, distinguished by its approach of sequentially probing the position of an emitter with different beam shapes. Its high localization efficiency—the number of emitted photons required to reach a given localization precision—has been harvested for stochastic super resolution imaging[6,7] and single-molecule tracking, reaching spatial and temporal resolutions in the nanometer[8] and sub-millisecond[9–11] scales. MINFLUX localizations in one-, two- and three-dimensions have been achieved through beams shaped by half-moon[10], vortex[4] and top-hat[8] phase masks. Even Gaussian beams[4] are efficient when used appropriately.

Irrespective of shape, the beams employed by the above methods require displacement. Available lateral scanning technologies include galvanometric, piezoelectric, electro-, and acousto-optic deflectors, while axial scanning technologies include electro-, acousto-optic, and liquid lenses. MINFLUX implementations have been based on electro-optical lateral deflection[4], as it is compact, achromatic, simple to use, and delivers sub-nanometer and sub-microsecond deflection. For axial deflection, previous implementations resorted to an electro-optically tunable lens[8]or a deformable mirror[12]. These devices come at an increased cost and exhibit more complexity than their lateral-deflection counterparts. The tunable lens has a limited focal length of down to one meter and a response in the order of 30 µs, limited by its high capacitance and the current provided by the driving high-voltage amplifier. Deformable mirrors, being micro-electro-mechanical devices, face similar speed constraints.

We present an interferometry-based strategy for fast beam shape manipulation where the coherent superposition of specific pairs of beams with different shapes results in displacements or tilts of point-, line- and plane-like zeros of intensity, making it attractive for super-resolution techniques such as STED and RESOLFT, localization techniques like MINFLUX and MINSTED, and optical tweezer applications. To realize this concept we developed and characterized a general-purpose four-channel polarization interferometer compatible with continuous-wave and pulsed beams. It is the key component facilitating 3D and two-color operation for imaging and tracking in the presented MINFLUX system and we believe it will make these features more accessible for future MINFLUX implementations. Furthermore, this technology enabled the first demonstrations of MINFLUX excitation schemes mixing distinct beam shapes for improved precision and concurrent two-emitter MINFLUX tracking in 3D, following the recent introduction of simultaneous two-emitter MINFLUX tracking in 2D[13]. These advancements pave the way for multi-emitter MINFLUX tracking as a method for studying the kinetics and conformational states of flexible protein complexes free from range limitations present in single-molecule FRET[14] and with time resolutions in the sub-millisecond range, surpassing high-speed AFM[15].

Results

Interferometric manipulation of an intensity zero point, line and plane

Regions of space where focused beams have no intensity exist as points, lines or planes and can be generated by distinct phase masks at the back focal plane of a lens. Near these locations with no intensity, the spatial dependence of the electric field and its polarization take a variety of forms. It is possible to manipulate the shape and location of these regions by interferometrically combining distinct beams, thus mapping their relative amplitudes and phases to spatial features. Figure 1 displays various simulated and measured beam combinations that displace and tilt zero-intensity regions (see methods, PSF simulation and measurement).

Several of these combinations are based on matching pairs of beams with linear and uniform electric fields, see Table 1. For example, a circularly polarized donut beam, created using a 2π vortex mask, features an axial zero line and a linearly dependent electric field across the xy plane that can be laterally displaced when combined with a circularly polarized Gaussian beam (Fig. 1a, Supplementary Fig. S1). As the donut beam contains all phases of electric field at any given time, there will always be a location where it destructively interferes with the Gaussian beam. That location is dictated by the relative amplitude and phase of the Gaussian beam, mapping them to physical polar coordinates[16] (Supplementary Fig. S2). A similar phenomenon occurs with a linearly polarized beam shaped by a half-moon phase mask, creating an axial zero plane that shifts laterally when paired with a linearly polarized Gaussian beam (Fig. 1b, Supplementary Fig. S3). When combining a charge-2 donut beam with a Gaussian beam (Fig. 1c, Supplementary Fig. S4), the axial zero line at the origin splits into two zero lines, opposite from each other, which are also mapped into polar coordinates by the relative phase and amplitude of the beams (Supplementary Fig. S5).

Furthermore, interferometric combinations that specifically alter the axial distribution within the beams can be engineered. For instance, the central zero point of a bottle beam can be axially shifted by combining it with a Gaussian beam (Fig. 1d, Supplementary Fig. S6), as the bottle beam is purely laterally polarized across the z-axis with a linear dependence on z. Other innovative combinations include tilting the axial zero line of a circularly polarized donut beam (Fig. 1e, Supplementary Fig. S7,Supplementary Fig. S8) and tilting the zero plane of a linearly polarized bi-lobed beam (Fig. 1f, Supplementary Fig. S9) when combining them with the bottle beam and its linear analogue the bottle-slice beam, respectively. See Table 2 for a list of the beam combinations presented.

However, beams focused with high numerical aperture contain axial electric fields[17], leading to a zero degradation if (i) the interferometric combination does not yield a null axial component or, if (ii) it does, but its location does not match the zero of the lateral components (see electric field profiles in Fig. 1a-g with zero mismatches marked by arrows). Additionally, a mismatch of Gouy phases, as in the case for the bottle beam and the Gaussian, degrades axially shifted zeros (Supplementary Fig. S10). Such degradation manifests in scenarios involving large displacements of the zero and depends on the numerical aperture of the system and fill factor of the beams.

Despite these circumstances, the interferometric shifting of zeros can imitate whole beam deflection for techniques, such as MINFLUX, where only the parabolic intensity distribution around a zero matters. It offers an enticing alternative to current technologies for implementing axial deflection as discussed in the following section.

A four-channel common-path beam-shaping polarization interferometer

We present an implementation of our interferometric beam shaping strategy with a system that is compact, modular, scalable, cost-efficient, flexible, and capable of dynamic manipulation. The system comprises three main blocks (Fig. 2a-c): a polarization rotator, a beam shaper, and a beam combiner that control the interference of two distinct beam shapes by modulating their relative amplitudes. In this two-color design, these components act on four independent paths, two per laser wavelength (Fig. 2d).

The first block, a polarization rotation module (Fig. 2a), allows us to change the relative amplitudes of the beams that will interfere. The rotator is comprised of an Electro-Optical Modulator (EOM) with its principal axis at 45° and an achromatic Quarter-Wave Plate (QWP) at 0°. For a linearly polarized Gaussian beam $E_0\vec{e}_x$ at the input, the output is a rotated linearly polarized state $E_1\vec{e}_x + E_2\vec{e}_y$ (shown in yellow and blue) with $E_1 = E_0 \cos\alpha(V)$ and $E_2 = E_0 \sin\alpha(V)$, where the rotation angle depends on V, the voltage applied to the EOM. This combination offers maximal modulation speed and has no chromatic angular dispersion. Implementing fast phase modulation, e.g., to realize the zero rotations depicted in Supplementary Fig. S2, Supplementary Fig. S5 and Supplementary Fig. S8, only requires an additional EOM with a 0° principal axis.

A double-pass configuration on a Spatial-Light Modulator (SLM) independently shapes the wavefront of each orthogonal linear polarization state (in yellow and blue), depicted in fig. 2b as a split diagram around a metallic mirror. The SLM first imprints a programmable retardation $\varphi_1(x,y)$ on E_1 (yellow beam), while the light in the orthogonal polarization state (blue beam) remains ideally unaffected. The following elements—QWP, convergent lens and metallic mirror—produce an inverted image of the SLM onto itself, as the system behaves as a $4f$ imaging system, and a 90° rotation of the polarization. This makes the second pass fall on a distinct region of the SLM (not shown in the simplified diagram of Fig. 2b), adding an arbitrary retardation $\varphi_2(x,y)$ to E_2 (yellow beam) and resulting in an output $E_2 e^{i\varphi_2(x,y)}\vec{e}_x + E_1 e^{i\varphi_1(x,y)}\vec{e}_y$.

Finally, both patterned fields E_1 and E_2 undergo a 45° polarization rotation by a half-wave plate and a Polarizing Beam Splitter (PBS) produces the final interference (Fig. 2c), outputting $\left(\frac{1}{2}E_1 e^{i\varphi_1(x,y)} + \frac{1}{2}E_2 e^{i\varphi_2(x,y)}\right)\vec{e}_x$. Both interfering beams share their optical path, meaning that this system has no need of active feedback loops or adjustments to maintain the relative phase stability.

It is common practice to use a blazed diffraction grating (e.g., horizontal) on SLM holograms to reject undesirable spurious phase structures imprinted on its zero-th order, i.e., the direct reflection[18]. A common spatial filter for the four paths (shown in Fig. 2d) rejects the zero-th order while the first diffraction order, which carries the patterned beams, passes through. As an added benefit, the use of the first diffraction order in the double-pass configuration filters out the crosstalk between polarization states due to, for example, the imperfect retardation of the QWP, see Supplementary Note 1. Additionally, we apply an orthogonal grating outside of the selected pupil region (Fig. 2e) for suppressing spurious light.

The modular geometry described above is replicated to produce four independent paths, each carrying an interferometric mixture of two shaped beams on a single SLM (Fig. 2d), with only one path active at any given moment. We tailored this system to operate with two paths in the green range (560 nm) and two in the red range (640 nm). After combining both laser sources with a dichroic mirror, an EOM-based path switching selects paths A/B or C/D for red/green. Each path contains its own EOM-based polarization rotator (as in Fig. 2a) followed by a spatial filter for cleaning up the mode. Paths A/B and C/D are split by dichroic mirrors and reach distinct regions of the SLM labeled as A1/B1/C1/D1 (Fig. 2e). The double-pass configuration changes their height and inverts the order of the regions on the second pass to D2/C2/B2/A2. Ultimately, the system can realize any of the beam manipulations previously mentioned in any of the four paths. After interference at the subsequent PBS, all paths are recombined into one and propagate into a MINFLUX confocal microscope, comprised of the commonly required blocks of scanning, detection, and stabilization (see Methods, MINFLUX Microscope).

In conclusion, for each excitation wavelength it is possible to select one of four phase masks e.g., φ_{A1}, φ_{C1}, φ_{A2}, φ_{C2} and, combine two pairs of them interferometrically e.g., $E_0\left[\chi_A e^{i\varphi_{A1}} + (1-\chi_A)e^{i\varphi_{A2}}\right]$ and $E_0[\chi_C e^{i\varphi_{C1}} + (1-\chi_C)e^{i\varphi_{C2}}]$, where the mixture coefficients χ_A and χ_C are dictated by the polarization rotation. We exploit this flexibility in the next section.

A fast axial scanner for efficient 3D MINFLUX

MINFLUX localization requires sequentially probing the emission of a fluorophore with tailored excitation beam shapes at distinct locations. These MINFLUX configurations usually enclose a circular or spherical region with a diameter L that scales the achievable localization precision and is shrunk sequentially in iterative MINFLUX[8]. Our system can produce a variety of such configurations, some of which are shown in Fig. 3a: all Gaussian or donut beams for 2D localization, all deformable bottle beams for 3D localization and mixtures of donut and bottle beams for improved photon efficiency, as well as interleaved wavelengths for simultaneous MINFLUX localization in distinct spectral bands (Fig. 3b). While the interferometric approach can produce lateral deflections suitable for MINFLUX (Figure 1a,g), we employed a pair of electro-optical deflectors that surpasses its range at a similar cost with a simpler implementation. To achieve axial deflection (Fig. 1d), however, this approach stands out for its accessibility and unrivaled time response.

Interferometric axial deflection of the *zero point* of a bottle beam overlapped with a Gaussian beam is shown via single-molecule fluorescence Point Spread Function (PSF) measurements (see Methods: PSF simulation and measurement) alongside simulations in Fig. 3c. This zero level can degrade due to a lack of coherence (see Supplementary Note 2) and misalignment between the interfering beams (Methods: Four channel polarization interferometer setup). Even under ideal conditions, a mismatch of the Gouy phase of both beams slightly degrades the deflected zero's quality as discussed in the previous section. Remarkably, the interferometer also works for pulsed excitation lasers as shown in Extended Fig. 1.

MINFLUX excitation schemes that displace beams with a zero of intensity harvest a gradient of *photon collection probability* that leads to a high localization precision[19]. This is hampered by zero degradation and is equivalent to a loss of signal-to-background ratio. Fig. 3d features a comparison of localization Cramér-Rao Bound (CRB) between defocused bottle beams with perfect zeros and interferometrically deformed bottle beams with zeros that degrade depending on their position. Despite the imperfect zeros there is no major deviation from the ideal localization precision.

Displaced bottle beams provide axial information, with poorer performance than donut beams in the lateral direction. This is because the emitted background *per emitted fluorescence photon* is higher for bottle beams than for donut beams, due to their weaker curvatures, larger size, and axial lobes. One could consider working in low background scenarios, but MINFLUX operates by purposely lowering the signal in exchange for high information content per photon by shrinking L. Thus, one should always strive to work in a regime in which background and/or zero quality are not negligible. We therefore implemented the capability of using a mixture of donut and bottle beams within one MINFLUX excitation scheme for lateral localization and axial localization, respectively. A CRB comparison of both scenarios (Fig. 3e) reveals a significant improvement for a molecule localized throughout the volume of the excitation pattern for an L of 50 nm.

The speed of the interferometric deflection dictates the wait time between the axial exposures of a MINFLUX excitation scheme (Fig. 3f) and it is limited by the bandwidth and electrical current of the amplifier driving the EOM of the polarization rotator (Fig 2a). We determined the rise time of the axial deflection by imaging the transient PSF at a time resolution of 200 ns (Fig. 3g, Methods: Bottle beam deflection speed Characterization). We measured a rise time (10%-90%) of <1.5 µs and a stabilization time (<1% of the asymptote) of <2.5 µs, with a system delay of 1.6 µs.

MINFLUX imaging and tracking

For proof-of-principle demonstrations of the system we used static and dynamic DNA origami structures as well as fixed cell samples. First, we designed and folded a DNA origami that arranges 12 Alexa Fluor 647 dye molecules in a three-by-four grid with 20 nm spacings for 3D STORM imaging (see Methods). The results are shown in Fig. 4a: all sites are clearly resolved with a Full Width at Half Maximum (FWHM) of the fitted Gaussian distribution of <3 nm in xy and <4.5 nm in z corresponding

to standard deviations for the localization precision of <1.3 nm and <1.9 nm, respectively. Averaging all emission events per site yields very high localization precisions as reported for DNA-PAINT[20]. On the STORM-MINFLUX data shown here, the FWHM of the average location ranges from 0.5nm to 1.0nm, corresponding to standard deviations between 0.2nm and 0.4nm in all dimensions. Furthermore, we acquired 3D images of the Nuclear Pore Complex (NPC) by labelling SNAP-tagged NUP96 with Alexa Fluor 647 in fixed U-2 OS cells, see Fig. 4b.

To showcase the 3D tracking capability and temporal resolution of the system, we designed a DNA origami with a fluorescently labelled DNA strand oscillating axially between two catching sites 14 nm apart. The DNA origami itself is rod-like, approximately 50 nm-tall, and features 16 biotin-modified DNA staple strands for it to stand vertically on streptavidin-functionalized surfaces (Fig. 4c). Localization traces shown in Fig. 4c are at 1 ms and 10 ms temporal binning, which correspond to 150 and 1500 average photon counts per localization, respectively. At 1 ms temporal resolution, the standard deviations for the localization precisions are 4.9, 4.7 and 4.1 nm in x, y and z. After further binning, the measured distance between catching sites is 14.9 ± 1.7 nm, see Methods: Data analysis.

The measurement scheme for tracking consisted of a first step where the excitation pattern is actively centered onto the fluorophore via a proportional-integral closed-loop control system that uses the live estimated MINFLUX localization. This feedback loop can flexibly act on the tip-tilt mirror, the EODs, and the interferometric axial scanner simultaneously. We chose the former because it is de-scanned and hence the collection efficiency is optimal after centering. Once centered, the excitation pattern is static over time and probes the molecule until photobleaching. The effectiveness of the centering step is evident in the localization traces in Fig. 4c, where MINFLUX tracking is initiated within a 10 nm range from the molecule's actual location.

Finally, we utilized the two-color excitation of the presented MINFLUX implementation to simultaneously track two spectrally distinct emitters (ATTO 647N and Janelia Fluor 549 dyes), each transiently binding to two distinct sites on a 2D DNA origami structure of programmable dynamics (Fig. 4d). The average photon count per localization in the displayed localization traces is 1200 for both emitters, resulting in 20 ms temporal resolution for ATTO 647N and 25 ms for Janelia Fluor 549. The corresponding standard deviations for the xyz-localization precisions are 2.2, 2.3, 1.8 nm for ATTO 647N and 1.8, 1.7, 1.6 nm for Janelia Fluor 549.

In this case, the measurement scheme involved a centering step at 640 nm excitation wavelength, converging onto the far-red dye, and defining a volume that encompasses both emitters. Following centering, the two excitation lasers were interleaved in time to probe the emitters with static excitation patterns, each one lasting approximately 250 µs. Notably, the sequence length is not limited by the deflection speed of either the EODs or the axial scanner presented here, but rather by the fluorophore's emission rate and the need to bin sufficient photon counts to achieve single-digit localization precision.

Discussion

We presented an interferometric strategy to manipulate a variety of focused beams, including some that are newly described. Our efforts centered on beams with intensity zeros and the manipulation of these regions through displacements and tilts. We proposed the use of three general optical blocks to realize this strategy: a polarization rotator, beam shaper and interferometer. An implementation of these blocks in a four-channel two-color configuration was introduced and employed as the excitation module of a custom MINFLUX microscope. We utilized this microscope for super-resolution imaging as well as single- and multi-molecule tracking with novel MINFLUX excitation schemes and dual-color operation, reaching state-of-the-art localization precision and time resolution.

The proposed common-path polarization interferometer is notable for its phase stability without active feedback, its versatility and extendibility. Its implementation is devoid of mechanical parts and manipulates beams at the microsecond time scale even for pulsed lasers. Nevertheless, slower and

more economic polarization rotation technologies are also compatible, such as mechanical- or liquid-crystal-based methods. Simplified implementations could achieve similar interferometric effects. For example, a (commercially available) birefringent phase mask could replace the SLM. However, it is limited to a fixed wavelength and lacks the ability to correct aberrations or adjust phases. A single-pass SLM configuration could realize all interferometric combinations involving a Gaussian beam originating from the direct reflection of the modulator's unaffected polarization. Nevertheless, this approach excludes blazed gratings, which would eliminate zero-order effects arising from the SLM pixelation[18]. Additionally, the lack of fine alignment and aberration correction on the directly reflected Gaussian beam leads to zero degradation, non-linear axial calibration and unintended tilts.

A wide range of methods might benefit from the presented approach. For instance, the volumetric neuronal imaging technique presented in[21]: instead of alternating two axial positions of the employed Bessel-droplet excitation foci via an SLM update, the interferometer could scan them continuously on a much faster time scale—potentially reaching the nanosecond regime when using a resonant EOM—to yield a more homogeneous distribution (see Supplementary Fig. S12). The same concept applies to optical trapping techniques that confine multiple particles axially[22], and the axial deformation of the bottle beam might be used as a photophoretic trap capable of loading and unloading a particle similar to[23]. Furthermore, applying our axial displacement strategy to a STED beam is optimally suited for extending conventional fast STED imaging[24] (especially for small volumes) and MINSTED[5] into the third dimension.

We believe that this work will prove especially valuable for future MINFLUX systems: among MINFLUX' major strengths is its isotropic localization precision in all three spatial dimensions. Yet, custom systems refrained from 3D implementations, presumably due to their complexity. Our method is not only a convenient alternative to current technologies for axial scanning but also unrivaled in its deflection speed. It integrates and scales well with other modalities, allowing the use of multiple beam shapes, several wavelengths and pulsed operation compatible with pulsed interleaved MINFLUX[25]. As such, we project that it will facilitate broader adoption of 3D MINFLUX and help to extend its current capabilities even further, unlocking new possibilities for investigating complex dynamic processes and structural studies on the molecular level involving single or multiple emitters.

Acknowledgements

We thank Karina Arellano Ayala for assistance with sample preparation. We thank Anna Deputatova for assistance with designing and folding the 32HB origami. F.B. was supported by Boehringer Ingelheim. This project has received funding from the European Research Council (ERC) under the European Union's Horizon 2020 research and innovation program (Grant agreement No. 853348). For the purpose of Open Access, the authors have applied a CC BY public copyright license to any Author Accepted Manuscript (AAM) version arising from this submission.

Author Contributions

M.K.G., A.G. and F.B. designed and built the optical system, and programmed the hardware control. M.K.G., A.G., A.P., M.S. and F.B. programmed the processing and visualization software. M.K.G. and A.G. performed experiments and data analysis. A.P. designed and folded DNA origami and optimized used protocols. A.P. prepared and optimized cell samples. M.S. performed simulations and optimizations. M.K.G., A.G., A.P. and F.B. wrote the manuscript. F.B. supervised the project.

Competing Interests

F.B. holds patents on principles, embodiments and procedures of MINFLUX.

Figures

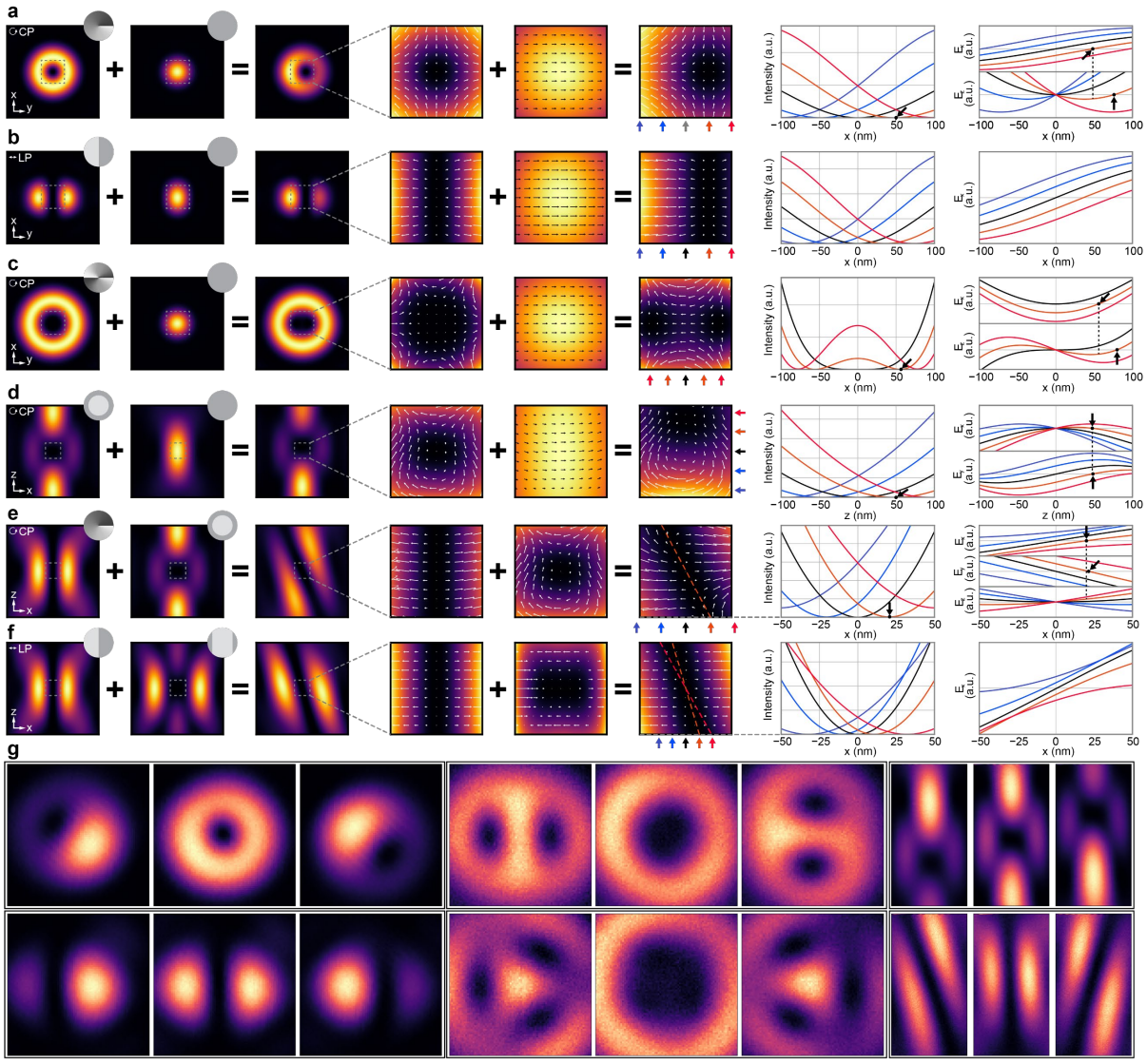

Fig. 1: Interference of canonical beams. a, Combination of charge-1 donut with Gaussian beams. **b**, Combination of bi-lobed and Gaussian beams. **c**, Combination of charge-2 donut and Gaussian beams. **d**, Combination of bottle and Gaussian beams. **e**, Combination of charge-1 donut and bottle beams. **f**, Combination of bi-lobed and bottle-slice beams. (Left column) Intensities of combined beams at the xy (a-c, 800x800nm) and xz (d-f, 1200x1200nm) plane. CP: circularly polarized. LP: linearly polarized. Dashed squares: 200x200nm. The corresponding phase masks for each canonical beam shape are indicated in grey at the top right corner. (Middle column) Zoomed intensities in the dashed squares with a vector plot of the xy (a-c) or xz (d-f) components of the electric field. The resulting displaced zero coordinate is marked by an arrow. (Right column) Intensity and electric field profiles for each x, y and/or z component along the x axis (a-c), z axis (d) or x axes offset in z (e,f), chosen to highlight the interplay between electric field components. Mismatches between zeros of different components are marked with arrows. **g,** Interferometrically shaped PSFs measured on 40 nm gold particles via scattering for three different mixture amplitudes. Top left: donut plus Gaussian, xy; Top middle: charge-2 donut plus Gaussian, xy; Top right: Bottle beam plus Gaussian, xz; Bottom left: bi-lobed plus Gaussian, xy; Bottom middle: charge-3 donut plus Gaussian, xy; Bottom right: donut plus bottle beam, xz.

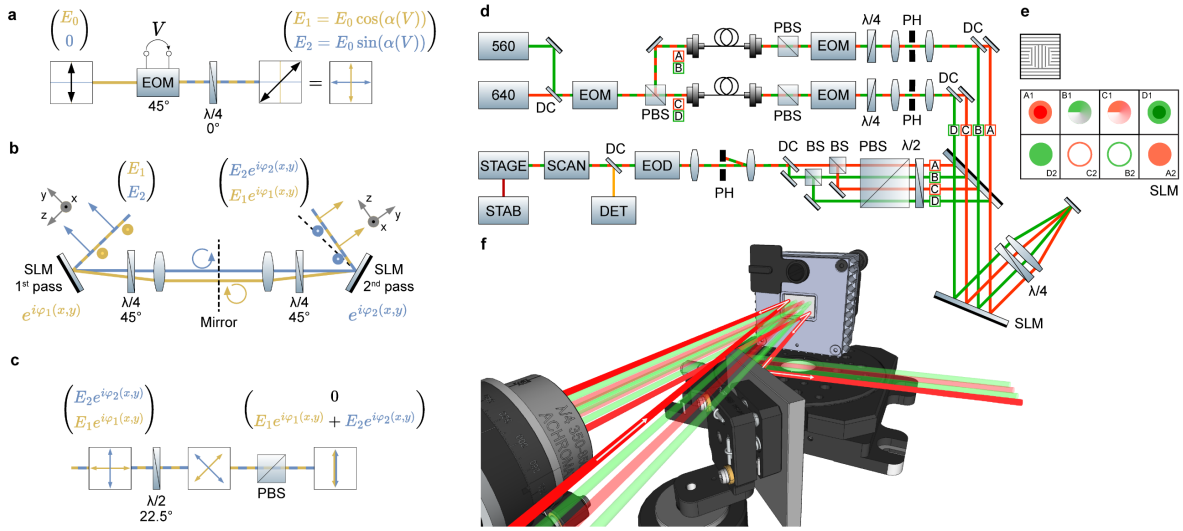

Fig. 2: Implementation of a multi-channel polarization interferometer. **a**, Polarization rotation module. The square with arrows represents the polarization state. **b**, Simplified diagram of the beam shaping module. A double-pass configuration on an SLM is shown unfolded with respect to its mirror. **c**, Beam combination/interference module. **d**, Complete system. **e**, Detailed grating structure used in all SLM regions (above), example phase masks (below) for interferometric bottle beam deflection in A1+A2 (and D1+D2) and donut beam generation on B1 (and C1) for red (and green) wavelengths; B2 and C2 are unused. **f**, 3D render of the SLM with all beam paths. The arrows indicate the propagation direction for one of the red paths (path A): it passes above a two-inch square mirror glued on a half-inch kinematic mount, reflects off the SLM, propagates through the imaging system and the QWP (not shown), reflects off the SLM again at a different height and is eventually picked up by the square mirror.

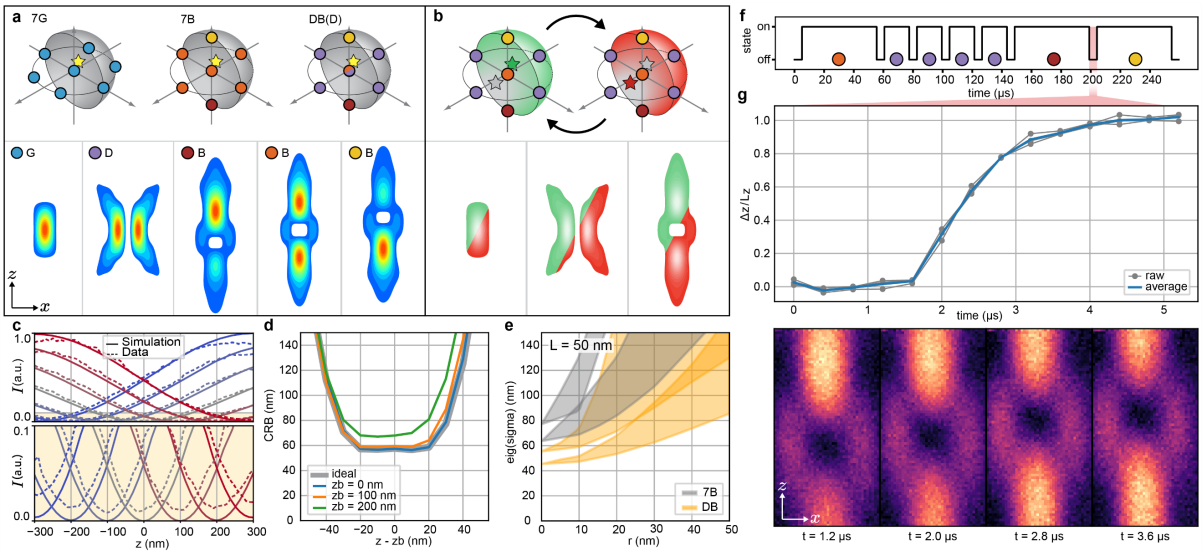

Fig. 3: MINFLUX excitation schemes with interferometrically deformed beams and mixed shapes. **a**, Depiction of the 2D and 3D MINFLUX excitation schemes realized with our system (top) and their corresponding beam shapes (bottom): Gaussian beam (G; blue), donut beam (D; purple) and bottle beam (B; red, orange, yellow) at different interferometric deflection states. **b**, Strategy for tracking two emitters simultaneously by rapidly switching between schemes for red and green excitation wavelengths, with seven exposures each. **c**, Juxtaposition of simulated and measured intensity profiles of the deflected bottle beam zero. Bottom: zoom-in of the yellow area. Despite the deformation, the profiles stay parabolic over a large range. The zero degradation of the simulated profiles is visible towards the edges. The measured profiles never reach a true zero due to background and aberrations. **d**, Comparison of the CRB for a single photon at a signal-to-background ratio of five along the optical axis z for ideally deflected bottle beams (without deformation, gray) and for our interferometric approach. Only when localizing emitters far off focus, given by the axial distance zb, the performance degrades slightly. **e**, Eigenvalue ranges of the 3x3 CRB covariance matrix for one collected photon with the *mixed beam* scheme comprised of donut and bottle beams (DB) versus the conventional 3D MINFLUX excitation scheme consisting of bottle beams only (7B). Each condition displays two shaded areas representing the range of the minimum (lower) and the maximum (upper) CRB eigenvalue for emitter positions on a sphere with radius r centered on the excitation pattern, indicating anisotropy; the width of each area accounts for spatial inhomogeneity. **f**, Timing diagram for the mixed beam scheme, with larger weights for the bottle beam exposures. **g**, Measurement of the interferometric deflection transient for a distance of 271 nm (top). Each point corresponds to the location of the zero of intensity obtained from a complete PSF measurement (bottom, selected time points).

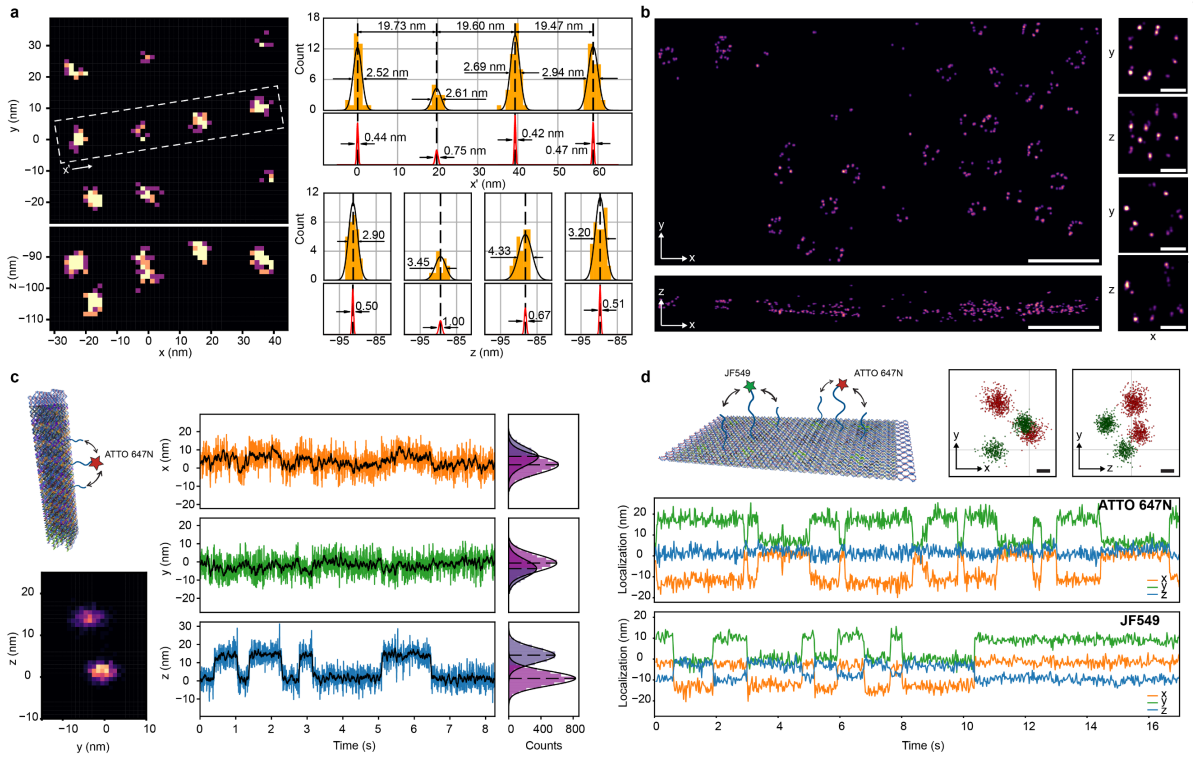

Fig. 4: MINFLUX imaging and tracking. **a**, 3D Imaging of Alexa Fluor 647 fluorophores arranged in a 3x4 grid with 20 nm spacing on a DNA origami (left). Localization histogram along the marked region with indications for distances and FWHM (top right) and corresponding histograms along z for each site (bottom right); for each site, the FWHM of the mean of all ocurrences is marked in red. **b,** 3D imaging of NUP96-SNAP labelled with BG-Alexa Fluor 647 in fixed U-2 OS cells. **c**, 3D tracking of ATTO647N conjugated to a DNA strand that oscillates axially between two binding sites on a DNA origami (top left). Histogram of localizations at 10 ms temporal resolution (bottom left). Localization traces for each coordinate (middle) at 1 ms temporal resolution (x: orange, y: green, z: blue) and with 10-fold temporal binning (black). The origin of the axes is set by the excitation pattern center after the initial centering step. Histograms for the two distinct positions of the molecule (right). **d**, Schematic of a 2D origami (upper left) with ATTO647N and Janelia Fluor 549 dyes, each transiently binding to two distinct sites. XY and YZ projections (upper right) of all localizations in the traces displayed below. Localization traces for ATTO647N and Janelia Fluor 549 (bottom), at 20 ms and 25 ms temporal resolution, respectively. DNA origami renders were generated with oxView. Scale bars: (**b**) 500 nm for large field of view, 50 nm for single pores, (**d**) 5 nm.

Tables

Beam	Polarization	Phase mask	Zero type	$\boldsymbol{E_x(\vec{r})}$	$\boldsymbol{E_y(\vec{r})}$	$\boldsymbol{E_z(\vec{r})}$
Gaussian	Circular	Flat	None	1	i	$x - iy$
Gaussian	Linear x	Flat	None	1	0	x
Bi-lobed	Linear x	Half-moon	Transverse plane	x	0	$-ixy$
Donut charge 1	Circular	Vortex 2π	Axial line	$x + iy$	$ix - y$	$-x^2 + y^2 + 2ixy$
Donut charge 1	Circular	Vortex -2π	None	$x - iy$	$ix + y$	1
Donut charge 2	Circular	Vortex 4π	Axial line	$-x^2 + y^2 + 2ixy$	$i(-x^2 + y^2) - 2xy$	0
Bottle	Circular	Top-hat	Point	$x^2 + y^2 + cz$	$i[x^2 + y^2 + cz]$	$ix - y$
Bottle-slice	Linear x	Top-hat slice	Lateral line	$x^2 + cz$	0	0

Table 1. Canonical beam shapes with their polarization state, corresponding back-focal plane phase mask and zero type. Second order approximations of the focused electric field at the origin are shown for each component of the electric field in the last three columns, excluding proportional constants. The constant c absorbs differences between lateral and axial prefactors.

Beam 1	Beam 2	Polarization state	Zero type	Interference Result
Donut charge 1	Gaussian	Circular	Axial line	Lateral displacement
Bi-lobed	Gaussian	Linear	Axial plane	Lateral displacement
Donut charge 2	Gaussian	Circular	Axial line	Lateral displacement Double lines
Bottle	Gaussian	Circular	Point	Axial displacement
Donut charge 1	Bottle	Circular	Axial line	Line tilt
Bi-lobed	Bottle-slice	Linear	Axial plane	Plane tilt

Table 2. Examples of some beam combinations and the resulting effects on the featured zero.

Methods

PSF simulation and measurement

Electric field calculations near the focus of an objective with high numerical aperture as shown in Fig. 1**a**-**f** and Fig. 3**a**-**c** were performed via a custom python implementation of [26].

The PSFs of the excitation beams were measured via a "bead stack" by moving the beam in xy via either the EODs or the tip/tilt mirror and in z by moving the fine stage (see Supplementary). The "bead" took the form of (i) fluorescent beads (see Fluorescent microspheres samples), (ii) single dye molecules attached to a DNA origami (see Origami sample preparation) or (iii) gold particles where the signal was the scattered excitation light (see Gold nanoparticles samples) detected on the avalanche photo diodes after removing the notch filter blocking the excitations wavelengths in the detection module.

The measured PSF gallery shown in Fig. 1**g** was acquired via scattering on gold particles. For the bi-lobed PSF the last QWP was removed to obtain linear polarization.

The measured intensity profiles shown in Fig. 3**c** were acquired on single molecule by scanning the voltage of the polarization rotator as well as moving the fine z-stage. One raw measurement contained 15 (not all are shown) profiles of different axial deflection offsets. Three such measurements were averaged and normalized to the maximum across all averaged profiles to produce the curves shown.

For the PSF measurements shown in Fig. 3**g** see Bottle beam deflection speed Characterization.

MINFLUX Microscope

We use an EOM and a PBS to switch the main excitation beam carrying light of either 560 nm or 640 nm between two paths, each coupled into a fiber. The fiber outputs then go through a PBS for polarization cleanup and an EOM plus waveplates for polarization rotation. A three-lens (zoom) telescope with a spatial filter cleans the mode and allows for adjustable magnification. The two paths are then split by a dichroic mirror (DC) into four; two for 640 nm and two for 560 nm. All paths are aligned to be parallel and then go through the SLM double-pass configuration as described in the main text. All four paths are combined into one via regular beamsplitters and another DC. A telescope with an adjustable iris at its focal plane blocks the zero-th diffraction order and relays the image of the SLM. The remainder of the system adheres to the configuration presented in [8]. For a detailed schematic see Supplementary Note .

The microscope control system comprises an FPGA board (NI USB-7856R), two data acquisition boards (NI PCIe-6363 and MCC USB-3114), and two Windows 10 PCs (one solely dedicated to the active stabilization). These hardware components are integrated through custom LabVIEW software, following the structure outlined in [8]. However, we updated the software to specifically control the developed polarization interferometer and enable convergence onto molecules through the implementation of a proportional-integral controller in MINFLUX tracking experiments.

Furthermore, a Raspberry Pi (RPI 4B 8GB) running Raspbian is used to display phase masks on the SLM via HDMI. It runs a simple web server (written in Go) that receives the desired phase mask as a png file through a POST request which it then displays via a lightweight image viewer called "feh".

SLM setup

We used the phase linearization provided by the vendor but adjusted the scale for the wavelengths we employed: We calibrated the phase value that corresponds to a retardation of 2π (one full wavelength) by maximizing the power in the first diffraction order when scanning the amplitude of the blazed grating, i.e., the maximum phase of its periodic ramp.

To correct for excitation beam aberrations we employed a pupil-segmentation approach[27] to measure the aberrated wavefront and apply resulting correction as an additive phase mask on the SLM. These corrections are crucial for achieving acceptable beam shapes, especially for the bottle beam.

The SLM was divided into 8 independent regions, each with its own calibration and correction.

Four channel polarization interferometer setup

Polarization rotator

The output of all EOMs and their QWPs were monitored via a polarimeter (PAX1000VIS/M, Thorlabs) while continuously modulating at low frequency with a range larger than the lambda-half voltage. The rotation of the EOM was adjusted until the two linear polarization states occurring during the modulation were 90 degrees apart (180 degrees on the Poincaré Sphere) while the rotation of the QWP was adjusted to yield close to purely linear polarization states throughout the modulation.

SLM double pass

The SLM double pass was aligned such that the images of the first and the second pass coincide by applying the right pixel offsets to the SLM regions (according to the geometry) and adjusting the mirror (DP.MM). The rotation of the quarter-wave plate (DP.QWP) was adjusted to minimize crosstalk from one pass to the other. The rotation of the half-wave plate (DP.HWP) was set to 22.5° to have equal amplitudes in the mixture of polarization states leading to a linear deflection calibration, see Supplementary Fig. S14.

The voltage offsets on the path switch EOM (E.EOM) were adjusted to minimize crosstalk between paths of the same wavelength. The voltage values that select only the first or second pass were adjusted to minimize the crosstalk between the first and the second pass.

To tune the polarization interferometer of a path, we adjusted the relative (flat) phase between the first and the second pass, and the tip, tilt and defocus Zernike terms of the first pass on the SLM. For that, we set the voltage of the polarization rotating EOM to a value where both polarization components carry equal power measured on a power meter close to the objective. Then, plain gratings (aberration corrected) were displayed on the SLM, and the power was minimized (destructive interference) by adjusting the above terms. This procedure was automated.

For axial deflection of a bottle beam, a flat phase of $\pi/2$ was applied to the second pass as is necessary for the right phase relations between the top-hat phase mask and the Gaussian's phase mask (plain grating). Finally, the quality of the deflection was tested by measuring intensity profiles along z on 100 nm fluorescent beads (FluoSpheres, 0.1 µm, Tetraspeck; Thermo Fisher Scientific) or single molecules on DNA origami (ATTO647N, Cy3B) and checking that the intensity minimum, the zero, was at an approximately constant level over a range of 600 nm for several deflection offsets. If not, small adjustments to the diameter of the π-phase step of the top-hat phase mask were made. Finally, the z-profiles were used to calibrate the polarization rotator's EOM input voltage, such that, for a given target, the deflected distance matched the movement in z of the fine stage.

Beam combination alignment

All four paths were manually aligned by overlapping cross patterns generated on the SLM by simultaneously looking at an image- and a conjugate plane of the SLM. Fine corrections were made by adjusting the tip and tilt Zernike terms of the respective paths on the SLM while measuring intensity profiles along x, y and z directions on 40 nm fluorescent beads (FluoSpheres, 0.04 µm, dark-red fluorescence; Thermo Fisher Scientific) such that the intensity minima coincided.

Bottle beam deflection speed Characterization

The xz-PSF measurement of the deflected bottle beam for several time points was achieved by collecting excitation beam photons scattered off 40 nm gold particles (see Gold nanoparticles samples) in a refractive index matched medium to avoid PSF artefacts caused by the reflection on the coverslip

interface. An excitation scheme with two deflected bottle beams some axial distance apart (for Fig. 3: 271 nm) was used. We used the 3 µm diameter confocal detector path and set the excitation power to yield a count rate of roughly 8 MHz. The counts for each of the two excitations were collected in two separate channels. Then, for the second exposure the counts were gated with a 200 ns window that was shifted in time in steps of 400 ns to probe the transition from the axial position of exposure one to the axial position of exposure two. The z-trajectory of the gated channel was calculated by fitting the intensity minimum. Furthermore, it was drift corrected by fitting the intensity minimum of the ungated channel (static bottle beam).

Sample preparation

Reagents

M13mp18-derived p7249 scaffold was obtained from NEB (catalog no. N4040S). Unmodified and biotinylated oligonucleotides for the rectangle origamis were obtained from MWG Eurofins, while unmodified and biotinylated oligonucleotides for the 3D origami and modified oligonucleotide for conjugation were obtained from Sigma-Aldrich. Freeze 'N Squeeze columns (catalog no. 732-6165) were obtained from Bio-Rad. Cy3b-maleimide (catalog no. 11525834) was obtained from Cytiva. Alexa Flour 647-NHS ester (catalog no. 16820) was obtained from Lumiprobe. ATTO647N-maleimide (catalog no. AD647N-41) was obtained from ATTO-TEC. Janelia Fluor 549-NHS ester (catalog no. 6147) was obtained from Tocris. TCEP hydrochloride (catalog no. C4706-2G), dimethylformamide (DMF) (catalog no. 227056-100ML), and dithiothreitol (DTT) (catalog no. D0632-5G) were obtained from Sigma-Aldrich. Absolute ethanol (catalog no. 1009831000) was obtained from Merck. Sodium bicarbonate (catalog no. 27778293) was obtained from VWR. Tris-HCl 1 M pH 8 and 7.5, 10x and 1X PBS pH 7.3, 1X TAE pH 8, 1 M HEPES pH 7.3, EDTA 0.5 M pH 8, 1 M magnesium chloride, 1 M potassium chloride and 5 M sodium chloride were obtained from our in-house media kitchen. Pure water was obtained from a MilliQ water filtration system. SYBR Safe (catalog no. S33102) was obtained from Invitrogen. Neutravidin protein (catalog no. 31000) was obtained from Thermo Scientific. Polyethylene glycol (PEG)-8000 (catalog no. P2139-500G) and Bovine Serum Albumin-biotin (BSA-biotin) (catalog no. A8549-10MG) were obtained from Sigma-Aldrich. Round and square # 1.5 coverslips (catalog no. 6311344 and MENZBB024024AC23 respectively) were obtained from Menzel Gläser. Flat microscope slides (catalog no. 09-3000) were obtained from Bio-Optica and Sail brand single concave glass slides (catalog no. 7103) were obtained from SmartLabs. Hellmanex III (catalog no. Z805939-1EA) was obtained from Sigma-Aldrich. Double sided tape (catalog no. 665D) was obtained from Scotch. Twinsil speed 22 (catalog no. 1300-1002) was obtained from Picodent. Epoxy glue (catalog no. G14250) was obtained from Thorlabs. Tween 20 (catalog no. P9416-50ML), protocatechuate 3,4-dioxygenase from Pseudomonas sp. (PCD) (catalog no. P8279-25UN), 3,4-dihydroxybenzoic acid (PCA) (catalog no. 37580-25G-F), (+−)-6-hydroxy-2,5,7,8-tetramethylchromane-2-carboxylic acid (Trolox) (catalog no. 238813-1G), methyl viologen (MV) (catalog no. 856177-1G) and sodium hydroxide (catalog no. 30620-1KG-M) were obtained from Sigma-Aldrich. Methanol (catalog no. 20846.326) and anhydrous D-glucose (catalog no. 0188-1KG) were obtained from VWR. Glycerol (catalog no. A0970-1000) was obtained from BioChemica. Glucose oxidase (catalog no. G2133-10KU), catalase (catalog no. C100-50MG) and cysteamine hydrochloride (MEA) (catalog no. M6500-25G) were obtained from Sigma-Aldrich. 1X Dulbecco's modified Eagle medium (DMEM) (catalog no. 11880028), 100X MEM non-essential amino acids solution (NEAA) (catalog no. 11140035), Fetal Bovine Serum (FBS) (catalog no. 10500064) and trypsin-EDTA 0.5% (catalog no. 15400054) were obtained from Gibco. L-glutamine (catalog no. 25030024) was obtained from Thermo Scientific. Penicillin-streptomycin (catalog no. P0781) was obtained from Sigma-Aldrich. The cell line is available via Cell Line Services (Nup96–SNAP, 300444). Paraformaldehyde (PFA) (catalog no. 15714) was obtained from Electron Microscopy Sciences. Triton X-100 (catalog no. T8787-100ML) was obtained from Sigma-Aldrich. Ammonium chloride (catalog no. 1011451000) was obtained from Merck. BSA (catalog no. 422351S) was obtained from VWR. Image-iT FX Signal Enhancer (catalog no. I36933) was obtained from Invitrogen. SNAP-Surface Alexa Fluor 647 (catalog no. S9136S) was obtained from NEB. 40 nm and 90 nm diameter gold

nanoparticles (catalog no. G-40-100 and G-90-100) were obtained from cytodiagnostics. 100 nm Tetraspeck beads (catalog no. T7279), 40 nm dark-red beads (catalog no. F8789) and 40 nm red-orange beads (catalog no. F8794) were obtained from Invitrogen. Norland Optical Adhesive 74 (catalog no. 7404001) was obtained from APM Technica.

Fluorescent microspheres samples

Different fluorescent microspheres ("beads") samples were used for calibrations, aberration correction, and testing the system. Glass coverslips were first cleaned via three rounds of water-bath sonication for 10 min in a 2% solution of Hellmanex III. Between each round and at the end, the slides were copiously rinsed with MilliQ water, and finally dried with compressed nitrogen before storage. A flow chamber was formed by placing two double-sided Scotch strips parallel to each other on the microscope slide, and then sandwiching them between the slide and the coverslip. First, 20 µl of a 1:5 dilution of 90 nm gold nanoparticles in 1X PBS was incubated for 5 min in the flow chamber. After a 20 µl wash with 1X PBS, the bead solution was incubated for 10 min. For Tetraspeck beads, this consisted of a 1:250 dilution of beads in 1X PBS, sonicated for 10 min. For the dark-red and red-orange 40 nm beads, this consisted of a 1:1000 dilution in 1X PBS, sonicated for 10 min, and then further diluted 1:1000 in 1X PBS before incubation. After a 20 µl wash with 1X PBS, the chamber was filled with more 1X PBS, and then sealed with epoxy glue.

Stock solutions

100X MEA: 568 mg of cysteamine hydrochloride in 5 ml of water, pH adjusted to 8 with NaOH and stored at -20°C.

100X GLOX: 2 mg of glucose oxidase in 1xPBS + a variable volume of catalase (dependent on the product batch) for a final concentration of 40 mg/ml glucose oxidase and 6.4 mg/ml catalase, stored at 4°C for a maximum of two weeks.

100X MV: 156 mg of MV in 5 mM of 50 mM Tris-HCl pH 8, stored at -20°C.

100X Trolox: 100 mg of Trolox dissolved in 430 µl of methanol, then added to 345 µl of 1 M NaOH in 3.2 ml of water, stored at -20°C.

40X PCA: 154 mg of PCA in 10 ml of water, pH adjusted to 9 with NaOH and stored at -20°C.

500X PCD: 9.3 mg of PCD in 2.66 ml of 100 mM Tris-HCl pH 8, 50 mM KCl, 1 mM EDTA, 50% glycerol, stored at -20°C.

2X TCEP: 11.5 mg of TCEP hydrochloride in 20 ml of 20 mM HEPES pH 7.3 + 100 mM NaCl, pH adjusted to 7.3 with NaOH and stored at -20°C.

Gold nanoparticles samples

Gold nanoparticle samples were used for PSF measurements and for the speed characterization of the axial scanner via backscattering. A flow chamber was made, and 40 nm gold nanoparticles were incubated as described above. Afterwards, the NOA 74 optical adhesive, matching the refractive index of the immersion oil, was flowed in the chamber, replacing the aqueous buffer, and cured by exposing to UV light for 15-20 minutes with a handheld UV lamp.

Design, folding and purification of DNA origami nanostructures

All DNA origamis are based on the p7249 scaffold derived from the M13mp18 bacteriophage. The two-dimensional rectangle origami is based on the design in[28], while the three-dimensional 32-helix bundle (32HB) origami was designed using Cadnano2 (see Supplementary Fig.) and tested in CanDo[30]. Folding of the DNA origamis was accomplished in a 50 µl one-pot reaction consisting of 10 nM scaffold strand (20 nM for the 32HB), 100 nM unmodified staple strands, excluding the ones substituted by a modified staple strand (200 nM for the 32HB), 500 nM biotynilated staples (1 µM for the 32 HB origami) (for a list of the unmodified and biotynilated staple strands, see Supplementary Table S1 and Supplementary

Table S2) and 500 nM modified staple strands (1 µM for the 32HB) (for a list of the modified staples strands, see Supplementary Table S3) in 1X folding buffer (5 mM Tris-HCl pH 8, 1 mM EDTA, 12.5 mM $MgCl_2$ or 20 mM $MgCl_2$ for the 32HB). The reaction mix was then subjected to a thermal annealing ramp in a thermocycler. For the rectangle origami, this consisted in 5 min at 80°C, then cooling immediately to 60°C followed by cooling from 60°C to 4°C in steps of 1°C every 3 min 21 s. The sample was then held at 4°C until purification. For the 32HB, the ramp consisted in 15' at 65°C, then cooling immediately to 60°C followed by cooling from 60°C to 44°C in steps of 1°C every 60 min, followed by cooling from 44°C to 25°C in steps of 1°C every 10 min. The sample was then cooled immediately to 4°C and held at that temperature until purification.

In order to remove most of the excess staple strands, the rectangle origami was initially purified via one round of PEG precipitation by adding the same volume of PEG buffer (1X TAE pH 8.0 + 15% PEG-8000, 500 mM NaCl, 12.5 mM $MgCl_2$ or 20 mM $MgCl_2$ for the 32HB), centrifuging at 14,000 *g* at 4 °C for 30 min, removing the supernatant and resuspending in folding buffer. In the case of the 32HB, in order to select properly-folded origami, this purification was instead carried out via agarose gel electrophoresis (1.5% agarose, 0.5× TAE, 20 mM $MgCl_2$, 1× SYBR Safe, run in 0.5× TAE, 20 mM $MgCl_2$ as running buffer) at 3 V cm^{-1} for 3 h at 4°C. The fastest running band, corresponding to properly-folded origami, was excised on a UV transilluminator, crushed, filled into a Freeze 'N Squeeze column, incubated for 5 min at -20°C and centrifuged for 3 min at 13000 *g* at room temperature.

After this initial purification, the origami solution was incubated with 1 µM of the appropriate fluorescent oligos (for a list of the fluorescent oligos, see Supplementary Table S4) for 2 h at room temperature, in order for it to bind to its target extended staple on the origami.

Finally, both rectangle and 32HB origamis were subjected to 3 rounds of PEG precipitation as described above to fully remove excess folding staples and fluorescent strands, and stored in low-binding Eppendorf tubes at -20°C.

Fluorescent labelling of oligonucleotides and purification

Oligonucleotides for external labelling of DNA origami were labelled in-house using either the maleimide + thiol or the NHS ester + amine chemistry. For the maleimide + thiol chemistry, 10 nmol of thiol-modified oligonucleotide in 50 µl of 20 mM HEPES pH 7.3 + 100 mM NaCl were added to 50 µl of 2x TCEP and incubated for 1 h at room temperature in the dark to reduce the disulfide bonds of the oligonucleotides. Then, 10 µl of 10 mM dye-maleimide in DMF were added to the reaction, the volume was brought to 200 µl with 20 mM HEPES pH 7.3 + 100 mM NaCl, and the reaction incubated for 2 h at room temperature in the dark. The reaction was then quenched by adding DTT to a final concentration of 50 mM. For the NHS ester + amine chemistry, 10 nmol of amine-modified oligos were subjected to one round of ethanol precipitation to remove any residual amine from the synthesis process by adding 0.1 volumes of 3 M NaCl and 2.5 volumes of cold absolute ethanol, incubating at -20°C for 30 min, centrifuging at 21000 *g* at 4°C for 30 min, and resuspending the pellet in 190 µl of 100 mM sodium bicarbonate pH 8.3. Then, 10 µl of 10 mM dye-NHS ester in DMF were added to the reaction, and the reaction was incubated for 2 h at room temperature in the dark. The reaction was quenched by adding Tris-HCl pH 8 to a final concentration of 50 mM. For both chemistries, the reaction pot after quenching was subjected to one preparative round of ethanol precipitation as just described before purifying via reverse-phase high-performance liquid chromatography on an UltiMate 3000 HPLC system equipped with a Phenomenex Clarity 5 µm oligo-RP column. The purified oligos were resuspended to 50 µM in 20 mM HEPES pH 7.3 + 100 mM NaCl and stored in low-binding Eppendorf tubes at -20°C.

Origami sample preparation

Origami samples were prepared as previously described[19]. In short, a flow chamber was made as described above, and similarly incubated with 90 nm gold nanoparticles. The chamber was then flushed with 20 µl of 1X PBS, then with 20 µl of buffer A (10 mM Tris-HCl pH 7.5, 100 mM NaCl and

0.05% Tween 20), and then incubated with 20 µl of 1 mg ml-1 BSA-biotin in buffer A for 5 min. The chamber was then flushed with 20 µl of buffer A, and then incubated with 0.5 mg ml-1 of neutravidin in buffer A for 5 min. The chamber was then flushed with 20 µl of buffer A, then with 20 µl of buffer B (5 mM Tris-HCl pH 8, 1 mM EDTA, 12.5 mM MgCl2 and 0.05% Tween), and then incubated with 20 µl of 30 pM DNA origami in buffer B for 8 min. The chamber was then flushed with 20 µl of buffer B, and finally filled with 20 µl of the appropriate imaging buffer. For tracking experiments, this consisted of a ROXS buffer containing 1X PCA (1 mM), 1X PCD (10 nM), 1X MV (1 mM), and 1X Trolox (1 mM) in buffer B. For STORM experiments, this consisted of a blinking buffer containing 1X GLOX (0.4 mg ml-1 glucose oxidase, 64 µg ml-1 catalase), and 1-10 mM MEA in buffer B + 10% w/v glucose. The sample was then immediately sealed with Twinsil. The buffer was replaced approximately every 2 h in the case of the blinking buffer to avoid unwanted blinking behavior due to pH drift caused by the oxygen scavenging system.

U2OS NUP96-SNAP cell sample preparation

Labelling of the U2OS NUP96-SNAP cell samples was performed similarly to previously described[8]. Cells were cultured in DMEM without phenol red supplemented with 1X MEM NEAA, 10% v/v FBS, 2 mM L-glutamine and 1:100 penicillin-streptomycin at 37°C, 5% CO_2 and 100% humidity and passaged every other day. The day before imaging, cells were seeded on round coverslips, cleaned as described above, so as to reach around 70% confluency the next day. The next day, cells were prefixed with 2.4% v/v PFA in 1X PBS for 30 s, permeabilized with 0.4% v/v Triton X-100 in 1X PBS for 3 min and fixed with 2.4% v/v PFA in 1X PBS for 30 min. Fixation was quenched by incubating with 100 mM ammonium chloride in 1X PBS for 5 min, followed by washing twice with 1X PBS for 5 min. The sample was blocked with Image-iT FX Signal Enhancer for 30 min, and then stained with 1 µM SNAP-Surface Alexa Fluor 647 in 1X PBS + 1 µM DTT + 0.5% w/v BSA for 2 h at room temperature. Excess unbound dye was removed by washing three times with 1X PBS for 5 min. Cells were then incubated for 10 min with 90 nm gold nanoparticles diluted 1:1 in 1X PBS, then washed three times with 1X PBS for 5 min to remove unbound nanoparticles. The sample was then mounted on a concave microscope slide, filled with blinking buffer containing 1X GLOX (0.4 mg ml^{-1} glucose oxidase, 64 µg ml^{-1} catalase), and 10-30 mM MEA in 50 mM Tris-HCl pH 8 + 10% w/v glucose, and sealed with Twinsil. The buffer was replaced approximately every 2 h to avoid unwanted blinking behavior due to pH drift caused by the oxygen scavenging system.

MINFLUX acquisitions

The acquisition for imaging follows the previous work [8]. For tracking, we first centered on the emitter(s) of interest in xy by moving the tip/tilt mirror controlled by a feedback loop and in z by deflecting the bottle beam. After converging to a location, the tracking took place within a “static” excitation pattern.

For detailed acquisition settings see Supplementary Note 4.

Live localization estimator

The live estimators utilized in all MINFLUX acquisitions reported in this work are from reference [8], except for the one associated with the excitation scheme comprising 7 Gaussian exposures positioned at the vertices and center of a regular hexagon, which we describe below:

$$\hat{\vec{r}} = -\frac{2^{\left[\left(\frac{L}{\mathrm{FWHM}}\right)^2-3\right]}\cdot\sqrt{\pi}\cdot\mathrm{FHWM}^3}{[\ln(2)]^{\frac{3}{2}}\cdot L^2}\left(\frac{1+\mathrm{SBR}}{\mathrm{SBR}}\right)\sum_{i=0}^{m-1}\hat{p}_i\cdot\vec{r}_i$$

where L is the hexagon radius, FWHM is the full width at half maximum of the focused 640 nm Gaussian beam in xy (280 nm in this work), SBR is the signal-to-background ratio, $\hat{p}_i = n_i/N$ is the estimated photon arrival probability of the i-th exposure, and $\vec{r}_i$ is the beam position of the i-th exposure.

Notably, we define the SBR from the maximum and minimum photon counts within a single excitation cycle: $\mathrm{SBR} = (n_{\max} - n_{\min})/n_{\min}$.

Data analysis

All acquired MINFLUX data was processed with custom processing software implemented in Python. The final localizations were estimated by maximum likelihood estimation implemented via a gradient descent on the likelihood function. For imaging, the processing followed the previous work[8]. The background localizations were filtered as listed in Supplementary Note 5. For tracking, see the remarks below.

Tracking

The raw photon counts underwent binning prior to localization estimation, allowing users to specify multiple binnings and thereby tailor the trade-off between spatial and temporal resolution during processing. For reporting localization precisions, we first applied a low-pass filter to the binned counts using a rolling window, and then ran a k-means cluster algorithm on the low-pass filtered counts. Subsequently, we computed standard deviations for each cluster and averaged the two resulting numbers for x, y, and z, separately. To report the distance between binding sites in the axial oscillator, we averaged each of the two clustered traces in groups of 20 localizations and then computed standard deviations. Only the dual-color origami was drift corrected by subtracting the trend obtained when fitting a fourth order polynomial to the x, y, and z trajectories, separately.

Extended Data

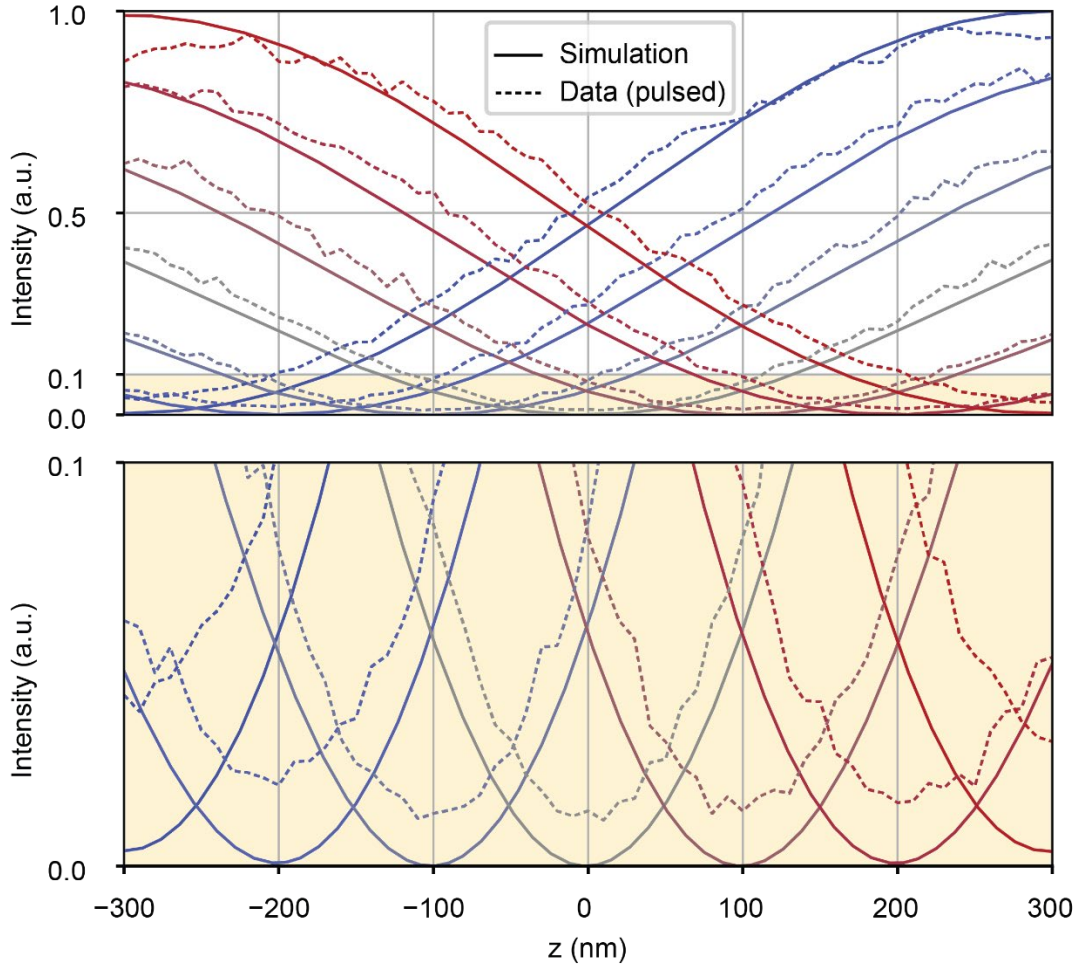

Extended Fig. 1. Pulsed-laser bottle beam deflection.
Juxtaposition of simulation and measurement with a pulsed excitation laser of intensity profiles for different positions of the deflected bottle beam zero. Bottom: zoom-in of the yellow area. A slightly stronger zero degradation than shown in Fig. 3**c** is visible for the measured data here.

References

1. Hell, S. W. & Wichmann, J. Breaking the diffraction resolution limit by stimulated emission: stimulated-emission-depletion fluorescence microscopy. Opt. Lett. 19, 780 (1994).
2. Hell, S. W., Jakobs, S. & Kastrup, L. Imaging and writing at the nanoscale with focused visible light through saturable optical transitions. Appl. Phys. Mater. Sci. Process. 77, 859–860 (2003).
3. Masullo, L. A. et al. Enhanced photon collection enables four dimensional fluorescence nanoscopy of living systems. Nat. Commun. 9, 3281 (2018).
4. Balzarotti, F. et al. Nanometer resolution imaging and tracking of fluorescent molecules with minimal photon fluxes. Science 355, 606–612 (2017).
5. Weber, M. et al. MINSTED fluorescence localization and nanoscopy. Nat. Photonics 15, 361–366 (2021).
6. Rust, M. J., Bates, M. & Zhuang, X. Sub-diffraction-limit imaging by stochastic optical reconstruction microscopy (STORM). Nat. Methods 3, (2006).
7. Betzig, E. et al. Imaging intracellular fluorescent proteins at nanometer resolution. Science 313, (2006).
8. Gwosch, K. C. et al. MINFLUX nanoscopy delivers 3D multicolor nanometer resolution in cells. Nat. Methods 17, 217–224 (2020).
9. Eilers, Y., Ta, H., Gwosch, K. C., Balzarotti, F. & Hell, S. W. MINFLUX monitors rapid molecular jumps with superior spatiotemporal resolution. Proc. Natl. Acad. Sci. U. S. A. 201801672 (2018) doi:10.1073/pnas.1801672115.
10. Wolff, J. O. et al. MINFLUX dissects the unimpeded walking of kinesin-1. Science 379, 1004–1010 (2023).
11. Deguchi, T. et al. Direct observation of motor protein stepping in living cells using MINFLUX. Science 379, 1010–1015 (2023).
12. Schmidt, R. et al. MINFLUX nanometer-scale 3D imaging and microsecond-range tracking on a common fluorescence microscope. Nat. Commun. 12, 1478 (2021).
13. Fiona Cole et al. Super-Resolved FRET and Co-Tracking in pMINFLUX. bioRxiv 2023.03.24.534096 (2023) doi:10.1101/2023.03.24.534096.
14. Bauer, B. W. et al. Cohesin mediates DNA loop extrusion by a “swing and clamp” mechanism. Cell 184, 5448-5464.e22 (2021).
15. Katan, A. J. & Dekker, C. High-Speed AFM Reveals the Dynamics of Single Biomolecules at the Nanometer Scale. Cell 147, 979–982 (2011).
16. Satyajit Maji, Jacob, P. & Brundavanam, M. M. Geometric Phase and Intensity-Controlled Extrinsic Orbital Angular Momentum of Off-Axis Vortex Beams. Phys. Rev. Appl. 12, 054053 (2019).
17. Propagation and focusing of optical fields. in Principles of Nano-Optics (eds. Hecht, B. & Novotny, L.) 45–85 (Cambridge University Press, Cambridge, 2012). doi:10.1017/CBO9780511794193.005.
18. Maurer, C., Jesacher, A., Bernet, S. & Ritsch-Marte, M. What spatial light modulators can do for optical microscopy. Laser Photonics Rev. 5, 81–101 (2011).
19. Balzarotti, F. et al. Nanometer resolution imaging and tracking of fluorescent molecules with minimal photon fluxes. Science 355, 606–612 (2017).
20. Reinhardt, S. C. M. et al. Ångström-resolution fluorescence microscopy. Nature 617, 711–716 (2023).
21. Chen, W., Zhang, Q., Natan, R., Fan, J. & Ji, N. Bessel-droplet foci enable high-resolution and high-contrast volumetric imaging of synapses and circulation in the brain in vivo. 2022.03.05.483143 Preprint at https://doi.org/10.1101/2022.03.05.483143 (2022).
22. Song, X., Wei, J., Teng, A. & Zhao, A. Controllable axial optical chain beams using a holographic method. Opt. Express 29, 17304–17315 (2021).
23. Turpin, A. et al. Optical vault: A reconfigurable bottle beam based on conical refraction of light. Opt. Express 21, 26335–26340 (2013).

24. Barbotin, A. et al. z-STED Imaging and Spectroscopy to Investigate Nanoscale Membrane Structure and Dynamics. Biophys. J. 118, 2448–2457 (2020).
25. Masullo, L. A. et al. Pulsed Interleaved MINFLUX. Nano Lett. 21, 840–846 (2021).
26. Leutenegger, M., Rao, R., Leitgeb, R. a & Lasser, T. Fast focus field calculations. Opt. Express 14, 11277–91 (2006).
27. Gao, P., Prunsche, B., Zhou, L., Nienhaus, K. & Nienhaus, G. U. Background suppression in fluorescence nanoscopy with stimulated emission double depletion. Nat. Photonics 11, 163–169 (2017).
28. Schueder, F. et al. An order of magnitude faster DNA-PAINT imaging by optimized sequence design and buffer conditions. Nat. Methods 16, 1101–1104 (2019).
29. Douglas, S. M. et al. Rapid prototyping of 3D DNA-origami shapes with caDNAno. Nucleic Acids Res. 37, 5001–5006 (2009).
30. Kim, D.-N., Kilchherr, F., Dietz, H. & Bathe, M. Quantitative prediction of 3D solution shape and flexibility of nucleic acid nanostructures. Nucleic Acids Res. 40, 2862–2868 (2012).

Super-resolved imaging of native mRNA ultrastructure

Authors: Alessandro Passera*, Paul Welzl*, Alba Gomez-Segalas, Clemens Plaschka, Francisco Balzarotti

*Authors contributed equally

Contributions: AP and FB conceived the combinatorial multiplexing strategies. CP and FB conceived and identified the application of the super-resolved combinatorial multiplexing strategies for mRNA ultrastructure visualization. AP designed mismatching imaging/handle pairs, designed and folded DNA origami, optimized protocols, performed all DNA origami experiments and their data analysis. AP designed and built the custom widefield optical system. AG and FB built the custom MINFLUX system and programmed the hardware control for the widefield and MINFLUX systems. AP, AG, and FB programmed the MINFLUX processing and visualization software. PW designed RNA-FISH probes, optimized the FISH protocols, performed widefield RNA-FISH experiments and their processing. AP and PW performed MINFLUX RNA-FISH experiments and processing. AP, PW, CP and FB wrote the manuscript. FB and CP supervised the project. All authors proofread and commented on the manuscript.

Relevance: The paper constitutes the culmination of my project, showing the design, development, and validation of the combinatorial DNA-PAINT technique. It describes a self-built super-resolution microscope and advanced 3D MINFLUX super-resolution imaging. It shows the first super-resolved imaging of nuclear and cytoplasmic mRNA ultrastructure, providing the basis for its study and first evidence of its role in mRNA biology.

Status: Submitted to Nature Methods on 18.12.2025. Published on bioRxiv on 23.01.2026

Super-resolved imaging of mRNA ultrastructure in cells

A. Passera[1,2,#], P. Welzl[1,2,#], A. Gomez-Segalas[1,2], C. Plaschka[1,*], F. Balzarotti[1,*]

[1]Research Institute of Molecular Pathology (IMP), Vienna BioCenter (VBC); Campus-Vienna-Biocenter 1, 1030 Vienna, Austria.

[2]Vienna BioCenter PhD Program, Doctoral School of the University of Vienna and Medical University of Vienna; A-1030, Vienna, Austria.

*Corresponding author. Email: clemens.plaschka@imp.ac.at; francisco.balzarotti@imp.ac.at

[#]These authors contributed equally to this work.

Abstract

Messenger RNA (mRNA) is a central polymer of gene expression, whose ultrastructure and defining regulatory rules remain unclear. To visualize the ultrastructure of mRNA, we here develop Combi-PAINT, a powerful and generalizable method for combinatorial super-resolved DNA-PAINT multiplexing, which we combine with high-efficiency RNA labelling and MINFLUX microscopy. This approach enables the nanometer-precision tracing of mRNA in three dimensions in cells. We use Combi-PAINT to visualize multiple distinct mRNA species inside the human cell nucleus and cytoplasm, revealing their quantitative ultrastructures and transcript-specific molecular patterns. By bridging sequence specificity with nanometer resolution, we provide a new lens for studying the cellular life of mRNA.

The three-dimensional organization of messenger RNA (mRNA) is critical for cellular function. mRNAs adopt secondary and tertiary structures and assemble with RNA-binding proteins (RBPs) into messenger ribonucleoprotein particles (mRNPs) (*1–5*), which govern fundamental processes such as RNA processing, packaging, diffusion, nuclear export, translation, and decay. Sequencing-based approaches can map RNA secondary structures (*6*), while atomic force microscopy has enabled the conformation mapping of very short RNA species *in vitro* (*9*). However, the direct visualization of the three-dimensional ultrastructure of mRNA inside cells—where they engage with cellular factors, undergo processing, and transport between subcellular locations—has remained a major challenge in RNA biology.

Electron microscopy has provided insights into the organization of mRNPs (*10*) and of cytoplasmic RNA through polysome imaging (*11*), leading to initial hypotheses of mRNA structure. Fluorescence *in situ* hybridization applied to RNA (RNA-FISH (*12*) and single molecule smRNA-FISH (*13*)) enables transcript-specific visualization of RNA molecules in cells. However, insights into mRNA ultrastructure have been limited to diffraction-limited imaging approaches, and to the analysis of one-dimensional end-to-end distances within transcripts (*14*).

Super-resolution microscopy (SRM) (*15*, *16*) has unlocked optical access to the sub-hundred nanometer scale in cell biology, and spurred efforts to determine the distribution and colocalization of proteins in cells and tissue (*17*). Among SRM techniques based on single-molecule localization (SMLM) (*18–20*), DNA-PAINT (*21*) is widely adopted for its multiplexing capabilities (*22–24*), quantitative molecular counting (*25*), and sub-nanometer precision (*26*).

SRM has enabled optical chromatin tracing (*27*), unveiling biological insights of chromatin organization (*28–31*). In contrast, super-resolving an RNA molecule has lagged behind, owing to high RNA-FISH primary probe densities, and stringent resolution requirements. RNA imaging has been carried out using stimulated emission depletion microscopy (*32*), expansion microscopy (*33*, *34*) and DNA-PAINT (*30*, *35*), with recent efforts targeting small RNAs (*36*) through specialized labelling design utilizing nucleotide analogs. While these approaches improved measurements of the cellular distribution of RNA, none have thus far addressed the ultrastructure of single RNAs at sub-transcript resolution.

In this work, we tackle this gap by developing a novel DNA-PAINT combinatorial multiplexing technique, Combi-PAINT, that enables the fast, multiplexed imaging with reduced sample perturbations. We apply Combi-PAINT to mRNA ultrastructure imaging with widefield and MINFLUX SRM modalities, showing the sub-transcript spatial organization of multiple mRNAs in the human cell nucleus and cytoplasm. We find differences in size, shape, and compaction for transcripts of different genetic architecture, which are enabled by a sub-diffraction view of mRNA. Taken together, Combi-PAINT and optical RNA ultrastructure analysis provide the first, to our knowledge, ultrastructural view of mRNA in cells and a generalizable platform for the ultrastructural imaging of any nucleic acid.

Results

Combinatorial multiplexing for DNA-PAINT super resolution imaging

DNA-PAINT exploits the transient binding of fluorescent DNA strands (‘imagers’) to their complement (‘handles’), attached to molecules of interest, to achieve the emitter sparsity, or ‘blinking’, necessary for SMLM. However, conventional DNA-PAINT multiplexing requires a number of imaging rounds that scales linearly with the number of desired imaging targets (*22–24*).

To simplify and accelerate high-target number DNA-PAINT imaging, we developed a combinatorial DNA-PAINT multiplexing approach (Combi-PAINT) in which a handle strand, coupled to a target, can recruit more than one imager strand (Handle AB in Fig. 1A). This strategy simplifies DNA-PAINT workflows and increases the number of resolvable targets without increasing the number of imaging rounds (*22*, *37*). At the single-molecule level, the colocalization of signals from multiple imagers encodes for target identity (Fig. 1B). For example, two imagers (A and B) suffice to discriminate three

targets (A, AB, B in Fig. 1B, top); by direct generalization to N imagers, a binary mapping enables 2^N-1 targets. Moreover, allowing arbitrary stoichiometries of imager binding sites on the same handle strand (Fig. 1B, bottom) relaxes the binary mapping constraint, enabling the number of distinguishable handles to grow beyond exponential scaling.

We present two avenues to implement the Combi-PAINT concept (Fig. 1A): (i) a “mismatch-based” design, which exploits engineered base-pair mismatches to yield handle-imager pairs of comparable binding kinetics, and (ii) a “module-based” design, in which handles concatenate short motifs that independently recruit distinct imagers.

Mismatch-based Combi-PAINT requires handle sequences to deviate from exact complementarity, reducing binding stability, which is compensated by increasing sequence length. By choosing the position of base-pair mismatches appropriately, distinct imagers can be programmed to bind to the same handle, allowing combinatorial multiplexing. We devised a computational pipeline for the rational design of such DNA strand families (Fig. 1C, Methods). The pipeline is seeded with randomized DNA sequences constrained by an analytic model of nucleotide dependencies that enforces a binary mapping between imagers and handles (Extended Data 1). This first *in silico* screen yields pseudo-orthogonal imager sets (ImA, ImB, ImC) and their corresponding handles (HnA, HnB, HnC, HnAB, etc.). As the analytic model does not predict realistic DNA-DNA binding, we produced a second *in silico* screen utilizing NUPACK (*38*). Here, the entire handle space (~70M combinations) was compared against the chosen imager sets, in search of uniform binding-energies, high off-target rejection and low self-interactions (Extended Data 2, Supplementary Table 1). Candidate handles were experimentally validated on DNA origami (*39*) by measuring their binding kinetics (Supplementary Table 2). From these, we selected an optimized six-handle set (Extended Data 3, Supplementary Table 3, Supplementary Table 4 , Supplementary Table 5), of which a subset is shown (Fig. 1D) to highlight the mismatch distribution.

We generated families of fluorogenic mismatch-based Combi-PAINT imagers spanning different spectral ranges by appending a quencher at the end of the strand opposite to the fluorophore, thereby suppressing background fluorescence from unbound strands (*40*) (Supplementary Fig. S1, Supplementary Fig. S2, Supplementary Table 5). To validate multiplexing performance, we imaged a mixed sample of six distinct 20-nm grid origamis, one per mismatching handle, over three rounds of Exchange-PAINT imaging (Fig. 1G). For each binding site, identity was inferred from a multinomial distribution model of binding events and compared with the ground truth defined by the origami template (Fig. 1H). The resulting confusion matrix demonstrated high (85-95%) sensitivity even at low coverage (>15 binding events per site; Fig. 1I). In parallel, this experiment provided binding kinetics and photophysical parameters of all imager-handle pairs simultaneously (Extended Data 4, Extended Data 5, Supplementary Table 6, Supplementary Table 7). MINFLUX imaging of the nuclear pore complex (*41*) utilizing these imagers exhibited clearly localized clusters (Supplementary Fig. S3).

The second avenue, module-based Combi-PAINT, uses conventional DNA-PAINT handles (*42*) in combined concatenations (Fig. 1A). Given its capability of encoding more than 2^N-1 handles through arbitrary ratios of binding sites for different imager strands, we aimed to identify optimal stoichiometries. We explored this design space with a maximum-likelihood classifier that computes the classification error as a function of stoichiometry, number of targets, and number of binding events (Extended Data 6, Extended Data 7). A subset of this analysis (Fig. 1F) shows the efficiency of the optimal strategies to address 6-, 9-, 12-, and 15-target imaging with three imager strands, which can be decoded with tens of binding events. Increasing the number of imagers to six (*43*), allows up to 63 targets (Supplementary Fig. S4). We employed the three established purine-only imagers to leverage the rapid imaging capabilities of single-class nucleobase strands (*43*) after checking their binding modes (Supplementary Fig. S5).

We characterized the performance of the 6- (Fig. 1J) and 9- (Fig. 1M) target strategies with a similar experiment to the one for mismatch-based Combi-PAINT, but with each individual origami harboring all the handle types. We created a Python pipeline to extract the ground truth identity of the handles from their position on the DNA origami, as well as the number of binding events. The resulting ternary plots (Fig. 1K,N) and confusion matrices (Fig. 1L,O) show high (90-95% and 80-95% for the 6- and 9-color strategies, respectively) sensitivity.

Taken together, we present two strategies, mismatch- and module-based, to perform novel combinatorial DNA-PAINT multiplexing, which we call Combi-PAINT. We show that three imagers can combinatorially encode double and triple the number of targets compared to a non-combinatorial approach. Module-based Combi-PAINT, due to the larger number of available speed-optimized imager strands, presents a higher ceiling to the possible number of addressable targets (Supplementary Fig. S4, Discussion). Mismatch-based Combi-PAINT, on the other hand, excels in background-heavy environments and in the absence of optical sectioning due to the fluorogenicity of its imager strands. Furthermore, while we tested both mismatch- and module-based handles for the purpose of RNA labelling, we found that module-based handles introduced undesired nuclear background under RNA-FISH conditions (Supplementary Fig. S6); however, they remain fully effective for non-nuclear targets and samples that do not undergo FISH hybridization.

Super-resolved RNA-FISH reveals mRNP morphology

We next integrated Combi-PAINT with RNA-FISH to directly visualize mRNAs in human cells. In conventional smFISH, fluorescent oligonucleotide probes hybridize with complementary mRNA sequences, providing transcript-specific signals at diffraction-limited resolution. In our design, each probe carries two single-stranded DNA extensions flanking the mRNA-binding region: one which engages the smFISH probe, serving as an intrinsic positive controls of RNA presence, and one which supports either the mismatch- or module-based Combi-PAINT readout as described above (*44*) (Fig. 2A).

As a first demonstration, we targeted MDN1, a well-studied 18 kb-long transcript, which was previously used as a model mRNA due to its large size, moderate copy number in cells and balanced nuclear/cytoplasmic localization to benchmark RNA structure in one dimension (*14*). We designed 200 homology sequences with OligoMiner aiming to sample the mature transcript as uniformly and selectively as possible, and appended with smFISH and mismatch-based Combi-PAINT handles (Methods). The RNA-FISH protocol was optimized for signal-to-background ratio and includes a shielding step (*45*) to reduce nuclear background (Supplementary Fig. S7). These optimizations allowed a clear identification of individual transcripts in high-quality smFISH (Fig. 2B, left) and their super-resolved reconstruction by DNA-PAINT (Fig. 2B, right) with high precision (NeNA (*46*): σ = 4-6 nm), even in the high-background nuclear environment, allowing, for the first time, direct visualization of RNA morphology in two dimensions.

To investigate whether different mRNA species follow different ultrastructural rules, we imaged two additional transcripts that differ in their genomic features (Fig. 3A, Supplementary Fig. S8). Alongside MDN1, a long transcript with high intron density (101 splice junctions), we selected AHNAK1, an mRNA of comparable length (18,761 bp) but with low intron density (4 splice junctions, localized at the 5' end). We also imaged EPRS1, which is of average mRNA length (4,300 nucleotides) but has a high intron density (31 splice junctions). RNA-FISH probes (MDN1: 200, AHNAK1: 98, EPRS1: 46) were uniformly distributed across each mRNA. Each mRNA was then split into three segments containing equal numbers of probes, and the probes of each segment were equipped with the same Combi-PAINT handle. Notably, this arrangement differs from simply interleaving RNA-FISH probes with different conventional DNA-PAINT handles along the transcript, as the stochasticity of probe binding cannot ensure true colocalization of signals, which is a unique feature of Combi-PAINT (Supplementary Fig. S9).

We acquired widefield RNA-FISH DNA-PAINT data over three rounds of Exchange-PAINT separately for each gene (Fig. 3A). The resulting localization clouds were analyzed with a custom pipeline that extracted particle features from single mRNPs (Fig. 3B; Methods). To capture their shapes, we quantified 5'-3' end-to-end distance, as in classical smFISH, and additional descriptors including covariance-based size and aspect ratio, as well as higher moments such as kurtosis (Fig. 3B). Particles were separated into nuclear and cytoplasmic fractions (Fig. 3C), anticipating morphological changes following export and translation due to ribosome engagement with mRNA.

End-to-end distances, which are measurable even without super-resolution, reveal mRNA species-specific behaviors (Fig. 3D). MDN1 showed a pronounced increase in extension from nucleus to cytoplasm, consistent with previous reports (*14*). In contrast, EPRS1 and AHNAK1 exhibited little or no detectable change. Based on this metric alone, one might conclude that MDN1 undergoes compaction changes upon nuclear export, while the other transcripts remain unchanged.

Super-resolved data provided a richer picture (Fig. 3E-G). Both EPRS1 and MDN1 transcripts increased in major axis size from nucleus to cytoplasm, while AHNAK1 remained unchanged (Fig. 3E). This indicates that transcript length by itself may not dictate the degree of compaction. The aspect ratio analysis revealed another pattern (Fig. 3F): in the nucleus, EPRS1 and MDN1 formed extended globule-like structures, whereas AHNAK1 showed a higher degree of elongation. This indicates that intron density may impact mRNP ultrastructure, consistent with biochemical data indicating a role of the splicing-dependent exon junction complex in mRNP packaging (*4*). The aspect ratios of each mRNP were markedly higher than 1, suggesting that mRNPs adopt different degrees of extended, rod-like structures, consistent with a sequencing-based assay (*47*). A strong change in aspect ratio between nucleus and cytoplasm was observed only for MDN1, while the other transcripts showed similar and unchanged aspect ratios. The lack of change in aspect ratio for cytoplasmic EPRS1 may be attributed to its smaller size, which limits ribosome occupancy and preserved its extended globule-like shape. In contrast, we speculate that the low number of introns of AHNAK1 compared to MDN1 may minimize AHNAK1 compaction in the nucleus. We expect that the imaging of additional RNA species may reveal general rules of mRNA ultrastructure regulation, for example, the relationship between intron density and aspect ratio.

Higher-order moment analysis reinforced these trends (Fig. 3G). Kurtosis distributions showed a consistent shift across the three transcripts: cytoplasmic localization patterns became more tail-heavy, reflecting increased RNA density at the particle periphery. This shift provides additional evidence that mRNPs undergo conformational changes during and following export. While AHNAK1 did not exhibit detectable changes in the other metrics described above when transiting from nucleus to cytoplasm, it did show a significant change in kurtosis distribution similar to the other transcripts, suggesting that this metric reflects some common event across all transcripts, such as translation.

Finally, we leveraged the combinatorial nature of Combi-PAINT to perform simultaneous RNA-FISH of all three segmented transcripts. Each one was labelled with a different assignment of Combi-PAINT handles, such that one imager binds to the entire transcript, while the other two bind to the 3' and 5' ends (see cartoon of labeling scheme, Fig. 3H, right). Over three rounds of imaging (Fig. 3H, left), the different stoichiometry signatures enabled blind assignment of both transcript identity and subregion, as confirmed by ternary plots of binding-event distributions (Fig. 3H, right, Extended Data 8), showcasing another example of 9-target multiplexing.

Taken together, these results reveal that different human mRNAs adopt distinct ultrastructural properties, some of which may be influenced by subcellular localization and processing events.

Three-dimensional MINFLUX imaging of mRNAs

We next aimed to adapt Combi-PAINT to enable three-dimensional (3D) interrogation of mRNP ultrastructure. Since mRNPs are small, 50 nm to 200 nm particles without a preferential orientation in space, they require an imaging method capable of delivering isotropic, few-nanometer precision in all three dimensions on a densely labeled object—an ability unique to MINFLUX, a single-molecule localization strategy that achieves nanometer precisions in 3D by sequentially interrogating the position of fluorescent emitters with a structured beam of focused light.

The nuclear environment poses challenges for this method due to its high background. (Methods, MINFLUX RNA-FISH imaging). To overcome this, we first optimized the MINFLUX targeted-coordinate-pattern (TCP) size L (Fig. 4A) to retrieve high-photon counts, with a large $L = 150\ \mathrm{nm}$ yielding superior localization precision and greater robustness to imperfect convergence onto the fluorophore. Second, axial convergence was achieved through a feedback loop, which proved more resilient to variable out-of-focus background binding events than conventional feedforward approaches. Finally, our custom MINFLUX microscope (*48*) allowed mixing distinct excitation beam shapes within a single MINFLUX cycle; combining donut and top-hat beams for lateral and axial localizations, respectively, provided a more photo-efficient MINFLUX scheme, useful for operation in the noisy nuclear environment (Fig. 4A).

With these improvements, we imaged nuclear and cytoplasmic MDN1 and AHNAK1 transcripts *in situ* (Fig. 4B-E, Movies S1-4, Extended Data 9) at 2 nm localization precision per-axis, corresponding to 4–5 nm resolution in 3D. MDN1 reconstructions revealed a modular arrangement: transcript segments occupy discrete, minimally overlapping volumes, and cytoplasmic particles are overall larger than their nuclear counterparts. This is reflected in the proximity matrices (Fig. 4C,E), which show limited co-occurrence between the ImB and ImC rounds, which labelled the 5’ and 3’ ends respectively and are not expected to colocalize at the single-probe level due to the Combi-PAINT handles distribution. Colocalization of the ImA round with the ImB/ImC rounds is instead expected and can be visually confirmed. In line with widefield MDN1 data the overall size of the particle increases in the cytoplasm. The AHNAK1 reconstructions also confirm the widefield data, showing similar particle sizes and elongation in the nucleus and cytoplasm (Fig. 4F-I). Interestingly, the increased spatial resolution from 3D MINFLUX allows to appreciate a common feature of AHNAK1 cytoplasmic particles, which assume highly curved shapes, with gaps devoid of RNA signal, possibly owing to competition with the translation machinery or other cytoplasmic RNA-binding proteins.

In summary, we introduce a new DNA-PAINT multiplexing method, Combi-PAINT, that is compatible with smRNA-FISH and MINFLUX imaging and allows faster imaging, allowing us to produce the first low-nanometer-resolution 3D images of nuclear and cytoplasmic mRNA in human cells.

Discussion

We developed a complete workflow that both advances super-resolution methodology and delivers nanometer-resolved RNA imaging *in situ*. Combi-PAINT enables dense, faster multiplexed labeling, and—paired with iterative 3D MINFLUX—yields segmented reconstructions of human mRNAs and, to our knowledge, the first nanoscopic 3D views of mRNP ultrastructure inside intact cells. Together, these advances turn studies of mRNA from a diffraction-limited blur into quantifiable particles with shape, size and internal organization.

Combi-PAINT is a general combinatorial multiplexing concept for DNA-PAINT. We implemented it in two ways—mismatch-based and module-based—and established a rational design pipeline that produces families of orthogonal, fluorogenic imagers. Practically, this increases the number of addressable targets without a proportional increase in imagers or exchange cycles, reducing washes, background and drift while remaining compatible with sequential Exchange-PAINT and unmixing approaches based on spectra and fluorescence lifetime (*49*, *50*). In the future, larger libraries of orthogonal, speed-optimized or chemically modified fluorogenic strands should enable scalability to

the hundreds, and potentially thousands, of targets (*51*); integration with RESI (*26*), FLASH-/SUM-PAINT (*23*, *24*) and related strategies can further expand resolution and multiplexing; and incorporating additional observables (spectra, lifetime, brightness (*52*)) plus colocalization-aware clustering (e.g., BaGoL inference (*53*)) will harden classification. Because the principle is sequence-agnostic, we expect that Combi-PAINT will generalize to nanoscale chromatin tracing and mapping protein complex stoichiometry and organization.

Super-resolved RNA-FISH coupled to Combi-PAINT reveals transcript-specific particle morphologies in both nucleus and cytoplasm. The level of compaction of mRNAs in the nucleus may correlate with intron density, consistent with a model for exon-junction-complex–mediated packaging of mRNAs (*4*), whereas cytoplasmic particles exhibit a common morphology, likely imposed by translation. Future imaging of many more, and distinct, RNA species will be necessary to investigate global regulatory rules of mRNA ultrastructure. Beyond the traditional end-to-end distance metric, shape descriptors (e.g., covariance-based size, aspect ratio, higher moments such as kurtosis) provide a richer vocabulary for mRNP ultrastructure, and enable studying the effect of genic features and mRNP composition on the functional mRNA ultrastructure in cells. Notably, the application of DNA-PAINT to RNA we present here is applicable to any RNA target that can be probed by FISH, given enough probes can be generated.

The powerful new toolkit developed here enables the study of RNAs at the nanoscale within intact cells. These methods will facilitate systematic, multi-gene surveys to connect mRNA ultrastructure with gene regulation, cellular function and disease, and to uncover the mechanisms and rules that govern the mRNA life cycle. Similar to how DNA tracing revolutionized our understanding of genome architecture (*28*, *54*), we establish a path to uncover the ultrastructural cell biology of RNA.

Figures

Figure 1

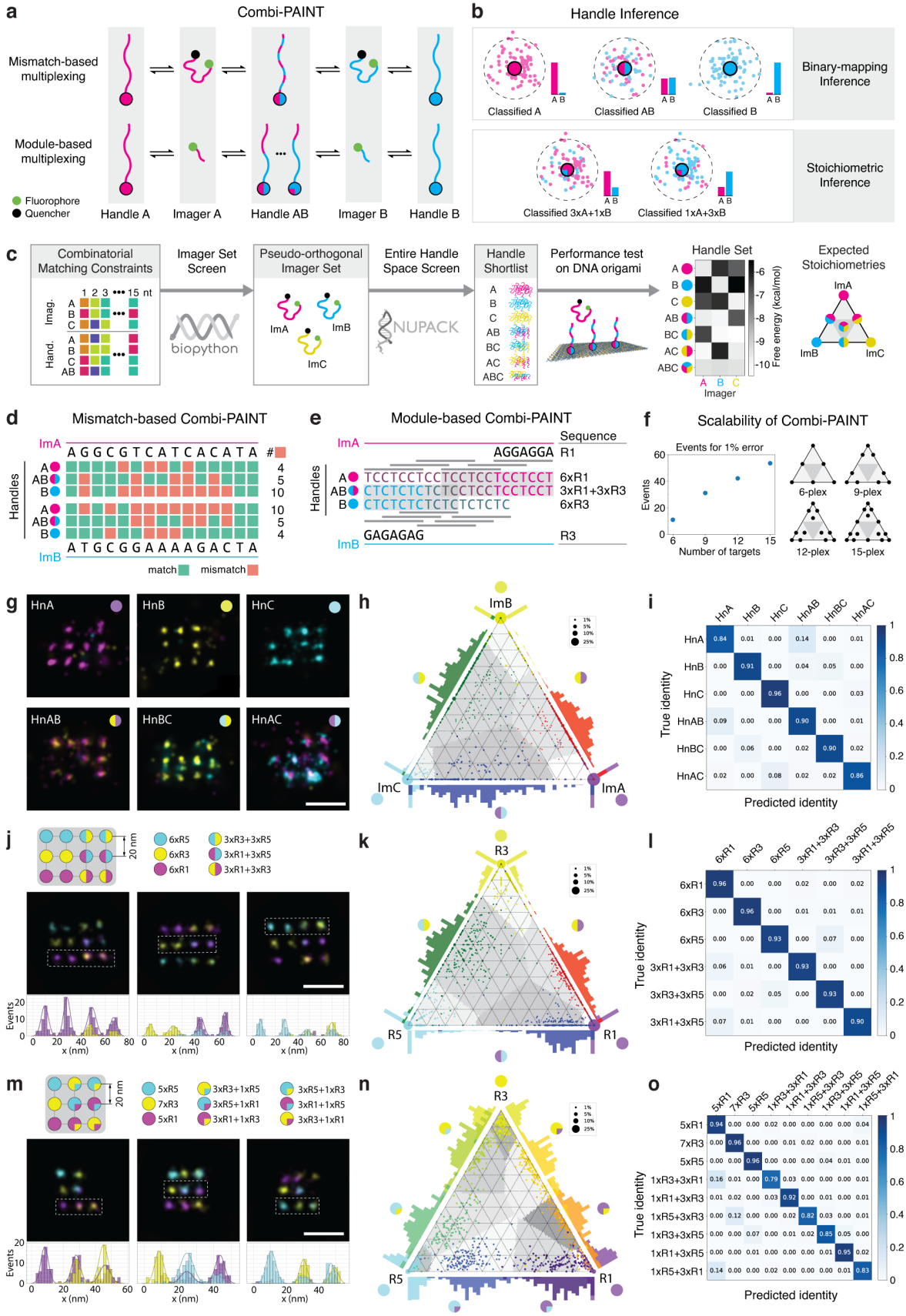

Fig. 1. Combinatorial DNA-PAINT multiplexing. (**A**) Concept: *de novo* target DNA handles are designed to bind transiently to several DNA imagers, e.g. handle "AB" binds imagers "A" and "B". Handle-imager pairs are designed by either (top) distributing base mismatches or (bottom) concatenating short modules. (**B**) The handle inference through classification of clustered localizations can assume either (top) binary-mapping with identical stoichiometries or (bottom) arbitrary stoichiometries of imager mixtures. (**C**) Computational pipeline for designing fluorogenic mismatch-based Combi-PAINT strand families (see Methods). The heatmap on the right shows the binding energy of each imager-handle pair, while the ternary plot shows the position of the handles, represented in the same color scheme as in the matrix, given the proportion of binding to each imager strand. (**D**) Mismatch arrangement of HnA, HnB and HnAB with ImA and ImB. The different arrangement of mismatches between ImA and ImB for HnAB is shown, as well as the much higher number of mismatches for HnA-ImB and HnB-ImA. (**E**) Imager binding pattern of Module-based Combi-PAINT, showing the partial overlap of the binding motifs to reduce handle length. (**F**) Example of scalability of Module-based Combi-PAINT exploiting binding stoichiometry. The plot on the left is a subset of , showing only the optimal scheme for each number of targets. The y-axis represents the number of events needed to achieve a 1% error probability for each target classification in the scheme. The diagrams on the right show the position, in a ternary plot, of each handle species in each scheme. (**G**) 6-color mismatch-based Combi-PAINT; a mixture of DNA origamis with a 20 nm-spaced grid for each handle type were imaged simultaneously over three rounds of exchange-PAINT with each imager: ImA (magenta), ImB (yellow), ImC (cyan). Scalebar: 50 nm. (**H**) Ternary plot representation of classification. Dot coordinates $(p_{ImA}, p_{ImB}, p_{ImC})$: recorded fraction of each imager per binding site. Color represents ground-truth: HnA (magenta), HnB (yellow), HnC (cyan), HnAB (red), HnBC (green), HnAC (blue). Dot size: fraction of entire population. Target classification is done according to the shaded gray areas, which represent maximum-likelihood classification. DNA-origami for each type: n_{HnA} = 356, n_{HnB} = 424, n_{HnC} = 543, n_{HnAB} = 638, n_{HnBC} = 1026, n_{HnAC} = 199. (**I**) Confusion matrix of the classification. Rows may not sum to 1 due to rounding errors. (**J-L**) Equivalent to (G-I) for Module-based Combi-PAINT for six targets; (J, top) diagrams of origami handle arrangement; (J, bottom) line profile from the localizations in the dashed rectangle. N=136 origamis. Scalebar: 50 nm. (**M-O**) Equivalent to (J-L) for Module-based Combi-PAINT for nine targets. N=253 origamis. Scalebar: 50 nm.

Figure 2

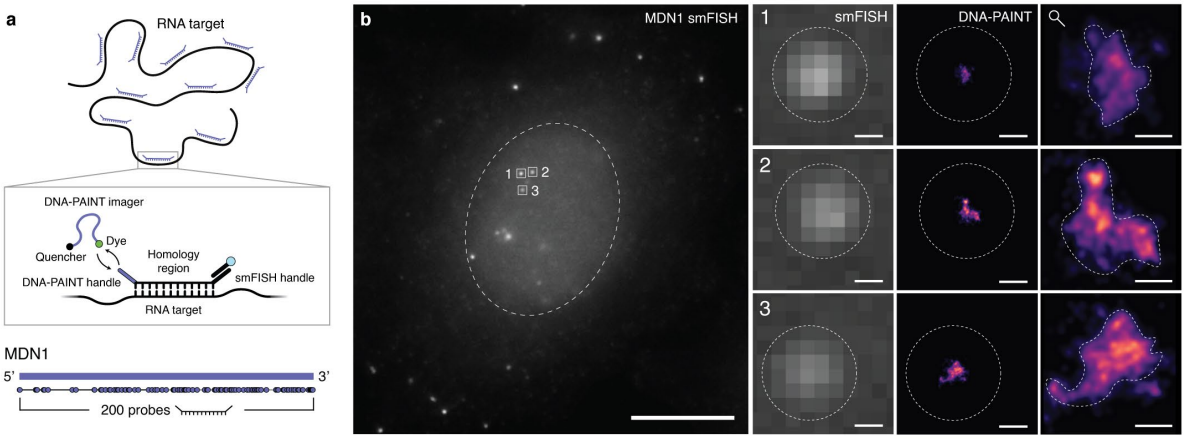

Figure 2. Super resolving mRNA by combining DNA-PAINT and RNA-FISH. (**A**) Cartoon of the RNA-FISH labelling strategy employed and of RNA-FISH probe distribution along the mature MDN1 transcript. (**B**) Left: diffraction-limited single-molecule FISH (smFISH) overview of a cell labelled with RNA-FISH for the MDN1 mRNA. Right, first column: zoom-in of three distinct MDN1 mRNAs marked in the overview; second column: single-color super-resolved DNA-PAINT image at the same scale; third column: zoom-in of DNA-PAINT images with a dashed contour marking the RNP region. Scalebar: 10 µm (cell overview), 200 nm (first and second columns), 50 nm (third column).

Figure 3

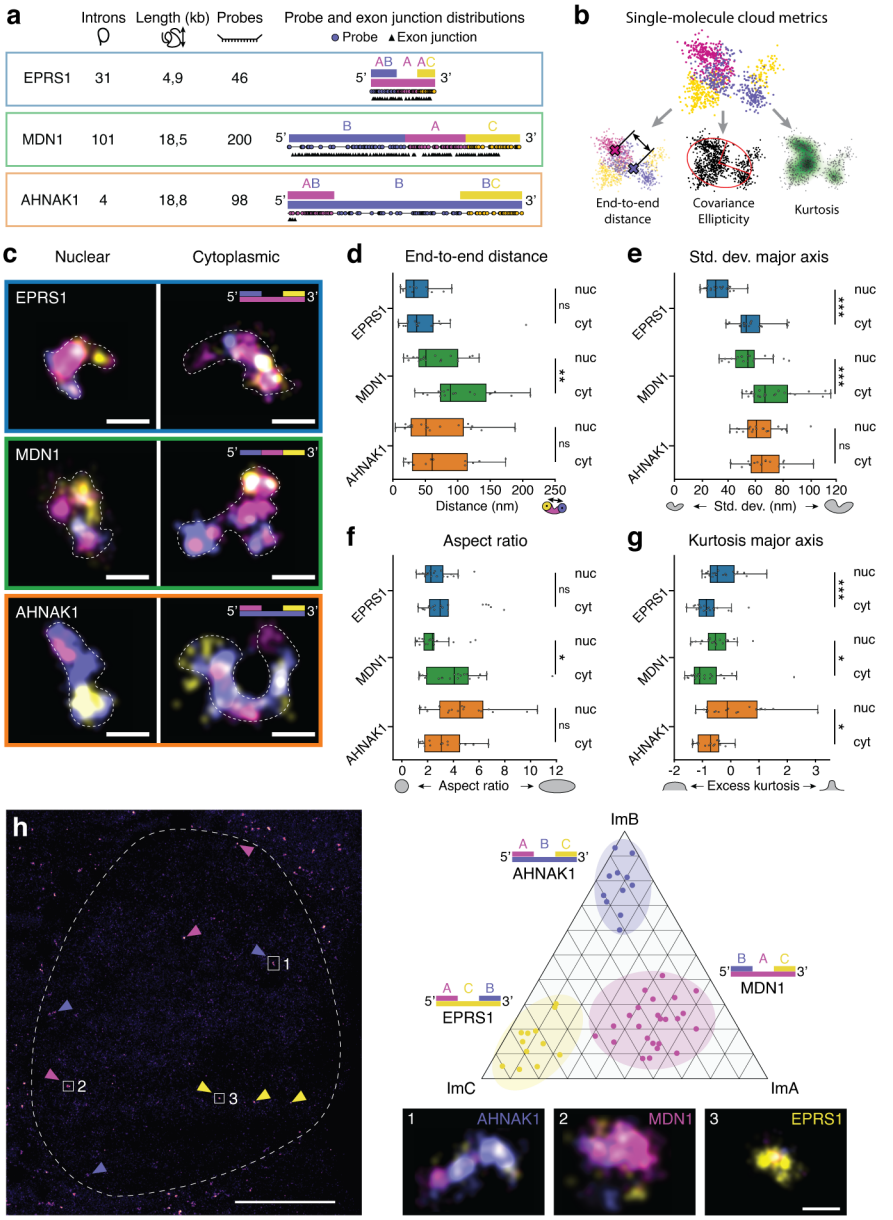

Figure 3. Morphology assessment of distinct mRNAs. (**A**) Overview of the investigated mRNAs' properties: number of introns, length of the mature transcript, number of designed RNA-FISH probes and sequence map highlighting probe positions (circles) and splice junctions (triangles). (**B**) Extracted metrics from each RNP's localization cloud. (**C**) Representative combinatorial DNA-PAINT images of RNPs of each of the three genes in the nucleus and cytoplasm, with a dashed contour marking the RNP region. Magenta: ImA, lilac: ImB, yellow: ImC. Scalebar: 100 nm. (**D-G**) Plots of 5'-3' end-to-end distance (D), major axis standard deviation (E), aspect ratio (F) and major axis kurtosis (G) of the three genes in the nucleus and cytoplasm. *: p<0.05, **: p<0.01, ***: p<0.001, n.s.: non-significant. Data from N>3 experiments per RNA, no. of particles MDN1 nuclear: N=21, MDN1 cytoplasm: N=23, AHNAK1 nuclear: N=20, AHNAK1 cytoplasm: N=17, EPRS1 nuclear: N=22, EPRS1 cytoplasm: N=21. (**H**) Combi-PAINT RNA-FISH image. Left: overview of the cell with nuclear area outlined by the dashed line. A zoom-in of the nuclear numbered particles is shown on the right. Arrowheads show other particles classified in the experiment (magenta: MDN1, lilac: AHNAK1, yellow: EPRS1). Right: ternary plot showing the proportion of binding of each imager strand to each RNP, represented by a single dot.

Classification is performed via DBSCAN clustering. Data from N=3 experiments. Scalebars: 5 µm (left), 100 nm (right).

Figure 4

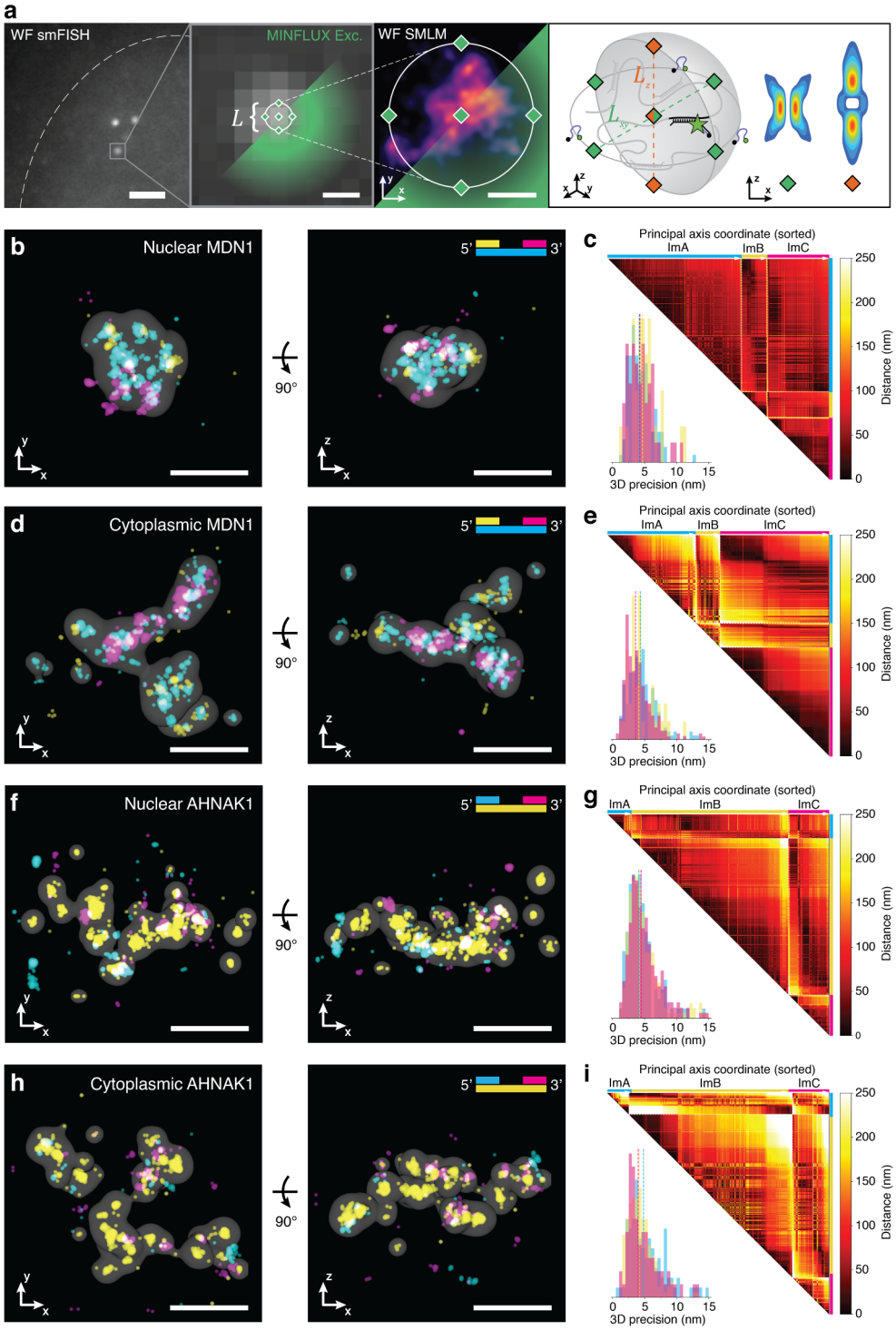

Figure 4: 3D MINFLUX imaging of DNA-PAINT RNA-FISH in the nucleus and cytoplasm. (**A**) 3D MINFLUX imaging context. A region of interest chosen by its smFISH signal, is then targeted with iterative 3D MINFLUX imaging. The right panel shows the arrangement of the MINFLUX beams. Green diamond: donut beam, orange diamond: top-hat beam. Scalebars: 2 µm (left), 200 nm (center), 50 nm (right). (**B,D,F,H**) xy and xz projections of single MDN1 RNPs in the nucleus (B) and cytoplasm (D) and of single AHNAK1 RNPs in the nucleus (F) and cytoplasm (H). The shaded volume is a thresholded large-sigma smoothing of the ImA (B,D) or ImB (F,H) rounds, which encompassed the whole MDN1 (B,D) or AHNAK1 (F,H) particles, respectively. Scalebar: 100 nm. (**C,E,H,I**) (top) Pairwise distance matrices of the

measurements in (B,D,F,H). Each line/column represents a single binding event. Binding events from the same imaging round are grouped together and separated by a dashed line, and each group is internally sorted by first principal component coordinate. (bottom) 3D localization precision achieved in each round of imaging (typically 4-5 nm). Imagers: ImA (cyan), ImB (yellow), ImC (magenta).

Methods

Widefield microscopy setup

The widefield microscope used for DNA origami experiments was custom built. The light from a Cobolt Jive 150 (0561-04-01-0150-699, Cobolt) was coupled into a polarization-maintaining single-mode fiber (P3-405BPM-FC-5, Thorlabs) using a fiber collimator (60FC-4-M6.2-33, Schäfter+Kirchoff). The output of the fiber was collimated using a 150 mm lens (AC254-150-A-ML, Thorlabs). A cleanup filter (FF01-561/14-25, Semrock) was used to reject any fiber-induced fluorescence. The collimated light was focused by a 400 mm lens (AC254-400-A-ML, Thorlabs) to the back focal plane of a high-numerical aperture oil objective (UPLXAPO60XO, Olympus) after being reflected by a TIRF-suitable dichroic mirror (ZT488/561rpc, Chroma) and passed through a quarter-wave plate (AQWP10M-580, Thorlabs) to induce circular polarization. Between the laser source and the 400 mm focusing lens, a mirror was placed one focal length away from the lens and mounted on a tip/tilt kinematic mirror mount (KM100, Thorlabs), allowing to move from epi-fluorescent illumination to TIRF illumination without displacing the illumination zone. The fluorescence light was passed through a 200 mm 1:1 telescope (2x AC254-100-A-ML, Thorlabs), a 800 nm short-pass filter (FESH0800, Thorlabs) to reject infrared light for the active stabilization, and a dual-notch filter (ZET488/561m, Chroma) to reject residual laser light. The image was formed by focusing with a 150 mm lens (AC254-150-A-ML, Thorlabs) on a PCO panda 4.2 bi camera (Excelitas) or with a 60 mm lens (AC254-060-A-ML, Thorlabs) on PCO edge 2.6 camera (Excelitas) depending on the experiment, leading to a pixel size of 125 and 121 nm respectively. The sample was mounted on a coarse xy stage (M-545.2ML, with M229.25S linear actuators and C-663.11 controllers, Physik Intrumente), itself mounted on a fine xyz stage (P-545.3D8S with E-727 controller, Physik Instrumente), used for active stabilization of the sample. The objective was mounted on a coarse z actuator (L-505.013212F with C-863.12 controller, Physik Instrumente), used for coarse z adjustments. The active stabilization module consists in a darkfield infrared scattering microscope and focus-lock system and is a copy of the one deployed on the MINFLUX setup and described in (*48*). The only modifications in this setup are the z stabilization laser (LuxX 945-200, Omicron) and the coupling/collimation of the z stabilization laser before/after the fiber (60FC-4-A6.2S-02 for both, Schäfter+Kirchoff). The module allows fine (sub-nanometer) and fast (10 Hz) adjustments in xyz of the sample, minimizing short-term drift and maintaining the focus. Residual long term drift (< 25 nm over 1 hour) was corrected in post-processing.

For initial characterization of the imaging strands, as well as widefield DNA-PAINT RNA-FISH, an Elyra 7 microscope (Zeiss) was used. The microscope is equipped with a PCO edge 4.2 camera (Excelitas) and a 63x/1.4 NA plan-apochromat oil immersion objective (Zeiss).

MINFLUX microscopy setup

The MINFLUX microscope used in this study is described in (*48*).

Reagents

M13mp18-derived p7249 scaffold (N4040S) was obtained from NEB. Unmodified and biotinylated oligonucleotides (DNA origami staples) were ordered from MWG Eurofins. Azide-modified oligos for conjugation were obtained from Metabion. Other modified oligos for conjugation were ordered from Sigma Aldrich. BHQ2- and BHQ3-modified oligonucleotides were obtained from Biosearch Technologies. IowaFQ-modified oligonucleotides were obtained from IDT. Cy3b-NHS ester (29320) was obtained from Lumiprobe. ATTO488-maleimide (AD 488-41) and ATTO643-maleimide (AD 643-41) were obtained from ATTO-TEC. TCEP hydrochloride (C4706-2G), dimethylformamide (DMF) (227056-100ML), dithiothreitol (DTT) (D0632-5G) and DBCO-PEG4-maleimide (760676-1MG) were obtained from Sigma Aldrich. Absolute ethanol (1009831000) and ammonium chloride (1011451000) were obtained from Merck. Sodium bicarbonate (27778293) was obtained from VWR. Anti-GFP nanobody (N0305) was obtained from NanoTag. Tris-HCl 1 M pH 8, 10x and 1x PBS pH 7.3, 1x TAE pH 8, 1 M HEPES pH 7.3, EDTA 0.5 M pH 8, 1 M magnesium chloride, 1 M potassium chloride and 5 M sodium chloride were obtained from our in-house media kitchen. Pure water was obtained from a MilliQ water

filtration system. Neutravidin protein (31000) was obtained from Thermo Scientific. Polyethylene glycol (PEG)-8000 (P2139-500G) and Bovine Serum Albumin-biotin (BSA-biotin) (A8549-10MG) were obtained from Sigma-Aldrich. µ-Slide 8 Well High Glass Bottom (80807) and µ-Slide I Luer Glass Bottom (80177) were obtained from Ibidi. Square #1.5 coverslips (MENZBB024024AC23) and round #1.5 coverslips (6311344) were obtained from Menzel Gläser. Microscope slides (09-3000) were obtained from Bio-Optica. Sail brand single concave glass slides (7103) were obtained from SmartLabs. Hellmanex III (Z805939-1EA) was obtained from Sigma-Aldrich. Double sided tape (665D) was obtained from Scotch. Twinsil speed 22 (1300-1002) was obtained from Picodent. Tween 20 (P9416-50ML), protocatechuate 3,4-dioxygenase from Pseudomonas sp. (PCD) (P8279-25UN), 3,4-dihydroxybenzoic acid (PCA) (506 37580-25G-F), (+−)-6-hydroxy-2,5,7,8-tetramethylchromane-2-carboxylic acid (Trolox) (238813-1G) and sodium hydroxide (30620-1KG-M) were obtained from Sigma-Aldrich. Methanol (c20846.326) was obtained from VWR. Glycerol (A0970-1000) was obtained from BioChemica. 90 nm diameter gold nanoparticles (G-90-100) were obtained from Cytodiagnostics. 40 nm dark-red beads (F8789) were obtained from Invitrogen. Low-glucose DMEM (11880028), FBS (10500064), 100x MEM NEAA (11140035) and trypsin-EDTA (15400054) were obtained from Gibco. Penicillin-streptomycin (P0781) was obtained from Sigma-Aldrich. L-glutamine (25030024) was obtained from Thermo Scientific. 20x SSC (AM9763) was obtained from Invitrogen. Ethylene carbonate (E26258-100G) and Triton X-100 (T8787-100ML) were obtained from Sigma Aldrich. ≥99.5% Formamide (47671) and Dextran sulfate (D8906) were obtained from Sigma Aldrich. 32% Paraformaldehyde (15714) was obtained from Electron Microscopy Sciences. 200 mM VRC (S1402S) was obtained from New England Biolabs.

Buffers and stock solutions

The buffers used for sample preparation and imaging are the following:

- **Buffer A**: 10 mM Tris pH 8.0, 100 mM NaCl. Stored at room temperature.
- **Buffer A+**: 10 mM Tris pH 8.0, 100 mM NaCl and 0.05% Tween-20. Stored at room temperature.
- **Buffer B+**: 5 mM Tris-HCl pH 8.0, 1 mM EDTA, 12.5 or 50 mM $MgCl_2$ and 0.05% Tween-20, optionally supplemented with 1× trolox, 1× PCA and 1× PCD. Stored at room temperature.
- **Cellular PAINT buffer**: 1xPBS + 500mM NaCl, supplemented with 1 x PCA, 1 x Trolox and 1 x PCD.
- **10x rectangle DNA origami folding buffer**: 50 mM Tris pH 8.0, 10 mM EDTA, 125 mM $MgCl_2$. Stored at room temperature.
- **10x BSA-biotin**: 10 mg BSA-biotin in 1 ml buffer A. Aliquots stored at -20°C.
- **20x Neutravidin**: 10 mg Neutravidin in 1 ml buffer A. Aliquots stored at -20°C.
- **40x PCA**: 154 mg PCA in 10 ml water and NaOH, pH adjusted to 9. Aliquots stored at -20°C.
- **100x PCD**: 9.3 mg PCD in 13.3 ml of buffer (100 mM Tris-HCl pH 8, 50 mM KCl, 1 mM EDTA, 50% glycerol). Aliquots stored at -20°C.
- **100x Trolox**: first, added 100 mg trolox to a mix of 430 µl 100% methanol and 345 µl 1 M NaOH, fully dissolved the trolox, then added 3.2 ml water. pH adjusted to 9. Aliquots stored at -20°C.

Conjugations

All DNA-PAINT imager strands were labelled in-house using either the maleimide + thiol or the NHS-ester + amine chemistry. For the maleimide + thiol chemistry, 20 nmol of thiol-modified oligonucleotide in 50 µl of 20 mM HEPES pH 7.3 + 100 mM NaCl were added to 50 µl of 2x TCEP (11.5 mg of TCEP hydrochloride in 20 ml of 20 mM HEPES pH 7.3 + 100 mM NaCl, pH adjusted to 7.3 with NaOH) and incubated for 1 hour at room temperature in the dark to reduce the disulfide bonds of the oligonucleotides. Then, 10 µl of 10 mM dye-maleimide in DMF were added to the reaction, the volume was brought to 200 µl with 20 mM HEPES pH 7.3 + 100 mM NaCl, and the reaction was incubated for 2 hours at room temperature in the dark. The reaction was then quenched by adding DTT to a final concentration of 50 mM. For the NHS ester + amine chemistry, 20 nmol of amine-modified oligos were subjected to one round of ethanol precipitation to remove any residual amine from the synthesis process by adding 0.1 volumes of 3 M NaCl and 2.5 volumes of cold absolute ethanol, incubating at -

20°C for 30 min, centrifuging at 21000 g at 4°C for 30 min, and resuspending the pellet in 190 µl of 100 mM sodium bicarbonate pH 8.3. This step was skipped in the case of the 7-nt speed-optimised imagers, as they are too short to be precipitated. Then, 10 µl of 10 mM dye-NHS ester in DMF were added to the reaction, and the reaction was incubated for 2 hours at room temperature in the dark. The reaction was quenched by adding Tris-HCl pH 8 to a final concentration of 50 mM. For both chemistries, the reaction pot after quenching was subjected to one preparative round of ethanol precipitation as just described before purifying via reverse-phase high-performance liquid chromatography on an UltiMate 3000 HPLC system equipped with a Phenomenex Clarity 5 µm oligo-RP column. Again, the preparative ethanol precipitation was skipped in the case of the speed-optimised imagers. The purified oligos were resuspended to 50 µM in 20 mM HEPES pH 7.3 + 100 mM NaCl and stored in low-binding Eppendorf tubes at -80°C. A list of all conjugations performed is provided in Supplementary Table 5.

DNA origami self-assembly and purification

The two dimensional rectangle origami is based on the design in (*43*). Folding of the DNA origami was accomplished in a 50 µl one-pot reaction consisting of 10 nM scaffold strand, 100 nM unmodified staple strands, excluding the ones substituted by a modified staple strand, 500 nM biotynilated staples and 500 nM modified staple strands (for a list of unmodified, biotynilated and handle-modified staple strands, see Supplementary Tables) in 1X folding. The reaction mix was then subjected to a thermal annealing ramp in a thermocycler, consisting in 5 min at 80°C, then cooling immediately to 60°C followed by cooling from 60°C to 4°C in steps of 1°C every 3 min 21 s. The sample was then held at 4°C until purification. In order to remove the excess staple strands and misfolded origamis, the origami was purified via three rounds of PEG precipitation, each consisting in adding the same volume of PEG buffer (1x TAE pH 8.0 + 15% PEG 8000, 500 mM NaCl, 12.5 mM $MgCl_2$), centrifuging at 14,000 g at 4°C for 30 min, removing the supernatant and resuspending in 1x folding buffer. The purified origamis were then stored in low-binding Eppendorf tubes at -20°C.

Bead sample preparation

Glass coverslips were first cleaned via three rounds of water-bath sonication for 10 min in a 2% solution of Hellmanex III. Between each round and at the end, the slides were copiously rinsed with MilliQ water, and finally dried with compressed nitrogen before storage. A flow chamber was formed by placing two double-sided Scotch strips parallel to each other on the microscope slide, and then sandwiching them between the slide and the coverslip. First, 20 µl of a 1:5 dilution of 90 nm gold nanoparticles in 1x PBS was incubated for 5 min in the flow chamber. After a 20 µl wash with 1x PBS, a 1:250 dilution of beads in 1x PBS (previously sonicated for 5 min) was incubated for 10 min. After a 20 µl wash with 1x PBS, the chamber was filled with more 1x PBS, and then sealed with epoxy glue.

DNA origami sample preparation and imaging

Two kinds of DNA origami samples were prepared, depending on whether the experiment included buffer exchange or not. In case no buffer exchange was needed (fluorogenic handles screening), a flow chamber was made from Scotch double-sided tape sandwiched between the microscope slide and the coverslip, as described previously (*48*). In case exchange was needed (everything else), an Ibidi well slide was used. The following protocol applies to the well slide, with changes for the flow chamber in parentheses. First, the cover glass was cleaned via two 800 µl washes with MilliQ water (Hellmanex cleaning as for bead samples). Then, 200 µl (20 µl) of a 1:4 dilution of 90 nm gold nanoparticles in 1x PBS was incubated for 5 minutes. After a 200 µl (20 µl) wash with 1xPBS and a 200 µl (20 µl) wash with buffer A+, 200 µl (20 µl) of BSA-biotin diluted to 1x in buffer A+ were incubated for 5 minutes. After a 200 µl (20 µl) wash with buffer A+, 200 µl (20 µl) of Neutravidin diluted to 1x in buffer A+ were incubated for 5 minutes. After a 200 µl (20 µl) wash with buffer A+ and a 200 µl (20 µl) wash with buffer B+, the DNA origami solution, diluted to approximately 100 pM in buffer B+, was incubated for 8 minutes. After a 200 µl (20 µl) wash with buffer B+, the imager solution in buffer B+ (imaging buffer) was added to the sample. The imaging buffer was supplemented with 1x PCD, 1x PCA and 1x Trolox. The flow chamber samples were at this point sealed with Twinsil and imaged, while well slides samples

were loaded on the microscope, closed with the chamber slide lid, and 15 minutes were waited to allow oxygen scavenging prior to starting to image. Exchange-PAINT was performed by carefully removing the lid to not disturb the actively-stabilized sample, washing with buffer B+ until single-molecule blinking stopped, and finally adding the next imaging buffer before placing back the lid. Details on imaging buffer and imaging conditions are provided in Supplementary Table 2.

Widefield DNA-PAINT processing

Movies obtained from widefield measurements (DNA origami and cell) were processed with Picasso (*37*). Drift correction of the residual long-term drift was performed via redundant cross-correlation. Alignment of Exchange PAINT rounds was performed via cross-correlation. Linking of the events was performed using a maximum distance of ~5 times the localisation precision (~20 nm) and zero dark frames allowed. The processing was also repeated varying these values and without major changes in results. For the mismatch multiplexing experiment, single sites of DNA origami rectangles were manually picked, with the only requirement of the grid being recognizable as of a given species. Since each origami carried twelve binding sites, this requirement was not met only in unfavourable scenarios (non-flatly bound origamis, misfolded origamis, and clusters with several origamis overlapping), making this manual labelling a reliable ground truth classification. If the grid could be recognised, every site present was picked, irrespective of number of events. For modular multiplexing experiments, the whole origami was picked as opposed to single sites. In addition to the previous requirements, the origami was picked only if it did not miss more than three sites, as this would not allow reliable fitting of the template in the subsequent analysis. After picking, custom Python scripts were used to analyze the data. For the mismatch multiplexing experiment, picked sites were filtered from sticking events (> 80% of the localisations happening in a segment <5% of the movie length), selected for repetitive binding (average frame value of the binding events between 10% and 90% of the movie length) and filtered for more than 15 binding events. Notably, all of these procedures are standard for DNA-PAINT, don't require manual picking (which can be substituted by a clustering algorithm) and can be met by adjusting the imaging time or strand concentration, to meet the required number of events. For the modular multiplexing, origamis were first noise-filtered via a light DBSCAN step with ε ~ 1.5σ and minimum number of events = 5 to remove isolated events, as well as missing sites. The origamis were then aligned with the template of the designed handle arrangement (as well as the mirror, to account for flipped origamis) using a nearest neighbor distance cost function. The result was visually inspected to remove misfit origamis. This provided the ground truth classification for subsequent analysis. Each binding event was then assigned to a handle via a Gaussian mixture model. Finally, the clusters were selected for more than 10 (6-color multiplexing) or 50 (9-color) total binding events. For both multiplexing strategies, the ground truth classification was used to retrieve the experimental proportion of binding to each imager (the probability vector $\mathbf{p} = (p_{ImA}, p_{ImB}, p_{ImC})$) of each handle species, as well as the average number of binding events for the modular multiplexing. The classification for the mismatch multiplexing experiment was performed, for each site H, via choosing the most likely handle species, H^*, given the formula

$$H^* = \underset{X \in T_{mis}}{\operatorname{argmax}}\, p_{(H=X)} = \sum_{ImY}^{(ImA,ImB,ImC)} p_{(ImY|X)}^{N_{ImY}}$$

Where $T_{mis} = \{\mathrm{HnA}, \mathrm{HnB}, \mathrm{HnC}, \mathrm{HnAB}, \mathrm{HnBC}, \mathrm{HnAC}\}$, the set of all handles in the 6-color mismatch multiplexing scheme, $p_{(H=X)}$ is the probability of site H being handle species X, $p_{(ImY|X)}$ the probability of binding of imager Y to handle species X, N_{ImY} the realized number of events from imager Y, and the sum being over all three imagers. For the modular multiplexing experiments, a different formula was used to harvest the information contained in the absolute number of binding events, assuming them to be Poisson distributed

$$H^* = \underset{X \in T_{mod}}{\operatorname{argmax}}\, p_{(H=X)} = \sum_{RY}^{(R1,R3,R5)} \left(N_{RY} \log \lambda_{X,RY} - \lambda_{X,RY}\right)$$

$T_{mod} = \{6\text{xR1}, 6\text{xR3}, 6\text{xR5}, 3\text{xR1} + 3\text{xR3}, 3\text{xR3} + 3\text{xR5}, 3\text{xR1} + 3\text{xR5}\}$ for the 6-color modular multiplexing experiment and $T_{mod} = \{5\text{xR1}, 7\text{xR3}, 5\text{xR5}, 1\text{xR3} + 3\text{xR1}, 1\text{xR1} + 3\text{xR3}, 1\text{xR5} + 3\text{xR3}, 1\text{xR3} + 3\text{xR5}, 1\text{xR1} + 3\text{xR5}, 1\text{xR5} + 3\text{xR1}\}$ for the 9-color modular multiplexing experiment and λ_Y is the average number of events of imager Y for handle species X.

RNA-FISH probe design

FISH-probe libraries were designed for the fully spliced mRNAs of MDN1, AHNAK1 and EPRS1 using OligoMiner (*55*). Homology regions were selected to be between 36 and 41 nt in length with a minimum GC content of 20%. The adjusted melting temperature in 50% formamide and 2xSSC was chosen to fall between 42 and 47 °C. Probes including 5 or more consecutive repeats of any given nucleotide were excluded. The generated probes were further filtered by oligoMiner's Linear Discrimination Analysis 42°C model with a threshold of 0.5, followed by a jellyfish 18bp k-mer filter with a k of 5. Probes were subsequently appended on their 5' end with their respective fluorogenic PAINT handle, using a 2-base linker and a stable bio-orthogonal smFISH imager handle (*29*) at their 3' end. Each mRNA probe set was split into three equal parts by the extension with different PAINT handles with the exact number of probes per mRNA and PAINT handle never falling below 15. Probe sequences for each probe set can be found in the Supplementary Tables.

Cell culture

HeLa Kyoto cells (female, HK WT: S. Narumiya (Kyoto University, Kyoto, Japan) were grown in 10 cm cell culture dishes (Falcon) in high-glucose DMEM containing 10% FBS, 100 U/ml penicillin-streptomycin and 1 mM L-glutamine. Cells were kept in a humidified incubator at 37°C and 5% CO_2. Passaging of cells was conducted every 2-3 days by detachment with 0.05% Trypsin-EDTA. U2OS cells were grown in DMEM without phenol red supplemented with 1x MEM NEAA, 10% FBS, 2 mM L-glutamine and 100 U/ml penicillin-streptomycin. Cells were kept in a humidified incubator at 37°C and 5% CO_2 and passaged every other day by detachment with 0.05% Trypsin-EDTA. Cells were routinely checked for mycoplasma contaminations.

Nanobody labelling and purification

Labelling of the anti-GFP nanobody with azide-modified DNA-PAINT handles via DBCO-maleimide crosslinker was performed as previously reported (*24*).

NUP96 imaging

U2OS NUP96-mEGFP (Cell Line Services no. 300174) were grown for two days on round coverslips to 50-70% confluency. Cells were then rinsed twice with 1xPBS, fixed with 2.4% PFA in 1xPBS for 30 min, rinsed thrice with 1xPBS, neutralized for 5 min with 100 mM NH_4Cl in 1xPBS, permeabilized for 5 min with 0.25% Triton X-100 in 1xPBS, and incubated for 1 hour in blocking buffer (1 mM EDTA, 3% BSA and 0.02% Tween-20 in 1xPBS). Cells were then incubated with 100 nM anti-GFP nanobody (labelled with a DNA-PAINT handle) in blocking buffer overnight at 4°C under slow shaking. Samples were washed for 5 min with 1xPBS to remove unbound nanobodies, incubated for 5 min with 90 nm gold nanoparticles diluted 1:1 in 1xPBS and rinsed thrice with 1xPBS. Cellular PAINT buffer with DNA-PAINT imager strand diluted to working concentration was deposited in the concave spot of a concave microscope slide, and the seeded coverslip was carefully flipped on top. The chamber was then sealed with Twinsil and imaging carried out similarly to (*56*).

Design of shielding strands for RNA-FISH

Shielding strands designed to block the DNA-PAINT handles during primary probe incubation but wash in subsequent steps were designed similarly to previous work (*45*). Each mismatch-based Combi-PAINT handle (including linker and padding oligonucleotides) was split in two sub-sequences of melting temperatures as close to each other as possible. The sequences (reverse-complementary to the handle sequence) were ordered and added to the primary incubation mixture as described below. The sequences can be found in the Supplementary Tables.

RNA-FISH

HeLa Kyoto cells were grown on glass bottom Ibidi-Luer µ-Slides overnight to a confluency of 60-70%. Cells were subsequently washed with 1xPBS for 2 min, followed by fixation with 4% PFA in 1xPBS for 10 min, permeabilization with 0.5% Triton in 1xPBS and a 5 min neutralization in 100 mM NH_4Cl in 1xPBS. A pre-denaturing step was carried out in which cells were treated with pre-heated 50% formamide/2xSSC and incubated at 60°C for 20 min followed by a 3 min incubation at 78°C. During the pre-denaturation step the hybridization buffer (50% formamide, 10% Dextran sulfate, 2 mM VRC in 2xSSC) was prepared. The pooled library of RNA-FISH-probes was added to the hybridization buffer at a concentration of 7 nM per probe. Shielding strands binding to the DNA-PAINT handles present in the used probe set were added at a concentration of 2 µM each and the mixture was incubated at RT for 20 min. Immediately after finishing the pre-denaturation step cells were incubated with the RNA-FISH-probe containing hybridization buffer over night at 42°C. The next day cells were washed four times with pre-heated 2% Tween in 2xSSC at 60°C before being cooled to RT with 2xSSC for 5 min. A secondary hybridization step for the smFISH imagers was carried out in 5% ethylene carbonate + 2% Tween in 2xSSC with a concentration of 20 nM per smFISH imager for 4 min. This was followed by a wash with 10% formamide + 2% Tween in 2xSSC for 1 min and a final transfer to 1xPBS. Samples were imaged the same day or kept at 4°C for up to two days.

Widefield RNA-FISH imaging

RNA-FISH samples were incubated with 90 nm gold fiducials (diluted 1:5 in 1xPBS) for 5 min and subsequently washed with 1xPBS three times. Samples were transferred to cellular PAINT buffer with the respective DNA-PAINT imager being added at its desired concentration. Acquisitions were carried out on an Elyra 7 microscope. A plane of interest was chosen by assessing the smFISH signal in the 488 nm channel followed by engaging the definite focus functionality to not lose the chosen focus during the acquisition. Movies were then recorded according to the information in Supplementary Table 2. Exchanges of the DNA-PAINT imagers were carried out by first washing with 1xPBS until no more signal could be detected in the respective imaging channel followed by flowing in a total of 500 µl of the new DNA-PAINT imager-containing cellular PAINT buffer. After ensuring the focused plane had not changed another round of imaging was conducted.

Widefield RNA-FISH DNA-PAINT processing

Movies obtained from widefield measurements (DNA origami and cell) were processed with Picasso (*37*). Drift correction of the residual long-term drift was performed via redundant cross-correlation and gold fiducials. Localization with a x/y precision above 20 nm were filtered. Alignment of Exchange PAINT rounds was performed via cross-correlation and alignment of gold fiducials. Linking of the events was performed using a maximum distance of ~3 times the localization precision (~15 nm) and zero dark frames allowed. The data was subsequently clustered using the DBSCAN implementation in Picasso Render with a minimum number of events of ~8 and a radius of ~40 nm. To ensure resulting clusters stem from repeated binding events a custom Python script was used to calculate the average frame value of all events per cluster and discard any that did not fall within a 20% range around the middle of the recorded movie. Following this clusters that overlapped with recorded smFISH signal of the imaged plane were picked and used for further analysis. All further analysis of the widefield data was performed using custom Python scripts. Multiple shape descriptors and parameters were calculated for each RNA species. End-to-end distances were calculated from the centroids of imaging rounds corresponding to the 5’ and 3’ end of each RNA. PCA was carried out and the major axis standard deviation, aspect ratio and major axis kurtosis of each particle were extracted. Significance testing was conducted using a pairwise Mann–Whitney U Test. For particles stemming from multiplexed widefield RNA imaging the ratio of events per exchange PAINT round was calculated and particles were plotted on ternary plots. Subsequent clustered using a DBSCAN implementation was finally used to classify the RNA species per recorded particle.

MINFLUX RNA-FISH imaging

RNA-FISH samples were incubated with 90 nm gold fiducial beads (diluted 1:3 in 1xPBS) for 5 min and subsequently washed with 1xPBS three times, then they were incubated with 40 nm dark red fiducial beads (diluted 1:10^6 in 1xPBS) for 10 min and subsequently washed with 1xPBS three times. Samples were transferred to cellular PAINT buffer with the respective DNA-PAINT imager being added at its desired concentration. A typical MINFLUX imaging started with widefield 488 illumination to detect and focus the smFISH signal, and picking of RNA particles for imaging. Widefield 640 nm illumination was then used to pick fluorescent beads for post-processing drift correction and imaging round alignment. Gold nanoparticles for infrared active stabilization were also selected at this point. The stage was then moved by a known amount to compensate for the discrepancy between the position of the 488 nm widefield focus and that of the 640 nm confocal detection and the axial active stabilization was engaged. A typical round of imaging lasted 45 minutes, during which the tip-tilt mirror used for scanning the sample alternated imaging between the RNP and the fluorescent beads, cycling through each every time 20 localizations were acquired (beads) or 5 minutes elapsed (RNP). Exchange rounds were carried out similarly to widefield experiments. The maximum laser power was approximately 40 µW at the sample plane.

Mixed-beams iterative MINFLUX imaging was performed similarly to previous works (*48*, *56*). The 3D MINFLUX strategy consisted of:

Iteration number	Beam arrangement	Relative power	Live estimator β_0, β_1	L_{xy} (nm)	L_z (nm)	Number of photons	Minimum time (ms)	Maximum time (ms)
0	7 G	0.15	1, 2	400	-	200	-	-
1	4 G	0.15	1, 1	300	-	200	-	-
2	5 V	0.25	0.8, 6	150	-	300	-	-
3	3 TH	1	0.4, 1.5	-	214	-	15	20
4	5 V + 3 TH	1	0.8, 22	150	214	30000	-	400

7 G: 6 Gaussians on a hexagon's vertices, plus one at the center; 4 G: 4 Gaussians on a square's vertices; 5 V: 4 vortices on a square's vertices, plus one at the center; 3 TH: 3 top hats on a line along the axial direction.

Iteration 3 was controlled by a proportional-integral feedback loop to make convergence in z more robust, using the live estimated molecule's position at each MINFLUX cycle as setpoint of the loop and acting on the top hat's interferometric deflection. This iteration did not stop upon collecting a certain number of photons, but instead stopped upon reaching a maximum allowed time or upon reaching the setpoint (with a tolerance of 5 nm) after a minimum time. The proportional-integral gains of the feedback loop were optimized on DNA origamis harboring a single, permanently-bound ATTO647N molecule(*48*) and additional free-floating ATTO643, at a concentration that simulated the nuclear Signal-to-Background Ratio (SBR), aiming for balanced settling time and overshooting. Iteration 4 was designed in terms of L and photon number to extract a large number of photons from the molecule, as this is optimal for localization precision at low signal-to-background ratios. Furthermore, isotropy of the localization precision in the 3 spatial directions was optimized by using 4 times more exposure time for the z (top hat) exposures as it is for the xy (vortex) exposures.

MINFLUX processing

The processing of the MINFLUX data acquired in this work was achieved via a Python implementation of previously used algorithms (*48*, *57*). Briefly, the photon trace of all MINFLUX last iterations was segmented into segments of a defined number of photons (typically 7500). These segments were then localised using an MLE estimator. Filtering of the localizations was done based on $p_{0\,xy}$ ($n_{0,vortex}/N_{vortex}$, the ratio of the photons from the central vortex in the last iteration and all vortex

exposures in the last iteration, typically chosen to be < 0.15), $p_{0\,z}$ ($n_{0,top\ hat}/N_{top\ hat}$, the ratio of the photons from the central top hat in the last iteration and all top hat exposures in the last iteration, tipically chosen to be < 0.25) and SBR (tipically chosen to be > 0.5) (Supplementary Fig. S10). Fluorescent bead localizations were then used to perform correction of residual drift and channel alignment: localizations coming from each bead at each timepoint of an imaging round were averaged to generate a high-precision localization. The trace formed by these localizations was then fit with a third-degree spline to interpolate the drift between timepoints. This continuous drift trajectory was then used to correct each MINFLUX localization for drift. The shift between rounds was similarly corrected by calculating the shift between the same bead in subsequent rounds of imaging and subtracting it to the entire round. Visualization of the data was done via Napari (*58*) after binning the 3D data (creating a 3D voxelated image) with a bin (voxel) size of 1.5-2 nm and applying a gaussian blurring of σ equal to the localization precision of the dataset (typically 2-2.5 nm). This localization precision was estimated in a similar way to the NeNA precision widely used in DNA-PAINT works, by retrieving the distribution of distance between consecutive localizations of the same binding event.

Fluorogenic mismatch-based Combi-PAINT strand design and screening

The design of the fluorogenic mismatch-based Combi-PAINT strands was done entirely in Python, following the steps in Fig. 1B. A mathematical model (depicted inExtended Data 1) was created to allow the design of imager-handle pairs of the desired length, number of mismatches (15 nt and 4 respectively, in agreement with results from (*40*)) when binding is desired (e.g., ImA to HnA), and as many mismatches as possible when it is not (to minimize crosstalk, e.g., ImA to HnB). The Python program assigned random bases to the nucleotide positions described in the model, and implemented a random shuffling of all bases apart from the first and last, as binding at the ends is desired anyway to make sure dye and quencher are truly far apart. The shuffling is necessary as the specific arrangement of matches and mismatches influences the strength and efficiency of binding, or in other words, the kinetics of binding. The program then runs the following checks using BioPython functions (*59*):

1. Pairwise local alignment of each undesired imager-handle pair (to avoid crosstalk)
2. Pairwise local alignment of each imager-imager pair (to avoid dimers)
3. Pairwise local alignment of each imager strands' start and end (to avoid hairpins)
4. Melting temperature (to match a desired range)

Pairwise local alignments scored matches as +1, mismatches as 0, and gap initiation and elongation as -1. Necessary scores to pass were <6, <7 and <4 for check 1, 2 and 3 respectively. The accepted melting temperature range at check 4 (calculated using DNA_NN3 nearest neighbor thermodynamics for 5 mM Tris, 50 mM Na^+ and 10 mM Mg^{2+}) was -45°C < < -25°C, but allowing up to 4 of the 12 desired pairwise bindings to lie outside this range. If these checks are passed, the imager-handle set is passed to NUPACK (*38*) to calculate all pairwise binding energies. The choice of the initial set was done by reviewing these energies for weakness (fast binding) and uniformity (similar binding time). The exhaustive search for optimal handles was again done entirely in Python using NUPACK. In this case, the imagers were left fixed, and all 4^{13} oligonucleotide handle sequences were generated (the first and last nucleotide were left fixed and matching). The following checks were ran:

1. Intramolecular binding energy (needs to be weaker than a threshold)
2. Binding energy with each imager (has to be outside certain ranges)

The intramolecular binding energy (calculated for 25°C, 50 mM Na^+ and 10 mM Mg^{2+} with model "dna04-nupack3" and ensemble "some-nupack3") was set to be higher than -0.8 kcal/mol. The binding energy range to exclude (calculated in the same conditions as the intramolecular binding) was < -10 kcal/mol and -8.5 < < -7 kcal/mol. The first range was too strong a binding (desired or not), while the second range a binding too weak if desired and too strong if undesired. If a handle passed these checks, depending on which binding energies to the imagers were suitable, the handle was classified as a

candidate for its handle type (e.g., if the binding energy to ImA and ImB were outside the excluded ranges, the handle is classified as a candidate HnAB). The handle sequences and binding energies were then filtered by species (the list of filters is provided in Supplementary Table 1) until ~100 sequences per species were left. For these sequences, the secondary structure of binding to their strands was predicted with NUPACK, and visually inspected for in-frame binding and strong binding at the extremities, with preference for weaker-binding handles. The top 10 handles of each handle species were given a 3', 2-nucleotide linker and a 5' 1-nucleotide overhang (*40*), designed to not modify the binding to the imagers or the intramolecular binding, and measured individually on DNA origamis to extract kinetics and evaluate image quality to select the best-performing handle of each species. Remarkably, all HnA, HnB and HnC candidates, and the majority of HnAB, HnBC and HnAC candidates yielded good-quality images, proving the effectiveness of the computational pipeline in finding functional handle sequences. HnABC was excluded for this work, since it would not be possible to distinguish from a cellular feature binding all imagers or the fluorophore indiscriminately. The code for initial imager/handle generation, as well as for exhaustive search and analysis is provided on GitHub.

Simulation of stoichiometries for modular multiplexing

Simulation of optimal stoichiometries for modular multiplexing was performed numerically in Python. Assuming three imager strand types A, B, C (in our case, R1, R3, R5), we modelled modular Combi-PAINT sets composed of handles each built with 3, 4, 5 or 6 possibly mixed concatenations of such types (3xA and 2xA+1xB could for example be part of the same set, but 5xA+1xB cannot). Only combinations that are radially symmetric on the ternary triangle were considered, as these better cover the ternary plot's space. Under these constraints, there are 6 Combi-PAINT handle sets for 3 modules, 12 for 4 modules, 35 for 5 and 272 for 6.

After defining a Combi-PAINT handle set, its performance is evaluated by calculating, for each of its handles, the classification error probability assuming N binding events. $N = n_A + n_B + n_C$, the sum of binding events from each imager strand, was sampled logarithmically. We also define $D_N = \{(n_A, n_B, n_C) \mid n_A + n_B + n_C = N\}$ as the set of all possible combinations of binding event numbers that sum to N. Then, the error probability for handle species X is defined as

$$P_{(\text{error},X)} = 1 - P_{(\text{not error},X)} = 1 - \sum_{\bar{n} \in D_{N,X}} P_{(\bar{n}|X)}$$
$$= 1 - \sum_{\bar{n} \in D_{N,X}} \frac{N!}{n_A!\, n_B!\, n_C!} {P_{(A|X)}}^{n_A} {P_{(B|X)}}^{n_B} {P_{(C|X)}}^{n_C}$$

Where $\bar{n}$ is a given realization of n_A, n_B, n_C events from the imagers, $D_{N,X} \subseteq D_N$ is the set of elements $\bar{n}$ for which handle species X is the most likely to have originated $\bar{n}$, in analogy to the classification problem in the Widefield DNA-PAINT processing section, and $P_{(A|X)}, P_{(B|X)}, P_{(C|X)}$ are the probabilities of binding of A, B, C assuming handle species X as the target. For each handle in a combination, the number of events necessary to obtain a reference error probability (1%) was determined by interpolation of the calculated N values, and the maximum value across handles of a given combination was retrieved as a metric of performance of the entire handle set.

Measurement of fluorogenicity factor

The fluorogenicity factor was measured on a LSM980 Axio Observer (Zeiss) inverted confocal laser scanning microscope. Samples of the fluorogenic strand alone (0.5 µM) or with an excess of the reverse complementary oligo (12.5 µM) in buffer B+PCA/PCD/trolox (if the dye was Cy3b, no additives for the far-red dyes) were made in separate flow chambers. The fluorogenic strand solution for each imager was made once and was used for both samples, to avoid pipetting error. The samples were measured at the same focus depth, several microns beyond the coverglass surface. All relevant parameters (confocal pinhole size, detector gain, detection spectral range, pixel dwell time) were kept constant between measurement, while the laser power was adjusted in order to not saturate the detector when

measuring the brighter sample with reverse complement, and to fully place the histogram of pixel values above the detector baseline when measuring the dimmer sample without reverse complement. The linearity of the laser power versus % value was ensured prior to the measurement. The average pixel value over the image was then calculated and normalized to the laser intensity used.

Funding

AP is the recipient of a DOC Fellowship of the Austrian Academy of Sciences at the Institute of Molecular Pathology. PW is the recipient of a Boehringer Ingelheim Fonds (BIF) PhD fellowship. Research in the laboratory of CP is supported by Boehringer-Ingelheim, the European Research Council under the Horizon 2020 research and innovation programme (949081) and by the Austrian Science Fund (FWF) doc.funds program DOC177-B (RNA@core: Molecular mechanisms in RNA biology). Research in the laboratory of FB was supported by Boehringer Ingelheim and the European Research Council (ERC) under the European Union's Horizon 2020 research and innovation program (853348). For the purpose of Open Access, the authors have applied a CC BY public copyright license to any Author Accepted Manuscript (AAM) version arising from this submission.

Author Contributions

AP and FB conceived the combinatorial multiplexing strategies. CP and FB conceived and identified the application of the super-resolved combinatorial multiplexing strategies for mRNA ultrastructure visualization. AP designed mismatching imaging/handle pairs, designed and folded DNA origami, optimized protocols, performed all DNA origami experiments and their data analysis. AP designed and built the custom widefield optical system. AG and FB built the custom MINFLUX system and programmed the hardware control for the widefield and MINFLUX systems. AP, AG, and FB programmed the MINFLUX processing and visualization software. PW designed RNA-FISH probes, optimized the FISH protocols, performed widefield RNA-FISH experiments and their processing. AP and PW performed MINFLUX RNA-FISH experiments and processing. AP, PW, CP and FB wrote the manuscript. FB and CP supervised the project. All authors proofread and commented on the manuscript.

Acknowledgements

We thank the Vienna Biocenter Core Facilities (VBCF) for their continuous support, in particular Mathias Madalinski for HPLC purifications, all members of the IMP/IMBA/GMI Mechanical Engineering Center and all members of the IMP/IMBA/GMI BioOptics Facility. We thank the entirety of the Balzarotti and Plaschka labs for discussion and feedback, with special regard to Karina Ayala and Alexander Philipps for help with cell lines. We thank Rupert Faraway and Daniel Zenklusen for helpful discussion regarding probe design and the choice of RNA targets. We thank Neos Cruz for sharing and discussing RNA-FISH protocols.

Competing Interests

FB holds patents on principles, embodiments and procedures of MINFLUX.

Data and Code availability

The raw data supporting the findings of this study are available from the corresponding author upon request. The code for initial imager/handle generation, as well as for exhaustive search and analysis is provided on GitHub at https://github.com/Balzarotti-Lab/fluorogenic_CombiPAINT_handle_generation.
Code for MINFLUX microscope control, MINFLUX data processing and visualization, Combi-PAINT simulations and Combi-PAINT DNA origami processing can be provided upon request.

Extended Data

	1	2	3	4	5	6	7	8	9	10	11	12	13	14	15
ImA	X_{1ABC}	X_{2A}	X_{3A}	X_{4A}	X_{5A}	X_{6AC}	X_{7AC}	X_{8AC}	X_{9AC}	X_{10AB}	X_{11AB}	X_{12AB}	X_{13AB}	X_{14ABC}	X_{15ABC}
ImB	X_{1ABC}	X_{2BC}	X_{3BC}	X_{4BC}	X_{5BC}	X_{6B}	X_{7B}	X_{8B}	X_{9B}	X_{10AB}	X_{11AB}	X_{12AB}	X_{13AB}	X_{14ABC}	X_{15ABC}
ImC	X_{1ABC}	X_{2BC}	X_{3BC}	X_{4BC}	X_{5BC}	X_{6AC}	X_{7AC}	X_{8AC}	X_{9AC}	X_{10C}	X_{11C}	X_{12C}	X_{13C}	X_{14ABC}	X_{15ABC}
HnA	Y_{1ABC}	Y_{2A}	Y_{3A}	Y_{4A}	Y_{5A}	Y_{6AC}	Y_{7AC}	Y_{8AC}	Y_{9M}	Y_{10AB}	Y_{11AB}	Y_{12M}	Y_{13M}	Y_{14M}	Y_{15ABC}
HnB	Y_{1ABC}	Y_{2BC}	Y_{3BC}	Y_{4M}	Y_{5M}	Y_{6B}	Y_{7B}	Y_{8B}	Y_{9B}	Y_{10AB}	Y_{11AB}	Y_{12AB}	Y_{13M}	Y_{14M}	Y_{15ABC}
HnC	Y_{1ABC}	Y_{2BC}	Y_{3BC}	Y_{4BC}	Y_{5M}	Y_{6AC}	Y_{7AC}	Y_{8M}	Y_{9M}	Y_{10C}	Y_{11C}	Y_{12C}	Y_{13C}	Y_{14M}	Y_{15ABC}
HnAB	Y_{1ABC}	Y_{2A}	Y_{3A}	Y_{4A}	Y_{5A}	Y_{6B}	Y_{7B}	Y_{8B}	Y_{9B}	Y_{10AB}	Y_{11AB}	Y_{12AB}	Y_{13AB}	Y_{14ABC}	Y_{15ABC}
HnBC	Y_{1ABC}	Y_{2BC}	Y_{3BC}	Y_{4BC}	Y_{5BC}	Y_{6B}	Y_{7B}	Y_{8B}	Y_{9B}	Y_{10C}	Y_{11C}	Y_{12C}	Y_{13C}	Y_{14ABC}	Y_{15ABC}
HnAC	Y_{1ABC}	Y_{2A}	Y_{3A}	Y_{4A}	Y_{5A}	Y_{6AC}	Y_{7AC}	Y_{8AC}	Y_{9AC}	Y_{10C}	Y_{11C}	Y_{12C}	Y_{13C}	Y_{14ABC}	Y_{15ABC}
HnABC	Y_{1ABC}	Y_{2BC}	Y_{3BC}	Y_{4BC}	Y_{5BC}	Y_{6AC}	Y_{7AC}	Y_{8AC}	Y_{9AC}	Y_{10AB}	Y_{11AB}	Y_{12AB}	Y_{13AB}	Y_{14ABC}	Y_{15ABC}

Extended Data 1: Combinatorial model for mismatching handle-imager generation.

Combinatorial model to achieve combinations via mismatches. Each symbol in the table is a DNA nucleotide that obeys the following rules: 1) $X_{i\alpha} = \mathrm{complement}(Y_{i\alpha})$, where complement is the Watson-Crick complement; 2) $X_{i\alpha} \neq X_{i\beta}$; 3) $X_{i\alpha}$ and $X_{j\alpha}$ may or may not be the same nucleotide; 4) $Y_{iM} \neq Y_{i\alpha}$ and $Y_{iM} \neq Y_{i\beta}$, so Y_{iM} is a mismatch with all imagers. The model allows to have 4 mismatches between each binding imager-handle pair, and the maximum possible number of mismatches (>9) between non-binding imager-handle pairs. Handle sequences need to be reversed to obtain the 5'→3' handle sequence. The table columns are ordered to show the symmetries of the model, but should be shuffled to explore different mismatch positions along the sequence space, which influence binding kinetics.

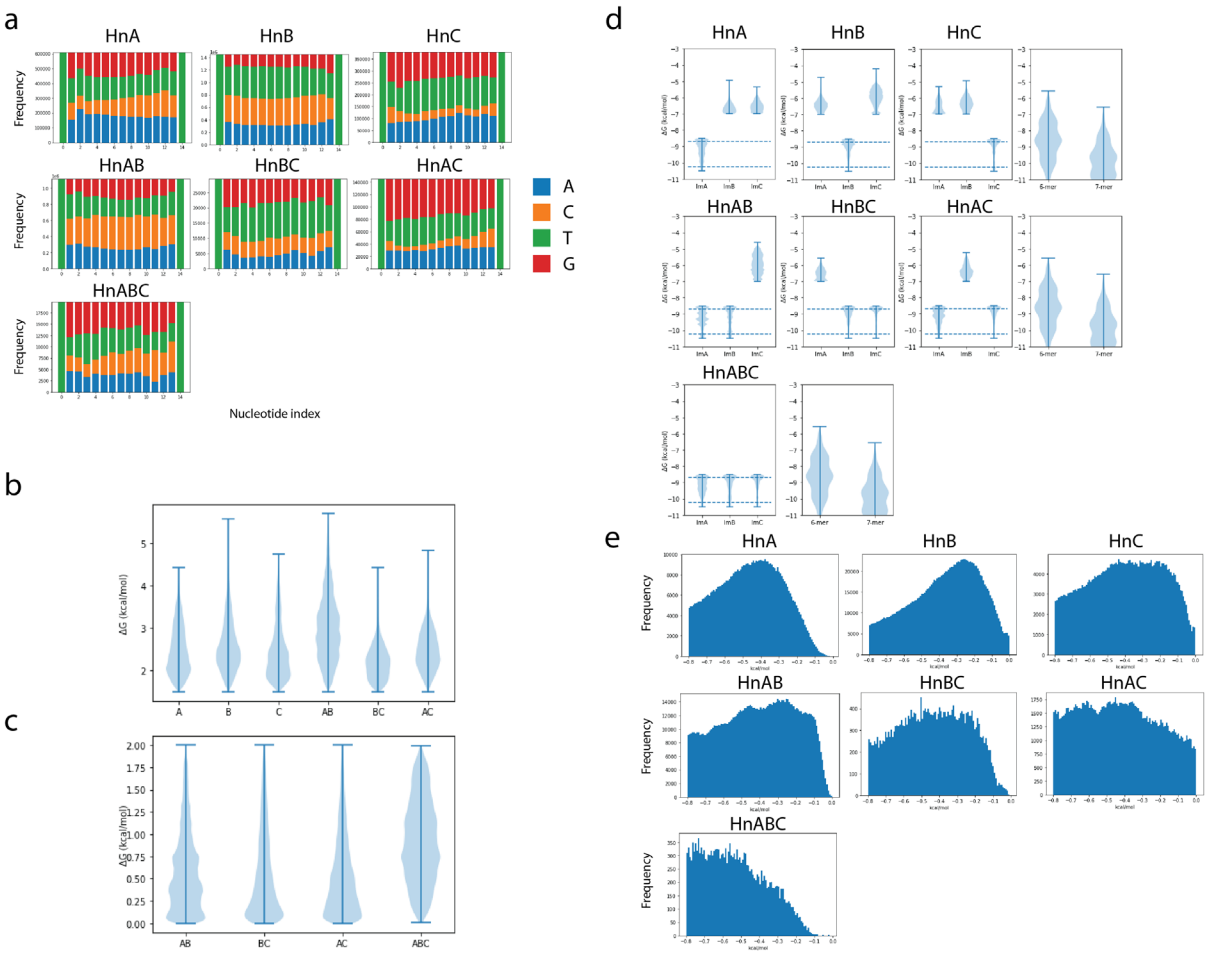

Extended Data 2: Parameters of mismatching handles pre-filtering.

Relevant parameters of mismatching handles coming from the exhaustive search before filtering. **a**, Base preference for each handle species by nucleotide index. From top to bottom: A (blue), C (orange), T (green), G (red). **b**, Wanted-unwanted binding energy gap (difference between the highest energy (weakest binding) among desired bindings and the lowest energy (strongest binding) among undesired binding). **c**, Binding energy discrepancy (maximum difference between the highest and lowest energies of the desired bindings). **d**, Energy of binding between the handles and the imagers. On the right is shown the violin plot of the energy of binding of all possible 6- and 7-mers to their reverse complements in the same conditions as for the mismatching strand, and the dashed lines correspond to their averages. This is to give a comparison between the binding energies of the mismatching sequences and the ones of speed-optimized DNA-PAINT. **e**, Energy of self-interaction.

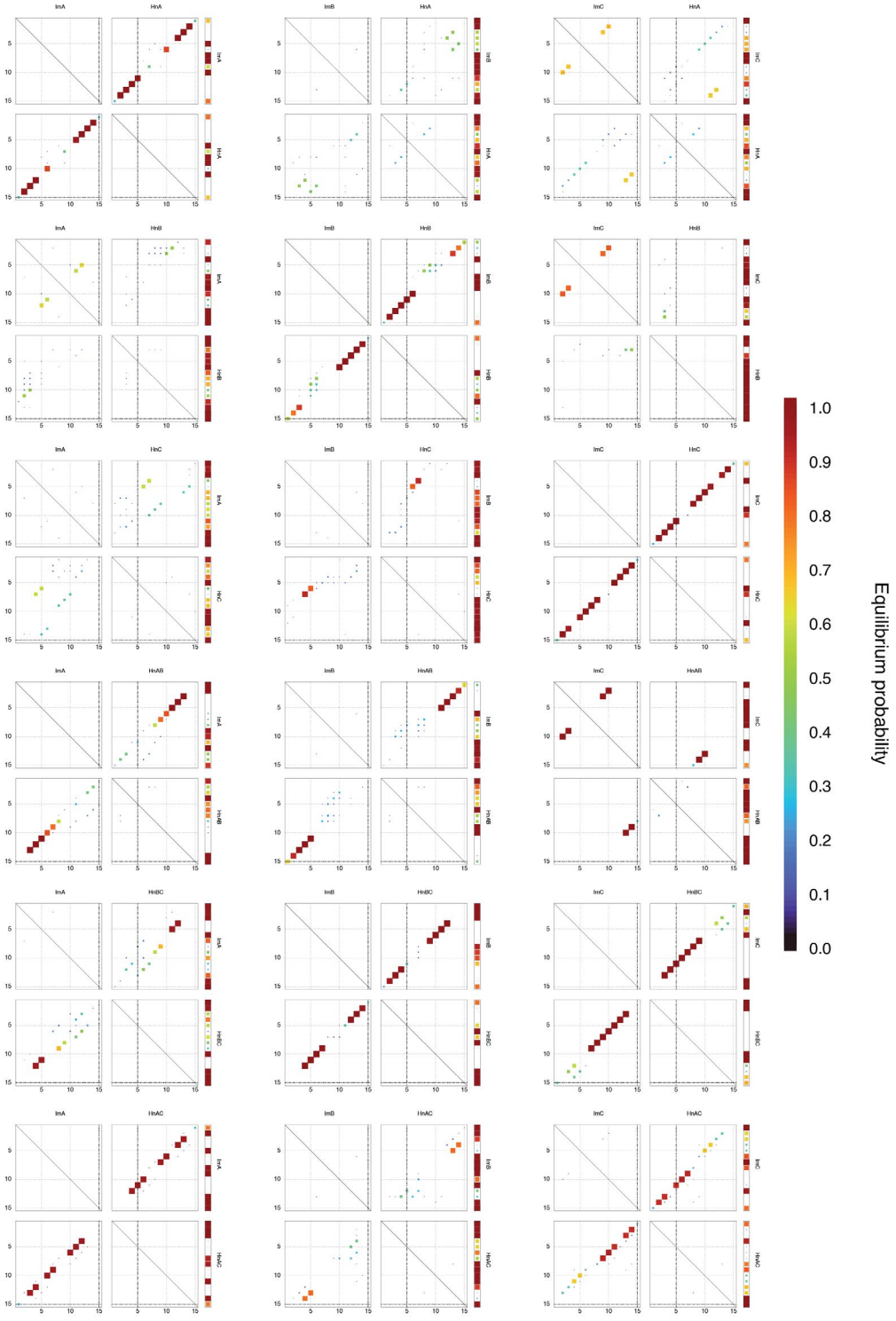

Extended Data 3: NUPACK predictions of the selected mismatching strands.

Pair probabilities of imager strands and handles, as predicted by NUPACK. Predictions were calculated at 0°C, 0.5 M NaCl.

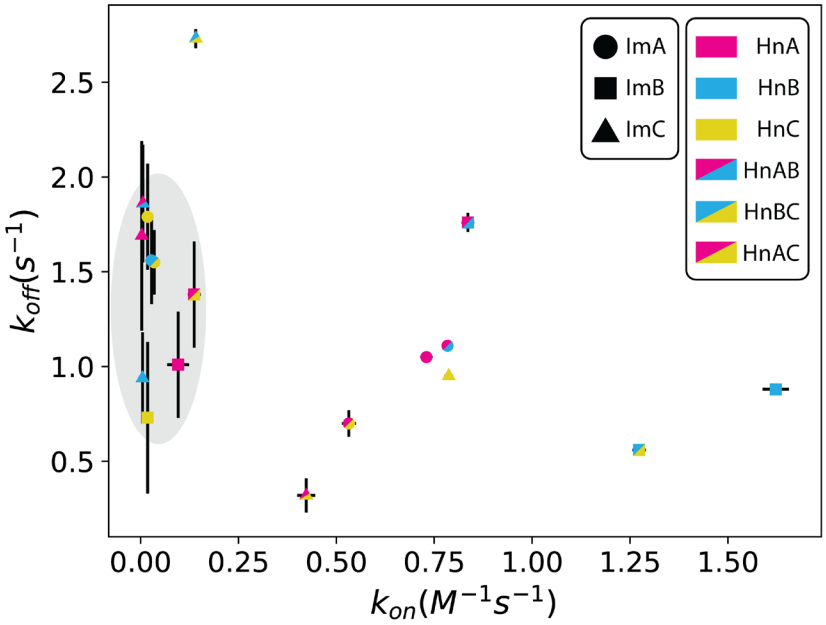

Extended Data 4: Kinetics of mismatching handles.

Average kinetics ± s.e.m of the handles-imager pairs. S.e.m. bars might be hidden by the marker. Undesired bindings are highlighted by the gray ellipse.

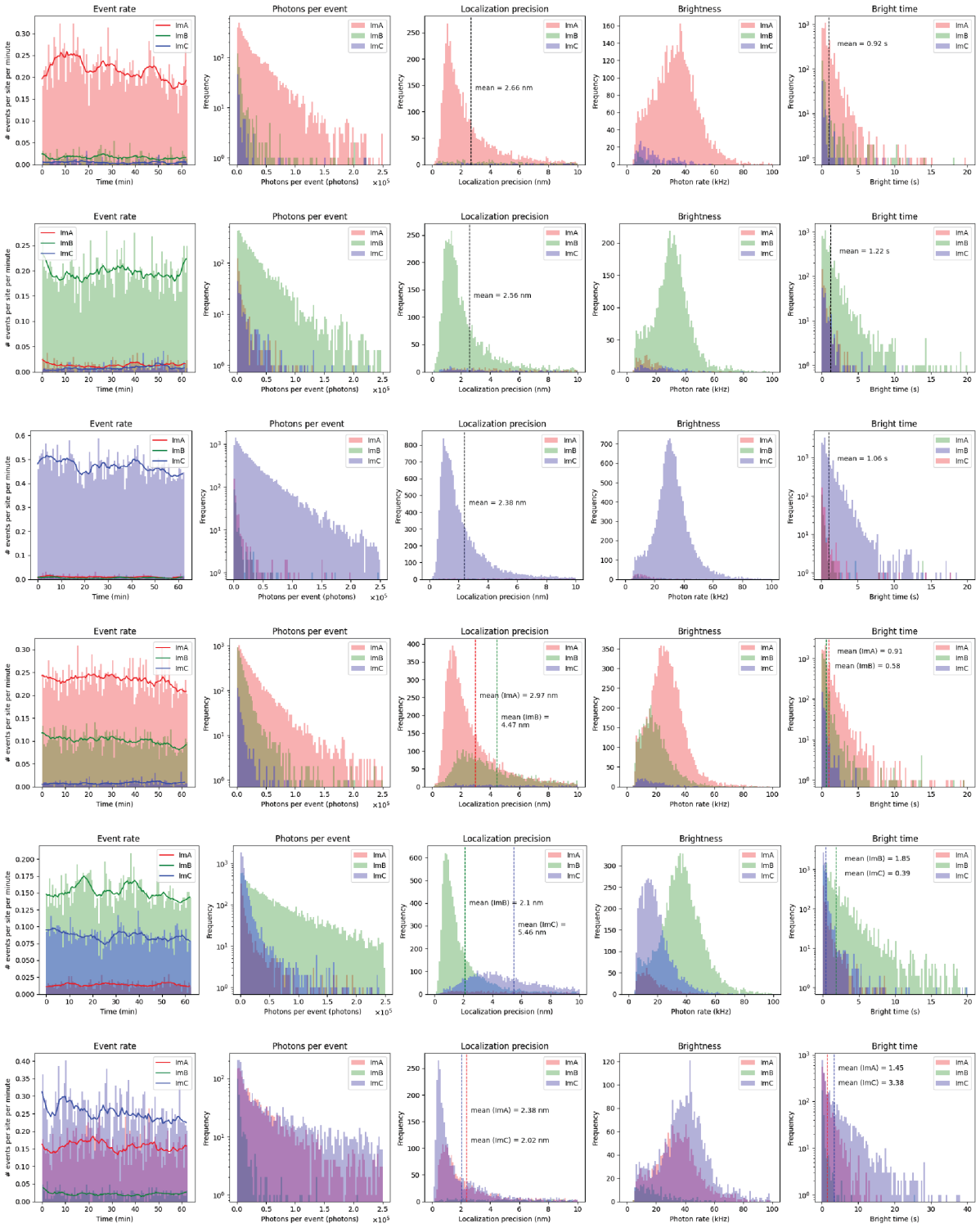

Extended Data 5: Photophysics of fluorogenic imagers/handles family.

Imaging statistics for the chosen mismatching handles.

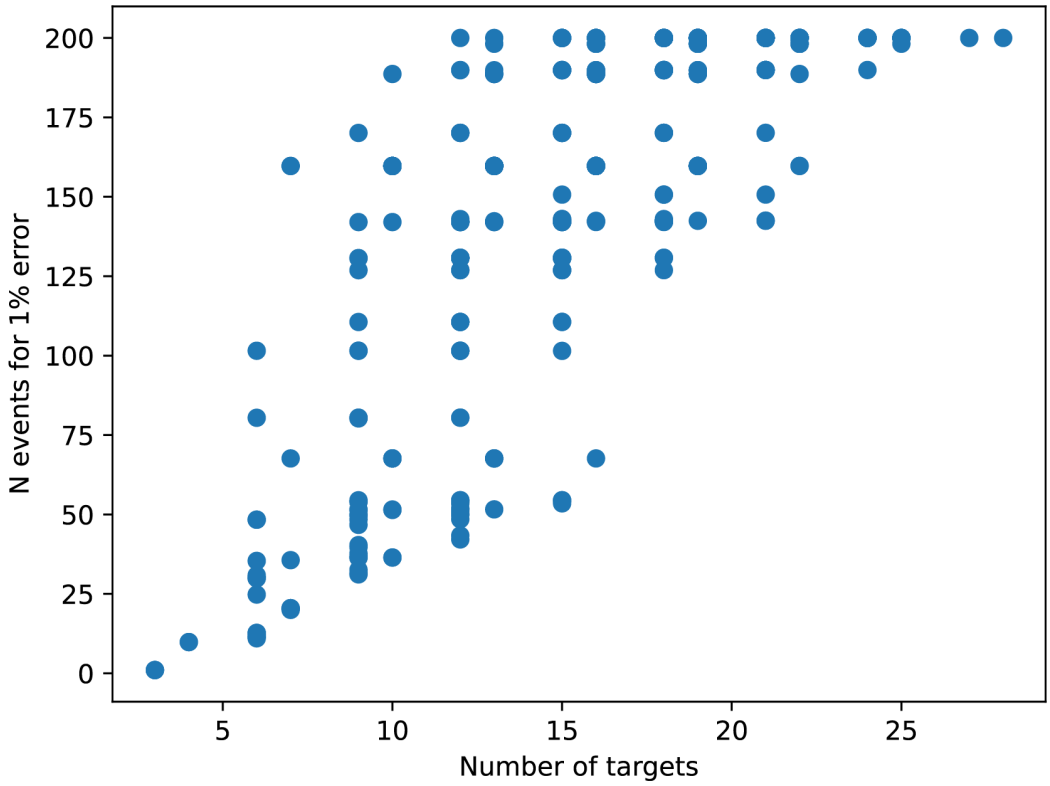

Extended Data 6: Efficiency of modular multiplexing stoichiometries.

Scatter plot of the efficiency (as number of events required to reach a 1% error) across different number of targets and different stoichiometries of binding sites on the modular multiplexing binding site. Even for comparatively low number of targets (e.g., 6), a large range of efficiencies can be achieved, making the choice of stoichiometries a non-trivial and important problem. The required number of events was clipped at 200 if higher.

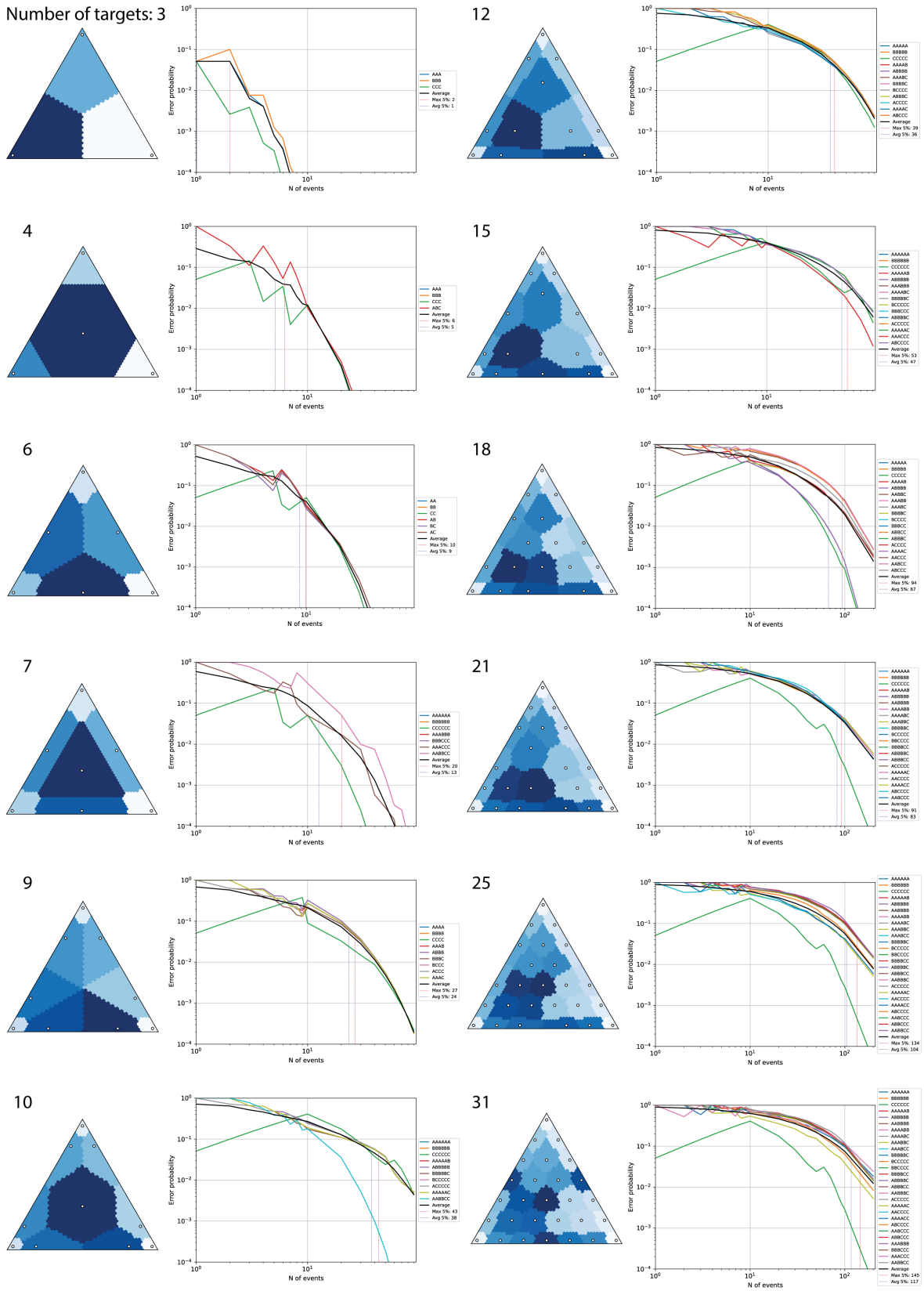

Extended Data 7: Optimal module stoichiometries and error probabilities.

Optimal stoichiometries and associated error probabilities versus number of events, by number of targets. All combinations of 3, 4, 5 and 6 modules were simulated, and the most efficient

stoichiometry to distinguish a number of targets from 3 to 28 was chosen based on the number of events required for the error probability to cross a 5% threshold. The ternary plots on the left side show the strategy, with the maximum likelihood regions of each species in different colors. The plots on the right side show the error probability versus the number of events. These simulations were done assuming a ~5% off-target binding, which is in line with the experimental ones (1% < < 10%, for different handles across the modular and mismatching strategies).

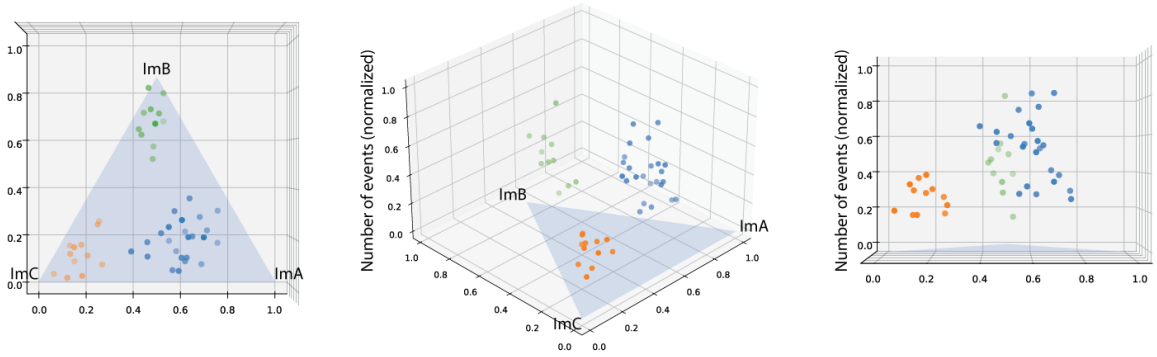

Extended Data 8: RNA-FISH Combi-PAINT with event number information.

RNA-FISH Combi-PAINT blind classification can be improved further by including absolute number of events information, due to the mRNAs being labelled with different number of probes due to length and/or sequence-specificity constraints. The total number of events from all rounds was normalized to allow comparison with the proportion of binding to each imager strand.

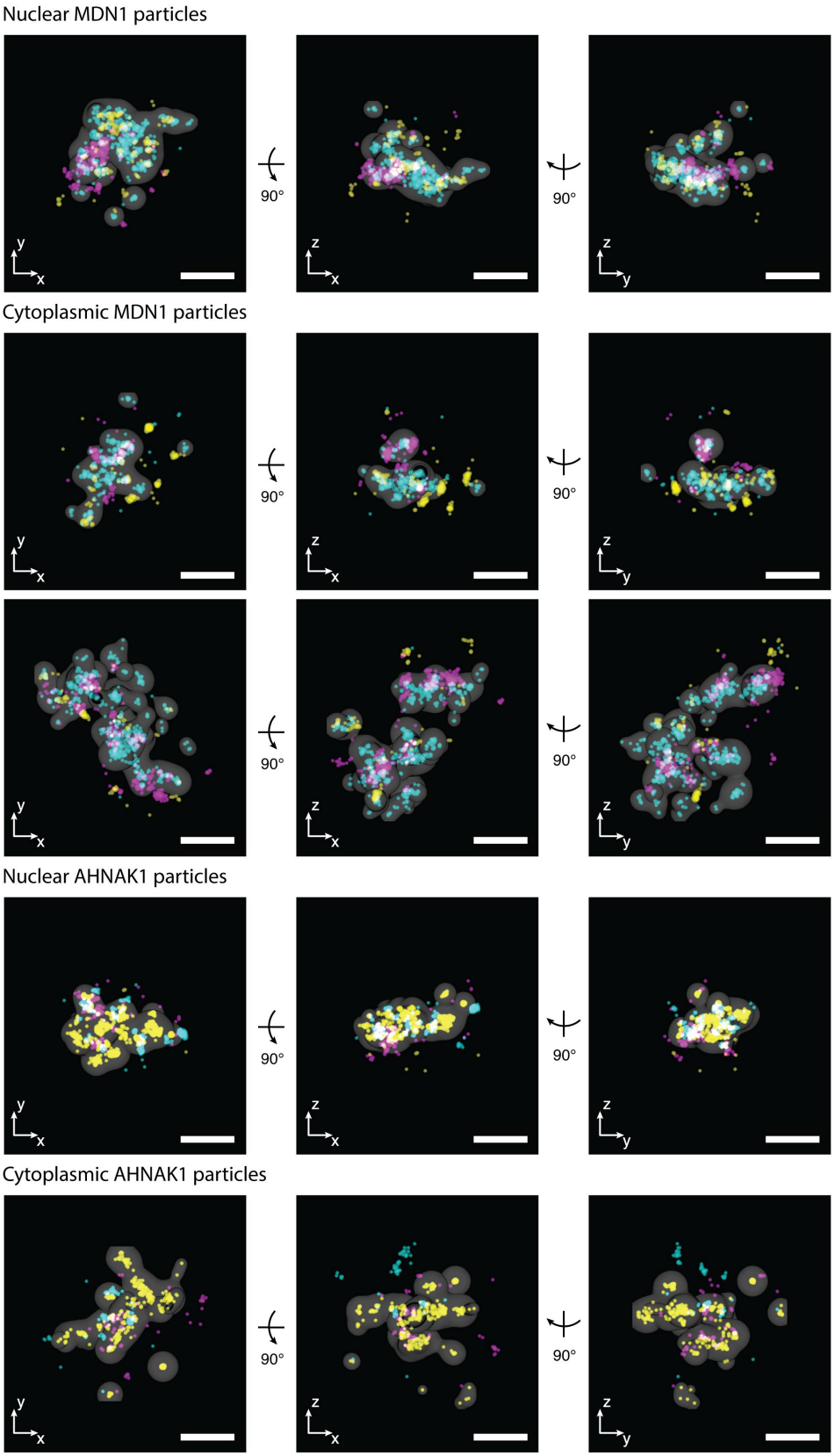

Extended Data 9: Additional 3D MINFLUX MDN1 and AHNAK1 mRNPs.
Additional MDN1 and AHNAK1 3D MINFLUX mRNPs, marked as nuclear or cytoplasmic based on their localization.

References

1. G. Singh, G. Pratt, G. W. Yeo, M. J. Moore, The Clothes Make the mRNA: Past and Present Trends in mRNP Fashion. *Annu. Rev. Biochem.* **84**, 325–354 (2015).
2. A. Khong, R. Parker, The landscape of eukaryotic mRNPs. *RNA* **26**, 229–239 (2020).
3. Q. Vicens, J. S. Kieft, Thoughts on how to think (and talk) about RNA structure. *Proc. Natl. Acad. Sci. U. S. A.* **119**, e2112677119 (2022).
4. B. Pacheco-Fiallos, M. K. Vorländer, D. Riabov-Bassat, L. Fin, F. J. O'Reilly, F. I. Ayala, U. Schellhaas, J. Rappsilber, C. Plaschka, mRNA recognition and packaging by the human transcription–export complex. *Nature* **616**, 828–835 (2023).
5. R. Faraway, D. Zenklusen, C. Plaschka, Mechanisms of Messenger RNA Packaging and Export. *Annu. Rev. Cell Dev. Biol.* **41**, 479–504 (2025).
6. J. B. Lucks, S. A. Mortimer, C. Trapnell, S. Luo, S. Aviran, G. P. Schroth, L. Pachter, J. A. Doudna, A. P. Arkin, Multiplexed RNA structure characterization with selective 2′-hydroxyl acylation analyzed by primer extension sequencing (SHAPE-Seq). *Proc. Natl. Acad. Sci.* **108**, 11063–11068 (2011).
7. T. Wu, A. Y. Cheng, Y. Zhang, J. Xu, J. Wu, L. Wen, X. Li, B. Liu, X. Dou, P. Wang, L. Zhang, J. Fei, J. Li, Z. Ouyang, C. He, KARR-seq reveals cellular higher-order RNA structures and RNA–RNA interactions. *Nat. Biotechnol.* **42**, 1909–1920 (2024).
8. J. Wang, Y. Zhang, T. Zhang, W. T. Tan, F. Lambert, J. Darmawan, R. Huber, Y. Wan, RNA structure profiling at single-cell resolution reveals new determinants of cell identity. *Nat. Methods* **21**, 411–422 (2024).
9. M. F. S. Degenhardt, H. F. Degenhardt, Y. R. Bhandari, Y.-T. Lee, J. Ding, P. Yu, W. F. Heinz, J. R. Stagno, C. D. Schwieters, N. R. Watts, P. T. Wingfield, A. Rein, J. Zhang, Y.-X. Wang, Determining structures of RNA conformers using AFM and deep neural networks. *Nature* **637**, 1234–1243 (2025).
10. U. Skoglund, K. Andersson, B. Strandberg, B. Daneholt, Three-dimensional structure of a specific pre-messenger RNP particle established by electron microscope tomography. *Nature* **319**, 560–564 (1986).
11. A. K. Christensen, L. E. Kahn, C. M. Bourne, Circular polysomes predominate on the rough endoplasmic reticulum of somatotropes and mammotropes in the rat anterior pituitary. *Am. J. Anat.* **178**, 1–10 (1987).
12. R. H. Singer, D. C. Ward, Actin gene expression visualized in chicken muscle tissue culture by using in situ hybridization with a biotinated nucleotide analog. *Proc. Natl. Acad. Sci.* **79**, 7331–7335 (1982).
13. A. M. Femino, F. S. Fay, K. Fogarty, R. H. Singer, Visualization of Single RNA Transcripts in Situ. *Science* **280**, 585–590 (1998).
14. S. Adivarahan, N. Livingston, B. Nicholson, S. Rahman, B. Wu, O. S. Rissland, D. Zenklusen, Spatial Organization of Single mRNPs at Different Stages of the Gene Expression Pathway. *Mol. Cell* **72**, 727-738.e5 (2018).
15. S. W. Hell, J. Wichmann, Breaking the diffraction resolution limit by stimulated emission: stimulated-emission-depletion fluorescence microscopy. *Opt. Lett.* **19**, 780 (1994).
16. E. Betzig, Proposed method for molecular optical imaging. *Opt. Lett.* **20**, 237 (1995).
17. S. J. Sahl, S. W. Hell, S. Jakobs, Fluorescence nanoscopy in cell biology. *Nat. Publ. Group*, doi: 10.1038/nrm.2017.71 (2017).
18. E. Betzig, G. H. Patterson, R. Sougrat, O. W. Lindwasser, S. Olenych, J. S. Bonifacino, M. W. Davidson, J. Lippincott-Schwartz, H. F. Hess, Imaging intracellular fluorescent proteins at nanometer resolution. *Science* **313** (2006).
19. S. T. Hess, T. P. K. Girirajan, M. D. Mason, Ultra-high resolution imaging by fluorescence photoactivation localization microscopy. *Biophys. J.* **91** (2006).
20. M. J. Rust, M. Bates, X. Zhuang, Sub-diffraction-limit imaging by stochastic optical reconstruction microscopy (STORM). *Nat. Methods* **3** (2006).
21. R. Jungmann, C. Steinhauer, M. Scheible, A. Kuzyk, P. Tinnefeld, F. C. Simmel, Single-Molecule Kinetics and Super-Resolution Microscopy by Fluorescence Imaging of Transient Binding on DNA Origami. *Nano Lett.* **10**, 4756–4761 (2010).
22. R. Jungmann, M. S. Avendaño, J. B. Woehrstein, M. Dai, W. M. Shih, P. Yin, Multiplexed 3D cellular super-resolution imaging with DNA-PAINT and Exchange-PAINT. *Nat. Methods* **11**, 313–318 (2014).
23. F. Schueder, F. Rivera-Molina, M. Su, Z. Marin, P. Kidd, J. E. Rothman, D. Toomre, J. Bewersdorf, Unraveling cellular complexity with transient adapters in highly multiplexed super-resolution imaging. *Cell* **187**, 1769-1784.e18 (2024).
24. E. M. Unterauer, S. S. Boushehri, K. Jevdokimenko, L. A. Masullo, M. Ganji, S. Sograte-Idrissi, R. Kowalewski, S. Strauss, S. C. M. Reinhardt, A. Perovic, C. Marr, F. Opazo, E. F. Fornasiero, R. Jungmann, Spatial proteomics in neurons at single-protein resolution. *Cell* **187**, 1785-1800.e16 (2024).

25. R. Jungmann, M. S. Avendaño, M. Dai, J. B. Woehrstein, S. S. Agasti, Z. Feiger, A. Rodal, P. Yin, Quantitative super-resolution imaging with qPAINT. *Nat. Methods* **13**, 439–442 (2016).
26. S. C. M. Reinhardt, L. A. Masullo, I. Baudrexel, P. R. Steen, R. Kowalewski, A. S. Eklund, S. Strauss, E. M. Unterauer, T. Schlichthaerle, M. T. Strauss, C. Klein, R. Jungmann, Ångström-resolution fluorescence microscopy. *Nature* **617**, 711–716 (2023).
27. J. Dekker, F. Alber, S. Aufmkolk, B. J. Beliveau, B. G. Bruneau, A. S. Belmont, L. Bintu, A. Boettiger, R. Calandrelli, C. M. Disteche, D. M. Gilbert, T. Gregor, A. S. Hansen, B. Huang, D. Huangfu, R. Kalhor, C. S. Leslie, W. Li, Y. Li, J. Ma, W. S. Noble, P. J. Park, J. E. Phillips-Cremins, K. S. Pollard, S. M. Rafelski, B. Ren, Y. Ruan, Y. Shav-Tal, Y. Shen, J. Shendure, X. Shu, C. Strambio-De-Castillia, A. Vertii, H. Zhang, S. Zhong, Spatial and temporal organization of the genome: Current state and future aims of the 4D nucleome project. *Mol. Cell* **83**, 2624–2640 (2023).
28. L. J. Mateo, S. E. Murphy, A. Hafner, I. S. Cinquini, C. A. Walker, A. N. Boettiger, Visualizing DNA folding and RNA in embryos at single-cell resolution. *Nature* **568**, 49–54 (2019).
29. K. S. Beckwith, A. Brunner, N. R. Morero, R. Jungmann, J. Ellenberg, Nanoscale DNA tracing reveals the self-organization mechanism of mitotic chromosomes. *Cell* **188**, 2656-2669.e17 (2025).
30. B. J. Beliveau, A. N. Boettiger, M. S. Avendaño, R. Jungmann, R. B. McCole, E. F. Joyce, C. Kim-Kiselak, F. Bantignies, C. Y. Fonseka, J. Erceg, M. A. Hannan, H. G. Hoang, D. Colognori, J. T. Lee, W. M. Shih, P. Yin, X. Zhuang, C. Wu, Single-molecule super-resolution imaging of chromosomes and in situ haplotype visualization using Oligopaint FISH probes. *Nat. Commun.* **6**, 7147 (2015).
31. H. M. Sasaki, J. Y. Kishi, C. Wu, B. J. Beliveau, P. Yin, Quantitative multiplexed imaging of chromatin ultrastructure with Decode-PAINT. bioRxiv [Preprint] (2022). https://doi.org/10.1101/2022.08.01.502089.
32. A. Raulf, C. K. Spahn, P. J. M. Zessin, K. Finan, S. Bernhardt, A. Heckel, M. Heilemann, Click chemistry facilitates direct labelling and super-resolution imaging of nucleic acids and proteins. *RSC Adv.* **4**, 30462–30466 (2014).
33. F. Chen, P. W. Tillberg, E. S. Boyden, Expansion microscopy. *Science* **347**, 543–548 (2015).
34. F. Chen, A. T. Wassie, A. J. Cote, A. Sinha, S. Alon, S. Asano, E. R. Daugharthy, J.-B. Chang, A. Marblestone, G. M. Church, A. Raj, E. S. Boyden, Nanoscale imaging of RNA with expansion microscopy. *Nat. Methods* **13**, 679–684 (2016).
35. F. Schueder, J. Lara-Gutiérrez, B. J. Beliveau, S. K. Saka, H. M. Sasaki, J. B. Woehrstein, M. T. Strauss, H. Grabmayr, P. Yin, R. Jungmann, Multiplexed 3D super-resolution imaging of whole cells using spinning disk confocal microscopy and DNA-PAINT. *Nat. Commun.* **8**, 2090 (2017).
36. K. Huang, F. Demirci, M. Batish, W. Treible, B. C. Meyers, J. L. Caplan, Quantitative, super-resolution localization of small RNAs with sRNA-PAINT. *Nucleic Acids Res.* **48**, e96 (2020).
37. J. Schnitzbauer, M. T. Strauss, T. Schlichthaerle, F. Schueder, R. Jungmann, Super-resolution microscopy with DNA-PAINT. *Nat. Protoc.* **12**, 1198–1228 (2017).
38. M. E. Fornace, N. J. Porubsky, N. A. Pierce, A Unified Dynamic Programming Framework for the Analysis of Interacting Nucleic Acid Strands: Enhanced Models, Scalability, and Speed. *ACS Synth. Biol.* **9**, 2665–2678 (2020).
39. J. J. Schmied, M. Raab, C. Forthmann, E. Pibiri, B. Wünsch, T. Dammeyer, P. Tinnefeld, DNA origami–based standards for quantitative fluorescence microscopy. *Nat. Protoc.* **9**, 1367–1391 (2014).
40. K. K. H. Chung, Z. Zhang, P. Kidd, Y. Zhang, N. D. Williams, B. Rollins, Y. Yang, C. Lin, D. Baddeley, J. Bewersdorf, Fluorogenic DNA-PAINT for faster, low-background super-resolution imaging. *Nat. Methods*, 1–6 (2022).
41. J. V. Thevathasan, M. Kahnwald, K. Cieśliński, P. Hoess, S. K. Peneti, M. Reitberger, D. Heid, K. C. Kasuba, S. J. Hoerner, Y. Li, Y.-L. Wu, M. Mund, U. Matti, P. M. Pereira, R. Henriques, B. Nijmeijer, M. Kueblbeck, V. J. Sabinina, J. Ellenberg, J. Ries, Nuclear pores as versatile reference standards for quantitative superresolution microscopy. *Nat. Methods* **16**, 1045–1053 (2019).
42. S. Strauss, R. Jungmann, Up to 100-fold speed-up and multiplexing in optimized DNA-PAINT. *Nat. Methods* **17**, 789–791 (2020).
43. F. Schueder, J. Stein, F. Stehr, A. Auer, B. Sperl, M. T. Strauss, P. Schwille, R. Jungmann, An order of magnitude faster DNA-PAINT imaging by optimized sequence design and buffer conditions. *Nat. Methods* **16**, 1101–1104 (2019).
44. B. J. Beliveau, E. F. Joyce, N. Apostolopoulos, F. Yilmaz, C. Y. Fonseka, R. B. McCole, Y. Chang, J. B. Li, T. N. Senaratne, B. R. Williams, J.-M. Rouillard, C. Wu, Versatile design and synthesis platform for visualizing genomes with Oligopaint FISH probes. *Proc. Natl. Acad. Sci.* **109**, 21301–21306 (2012).

45. E. Lučinskaitė, A. F. E. Bokhobza, A. Stannard, A. Meletiou, C. Estell, S. West, L. D. Michele, C. Soeller, A. H. Clowsley, Reduced Non-Specific Binding of Super-Resolution DNA-PAINT Markers by Shielded DNA-PAINT Labeling Protocols. *Small* **20**, 2405032 (2024).
46. U. Endesfelder, S. Malkusch, F. Fricke, M. Heilemann, A simple method to estimate the average localization precision of a single-molecule localization microscopy experiment. *Histochem. Cell Biol.* **141**, 629–638 (2014).
47. M. Metkar, H. Ozadam, B. R. Lajoie, M. Imakaev, L. A. Mirny, J. Dekker, M. J. Moore, Higher-Order Organization Principles of Pre-translational mRNPs. *Mol. Cell* **72**, 715-726.e3 (2018).
48. M. K. Geismann, A. Gomez-Segalas, A. Passera, M. Shirzadian, F. Balzarotti, A Fast Interferometric Beam Shaper for Multi-Emitter 3D MINFLUX. bioRxiv [Preprint] (2024). https://doi.org/10.1101/2023.12.09.570565.
49. N. Gimber, S. Strauss, R. Jungmann, J. Schmoranzer, Simultaneous Multicolor DNA-PAINT without Sequential Fluid Exchange Using Spectral Demixing. *Nano Lett.* **22**, 2682–2690 (2022).
50. N. Oleksiievets, Y. Sargsyan, J. C. Thiele, N. Mougios, S. Sograte-Idrissi, O. Nevskyi, I. Gregor, F. Opazo, S. Thoms, J. Enderlein, R. Tsukanov, Fluorescence lifetime DNA-PAINT for multiplexed super-resolution imaging of cells. *Commun. Biol.* **5**, 1–8 (2022).
51. A. Banerjee, M. Anand, M. Srivastava, V. S. Vidwath, M. Ganji, High-Speed Multiplexed DNA-PAINT Imaging of Nuclear Organization Using an Expanded Sequence Repertoire. bioRxiv [Preprint] (2025). https://doi.org/10.1101/2024.12.21.629871.
52. L. Le, S. K. Sreenivas, E. Fort, S. Lévêque-Fort, Brightness demixing for simultaneous multi-target imaging in 3D single-molecule localization microscopy. bioRxiv [Preprint] (2025). https://doi.org/10.1101/2025.03.02.639924.
53. M. Fazel, M. J. Wester, D. J. Schodt, S. R. Cruz, S. Strauss, F. Schueder, T. Schlichthaerle, J. M. Gillette, D. S. Lidke, B. Rieger, R. Jungmann, K. A. Lidke, High-precision estimation of emitter positions using Bayesian grouping of localizations. *Nat. Commun.* **13**, 7152 (2022).
54. J.-H. Su, P. Zheng, S. S. Kinrot, B. Bintu, X. Zhuang, Genome-Scale Imaging of the 3D Organization and Transcriptional Activity of Chromatin. *Cell*, S0092867420309405 (2020).
55. B. J. Beliveau, J. Y. Kishi, G. Nir, H. M. Sasaki, S. K. Saka, S. C. Nguyen, C. Wu, P. Yin, OligoMiner provides a rapid, flexible environment for the design of genome-scale oligonucleotide in situ hybridization probes. *Proc. Natl. Acad. Sci.* **115**, E2183–E2192 (2018).
56. K. C. Gwosch, J. K. Pape, F. Balzarotti, P. Hoess, J. Ellenberg, J. Ries, S. W. Hell, MINFLUX nanoscopy delivers 3D multicolor nanometer resolution in cells. *Nat. Methods*, 1–8 (2020).
57. F. Balzarotti, others, Nanometer resolution imaging and tracking of fluorescent molecules with minimal photon fluxes. *Science* **355**, 606–612 (2017).
58. N. Sofroniew, T. Lambert, G. Bokota, J. Nunez-Iglesias, P. Sobolewski, A. Sweet, L. Gaifas, K. Evans, A. Burt, D. Doncila Pop, K. Yamauchi, M. Weber Mendonça, L. Liu, G. Buckley, W.-M. Vierdag, T. Monko, L. Royer, A. Can Solak, K. I. S. Harrington, J. Ahlers, D. Althviz Moré, O. Amsalem, A. Anderson, A. Annex, C. Aronssohn, P. Boone, J. Bragantini, M. Bussonnier, C. Caporal, J. Eglinger, A. Eisenbarth, J. Freeman, C. Gohlke, K. Gunalan, Y. O. Halchenko, H. Har-Gil, M. Harfouche, V. Hilsenstein, K. Hutchings, J. Lauer, G. Lichtner, H. Liu, Z. Liu, A. Lowe, L. Marconato, S. Martin, A. McGovern, L. Migas, N. Miller, S. Miñano, H. Muñoz, J.-H. Müller, C. Nauroth-Kreß, H. A. Obenhaus, D. Palecek, C. Pape, E. Perlman, K. Pevey, G. Peña-Castellanos, A. Pierré, D. Pinto, J. Rodríguez-Guerra, D. Ross, C. T. Russell, J. Ryan, G. Selzer, M. Smith, P. Smith, K. Sofiiuk, J. Soltwedel, D. Stansby, J. Vanaret, P. Wadhwa, M. Weigert, C. Willing, J. Windhager, P. Winston, R. Zhao, napari: a multi-dimensional image viewer for Python, Zenodo (2025); https://doi.org/10.5281/zenodo.15779115.
59. P. J. A. Cock, T. Antao, J. T. Chang, B. A. Chapman, C. J. Cox, A. Dalke, I. Friedberg, T. Hamelryck, F. Kauff, B. Wilczynski, M. J. L. de Hoon, Biopython: freely available Python tools for computational molecular biology and bioinformatics. *Bioinformatics* **25**, 1422–1423 (2009).

Supplementary Information

Supplementary Notes

Supplementary Figures

Supplementary Tables

Supplementary Notes

Supplementary Note 1 Speed considerations of Combi-PAINT

Combinatorial multiplexing strategies are, in general, utilized to economize a scarce resource like the required measurement time, the number of readouts, the required energy, or the total signal available. In this note, we compare the required imaging time of standard DNA-PAINT multiplexing (non-combinatorial: NC) versus Combi-PAINT (combinatorial: C) under the constraint of equal probability of "double binding" event.

We define:

Symbol	Definition
H	Number of handles or targets
I	Number of imagers
$h \in \{1, \dots, H\}$	Index for handles
$i \in \{1, \dots, I\}$	Index for imagers
Hn_h	Handle names
Im_i	Imager names
$k_{\mathrm{on},i,h} = k_{\mathrm{on}}$	Molar binding rate of imager Im_i to handle Hn_h
C_i	Concentration of imager Im_i
$C_{\mathrm{max},i,h}$	Maximum tolerable concentration
N_i	Number of binding events of imager Im_i
t_i	Imaging time for imager Im_i
T	Total imaging time

Remarks:

- For the effects of this computations, we assume identical values of k_{on} for all imagers and handles.
- The non-combinatorial case corresponds to $I = H$, while the combinatorial case has $I < H$.
- We consider that the statistics of DNA binding events follows a Poisson distribution, with the average number of binding events N in a time t with an imager concentration C and a molar binding rate k_{on} yielding

$$N = k_{\mathrm{on}} C t \tag{1}$$

Non-combinatorial case

Here, the number of handles is equal to the number of imagers, $I = H$, therefore, the experiment requires H imaging rounds. From eq. (1), a single imaging round yields $N_i = k_{\mathrm{on}} C_i t_i$ binding events and the total imaging time is

$$T^{(\mathrm{NC})} = \sum_{i=1}^{I} t_i = I t_i = H t_i \tag{2}$$

where equal time is assumed for all imager rounds. This expression can also be written as

$$T^{(\mathrm{NC})} = \sum_{i=1}^{I} \frac{N_i}{C_i k_{\mathrm{on}}} = \frac{\sum_{i=1}^{I} N_i}{C k_{\mathrm{on}}} = \frac{H N_i}{C k_{\mathrm{on}}} \tag{3}$$

where C is the concentration of any imager and $I = H$ was utilized.

Comparison constrained by the probability of "double binding" event occurrence

We now focus on the case of high density, where many handle strands fall within the same diffraction-limited area, making them indistinguishable without SRM.

Defining $C_{\max}$ as the imager concentration that yields an acceptable probability of "double binding" events within a diffraction-limited area, the total imaging time of the non-combinatorial case of eq. 3 can be written as

$$T^{(\mathrm{NC})} = \sum_{i=1}^{H} \frac{N_i}{C_{\max,i}^{(\mathrm{NC})} k_{\mathrm{on},i}^{(\mathrm{NC})}} = H t_i^{(\mathrm{NC})} \tag{4}$$

For the combinatorial strategy, we define the density of each target species h as δ_h and, without loss of generality to make our point, we assume $\delta_h = \delta$. Likewise, we define $d_i = d$, the density of the target handles that bind any given imager, or "imager density".

In analogy to the pigeonhole principle, the combinatorial strategy effectively increases the "imager density" d by using less imaging strands than the non-combinatorial strategy. The specific ratio of imager density between both strategies, $d_{\mathrm{C}}/d_{\mathrm{NC}}$, depends on the specific combinatorial multiplexing scheme (see specific example below) and is equal to H/I. The equation for the imaging time per imager, in the combinatorial case, becomes

$$t_i^{(\mathrm{C})} = \frac{N_i^{(\mathrm{C})}}{C_{\max,i}^{(\mathrm{C})} k_{\mathrm{on},i}^{(\mathrm{C})}} = \frac{N_i^{(\mathrm{NC})}}{\left(C_{\max,i}^{(\mathrm{NC})} d_{\mathrm{NC}}/d_{\mathrm{C}}\right) k_{\mathrm{on},i}^{(\mathrm{NC})}} = \frac{d_{\mathrm{C}}}{d_{\mathrm{NC}}} t_i^{(\mathrm{NC})} = \frac{H}{I} t_i^{(\mathrm{NC})} \tag{5}$$

Here, we assume $N_i^{(\mathrm{C})} = N_i^{(\mathrm{NC})}$ and $k_{\mathrm{on},i}^{(\mathrm{C})} = k_{\mathrm{on},i}^{(\mathrm{NC})}$ because they are determined by the desired image quality and imager strand thermodynamics, which are not dependent on the chosen multiplexing strategy. In contrast, $C_{\max,i}^{(\mathrm{C})} = C_{\max,i}^{(\mathrm{NC})} d_{\mathrm{NC}}/d_{\mathrm{C}}$ because the increased imager strand binding site density imposes a proportional reduction in imager strand concentration to prevent overlapping blinking events. This leads to a proportional increase in imaging time. The equation for total imaging time then becomes

$$T^{(\mathrm{C})} = I t_i^{(\mathrm{C})} = I \frac{H}{I} t_i^{(\mathrm{NC})} = H t_i^{(\mathrm{NC})} = T^{(\mathrm{NC})} \tag{6}$$

Therefore, a speed advantage is obtained by having to perform less imager exchange rounds, which are especially time-consuming in dense, large samples like tissues, and goes from 2.5x less wash time (6-color NC imaging, 5 washes, versus 6-color C imaging, 2 washes), 4x less wash time (9-color NC imaging, 8 washes, versus 9-color C imaging, 2 washes) to 12.2x less wash time (62-color NC imaging, 61 washes, versus 62-color C imaging, 5 washes, Supplementary Fig. S4). Furthermore, if information about the spatial arrangement of the targets is available, Combi-PAINT provides a speed advantage uniquely due to multiplexing. For example, if one target is known to have a nuclear localization, while a second target is known to have a cytoplasmic membrane localization, these targets are not expected to lead to overlapping blinking events, even at high imager concentrations. Both targets can then bind to a given imager in a Combi-PAINT multiplexing scenario without the density of binding sites for that imager increasing, leading to a modification of eq. (7) that yields a strict improvement in imaging time.

This is analogous to the decrease in imaging time in multiplexing schemes like MERFISH compared to regular, non-combinatorial FISH: the spatial separation between particles allows the problem to be reduced to a pure decoding problem, in which the advantage of a combinatorial strategy is exactly equal to the reduction in rounds of imaging, H/I.

	Non-combinatorial label	**Combinatorial label**
Target 1	2xR1	2xR1
Target 2	2xR2	1xR1+1xR2
Target 3	2xR3	2xR2
K	3	3
I	3	2

Supplementary Figures

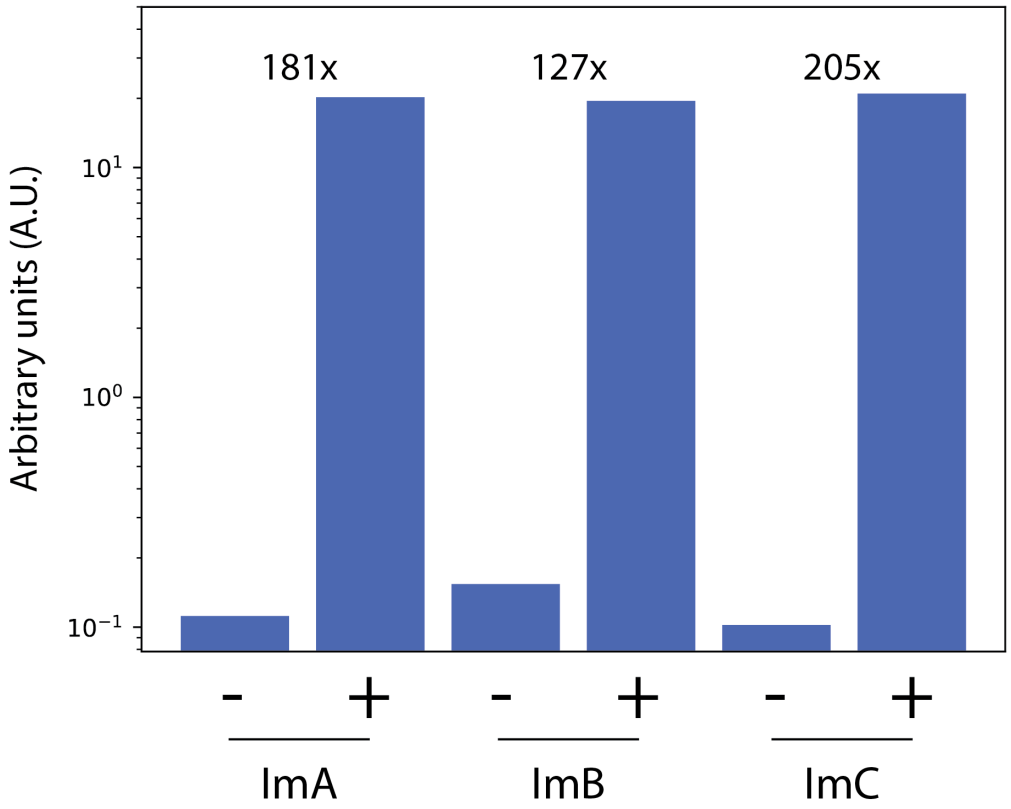

Supplementary Fig. S1 Fluorogenicity factors of green fluorogenic imagers.

Fluorogenicity factors for the Cy3b-ImA/B/C-BHQ2 strands, measured as described in Methods. The -/+ refers to the imager in the absence/presence of its reverse complement. Fluorogenicity factors are on top.

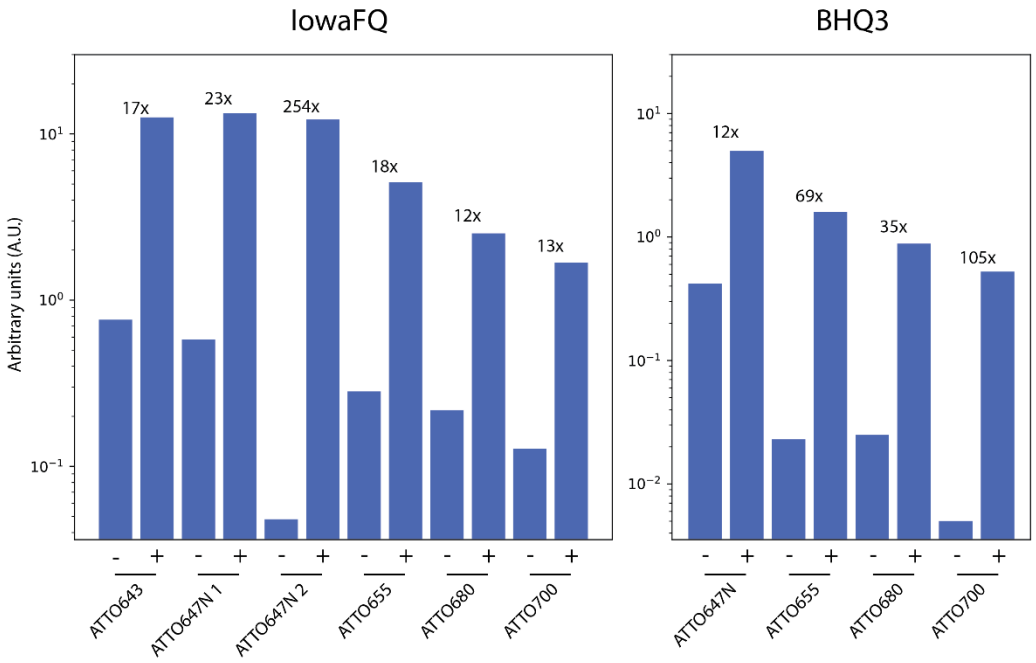

Supplementary Fig. S2 Fluorogenicity factors of far-red fluorogenic strands.

Fluorogenicity factors for the far-red ImB strands, measured as described in Methods. The -/+ refers to the imager in the absence/presence of its reverse complement. Fluorogenicity factors. Two quenchers were tested, IowaFQ and BHQ3. Fluorogenicity factors are on top. While BHQ3 showed higher fluorogenicity ratios on average, it also seemed to quench the dye in the bound state more than IowaFQ, leading to lower brightness in the bound state. If the setup is not limited by laser power, however, the higher fluorogenicity factor of BHQ3-labelled imagers could be of interest. Also, ATTO647N 1 and ATTO647N 2 refer to two different HPLC fractions of the ATTO647N conjugation. While ATTO647N 1 exhibits a fluorogenicity factor in line with the other dyes, ATTO647N 2 shows an exceptionally high factor, which could be of interest if ATTO647N is a suitable dye for an application.

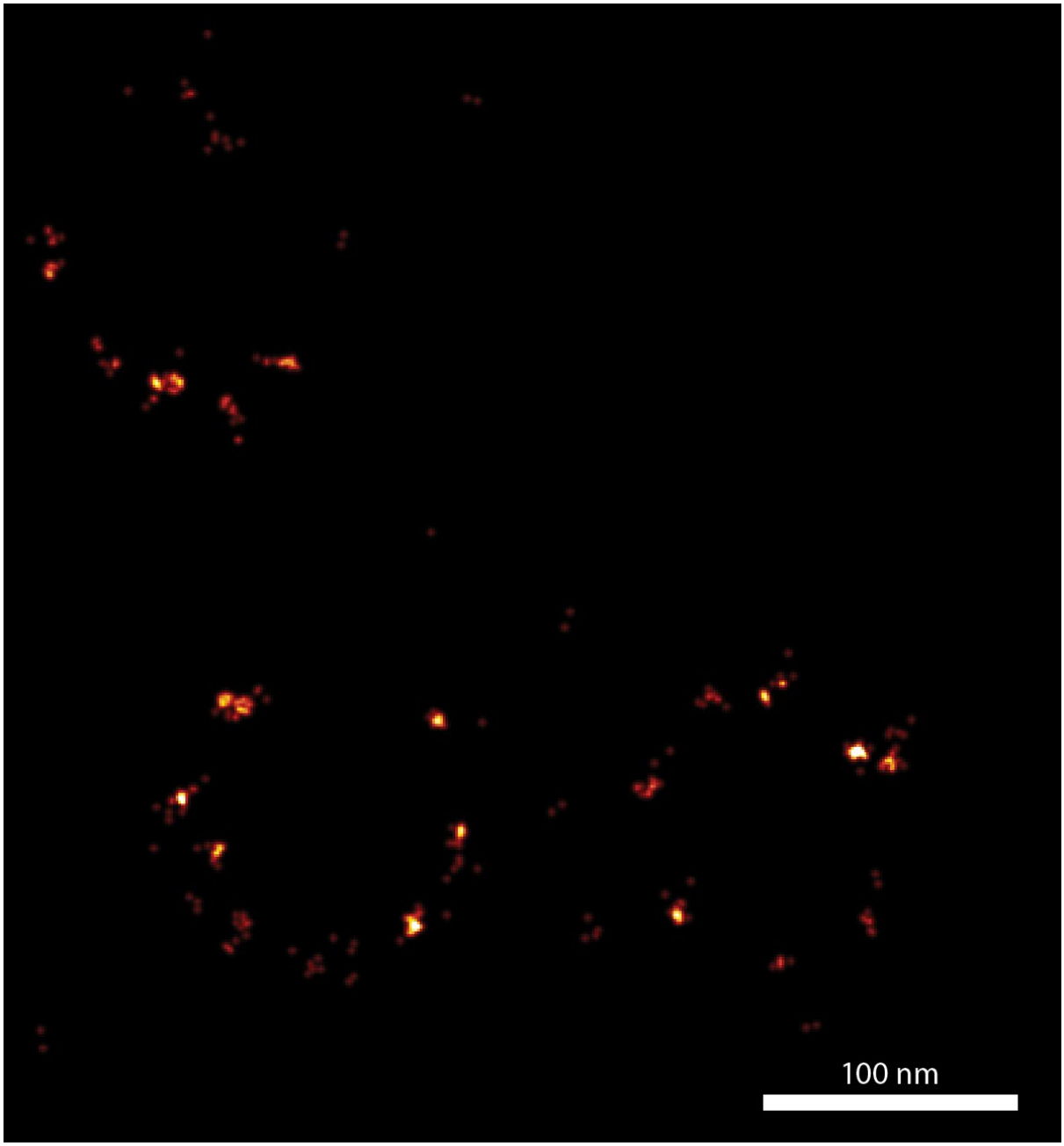

Supplementary Fig. S3 Nuclear pore complex imaging with mismatching imager.

2D MINFLUX imaging of a CRIPSR U2OS Nucleoporin96-GFP cell line, labelled with an αGFP nanobody tagged with HnA. The imager was acquired over the course of 20 minutes, with 2.5 nM of the fluorogenic imager ATTO655-ImA-IowaFQ.

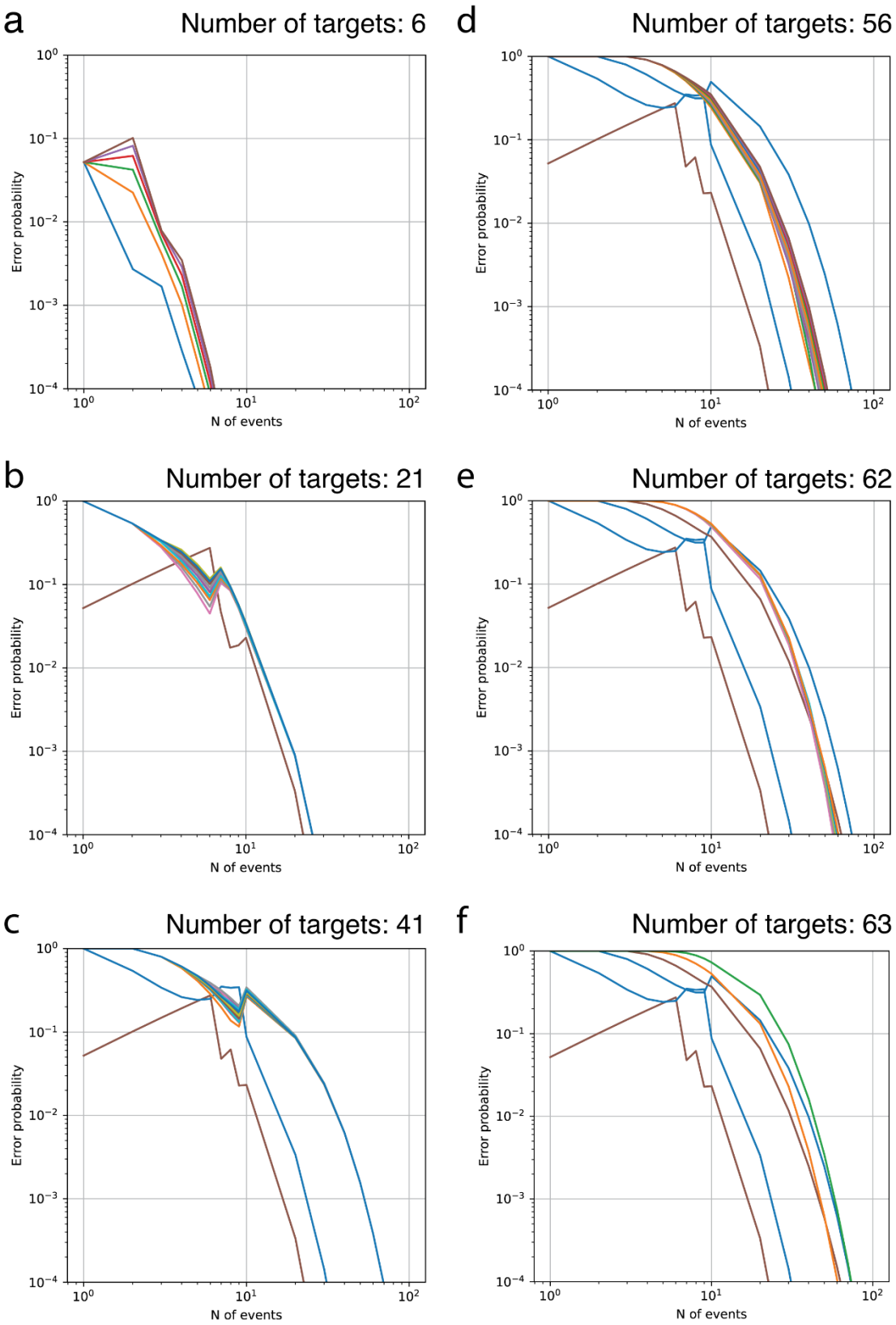

Supplementary Fig. S4 Error probabilities for a non-stoichiometric, 6-label approach.

Theoretical performance of a 6-label approach, as opposed to the 3-label approach used in this work. The legends are omitted for lack of enough separation and colors in the plot. All simulations assume a ~5% off-target binding, as in Supplementary Fig. S10 **a**, Simulation of a 6-color

approach (where each handle has a probability vector of the form $\mathbf{p} = (p_{R1}, p_{R2}, p_{R3}, p_{R4}, p_{R5}, p_{R6}) = \delta_i$, that is, the vector is 0 at all components except the i-th component, at which it is 1). 6 is $\binom{6}{1}$. **b**, Simulation of a 21-color approach ($\mathbf{p} = \delta_i$ or $\frac{1}{2}\delta_{i,j}$, that is, the vector is either as in the 6-color approach, or is 0 at all components except the i-th and j-th components, at which it is $\frac{1}{2}$, for some $(i,\ j),\ i < j$). 21 is $\binom{6}{1} + \binom{6}{2}$. **c**, Simulation of a 41-color approach ($\mathbf{p} = \delta_i$ or $\frac{1}{2}\delta_{i,j}$ or $\frac{1}{3}\delta_{i,j,k}$, for some $(i,\ j,\ k),\ i < j < k$). 41 is $\binom{6}{1} + \binom{6}{2} + \binom{6}{3}$. **d**, Simulation of a 56-color approach ($\mathbf{p} = \delta_i$ or $\frac{1}{2}\delta_{i,j}$ or $\frac{1}{3}\delta_{i,j,k}$ or $\frac{1}{4}\delta_{i,j,k,l}$, for some $(i,\ j,\ k,\ l),\ i < j < k < l$). 56 is $\binom{6}{1} + \binom{6}{2} + \binom{6}{3} + \binom{6}{4}$. **e**, Simulation of a 62-color approach ($\mathbf{p} = \delta_i$ or $\frac{1}{2}\delta_{i,j}$ or $\frac{1}{3}\delta_{i,j,k}$ or $\frac{1}{4}\delta_{i,j,k,l}$ or $\frac{1}{5}\delta_{i,j,k,l,m}$, for some $(i,\ j,\ k,\ l,\ m),\ i < j < k < l < m$). 62 is $\binom{6}{1} + \binom{6}{2} + \binom{6}{3} + \binom{6}{4} + \binom{6}{5}$. **f**, Simulation of a 63-color approach ($\mathbf{p} = \delta_i$ or $\frac{1}{2}\delta_{i,j}$ or $\frac{1}{3}\delta_{i,j,k}$ or $\frac{1}{4}\delta_{i,j,k,l}$ or $\frac{1}{5}\delta_{i,j,k,l,m}$ or $\frac{1}{6}\mathbf{1}$, for some $(i,\ j,\ k,\ l,\ m),\ i < j < k < l < m$) and $\mathbf{1}$ is the vector of ones. 63 is $\binom{6}{1} + \binom{6}{2} + \binom{6}{3} + \binom{6}{4} + \binom{6}{5} + \binom{6}{6}$.

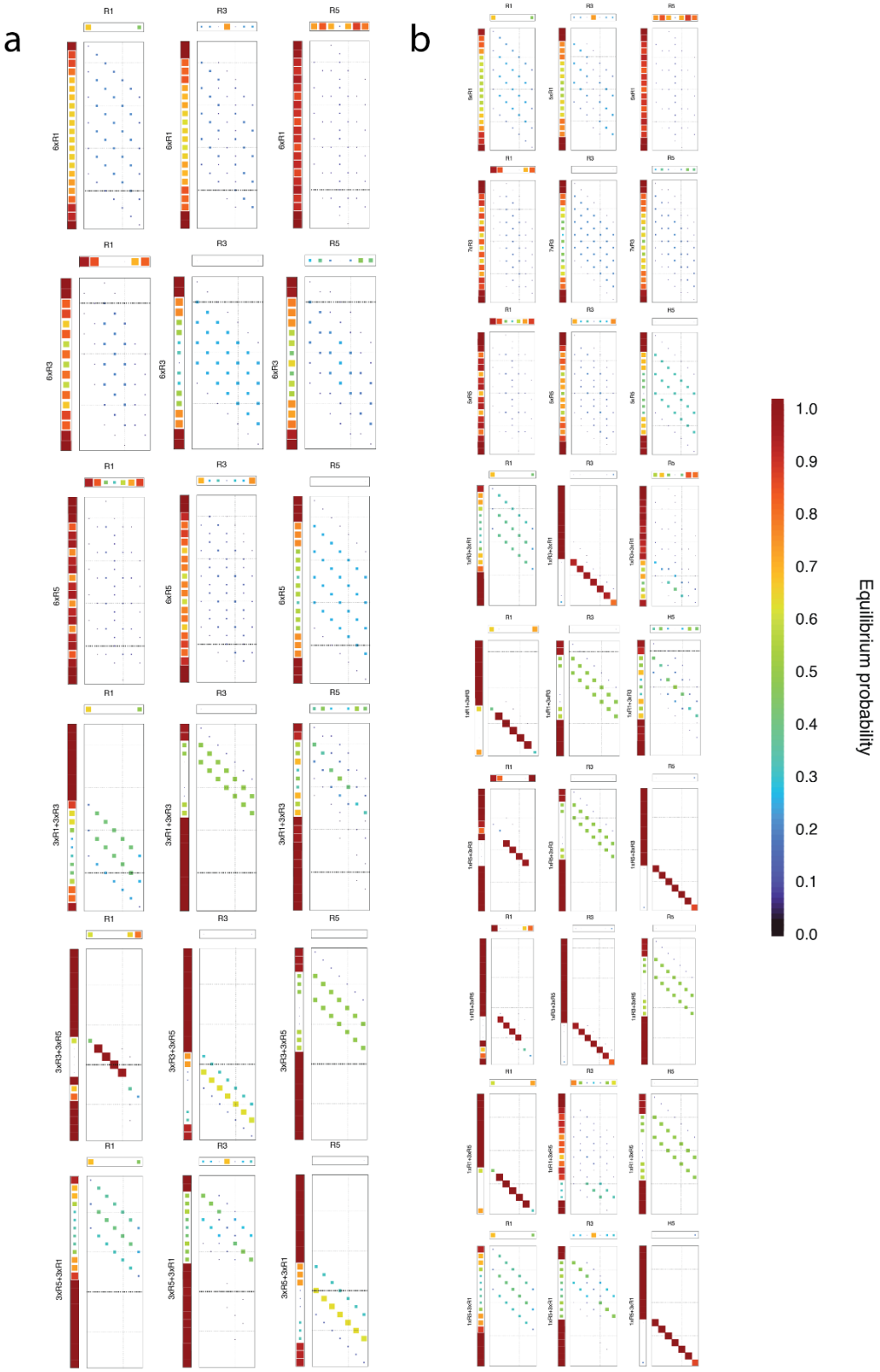

Supplementary Fig. S5 NUPACK predictions of modular multiplexing.

Pair probabilities of imager strands and handles for the 6-color (**a**) and 9-color (**b**) multiplexing strategies, as predicted by NUPACK. Predictions were calculated at 0°C, 0.5 M.

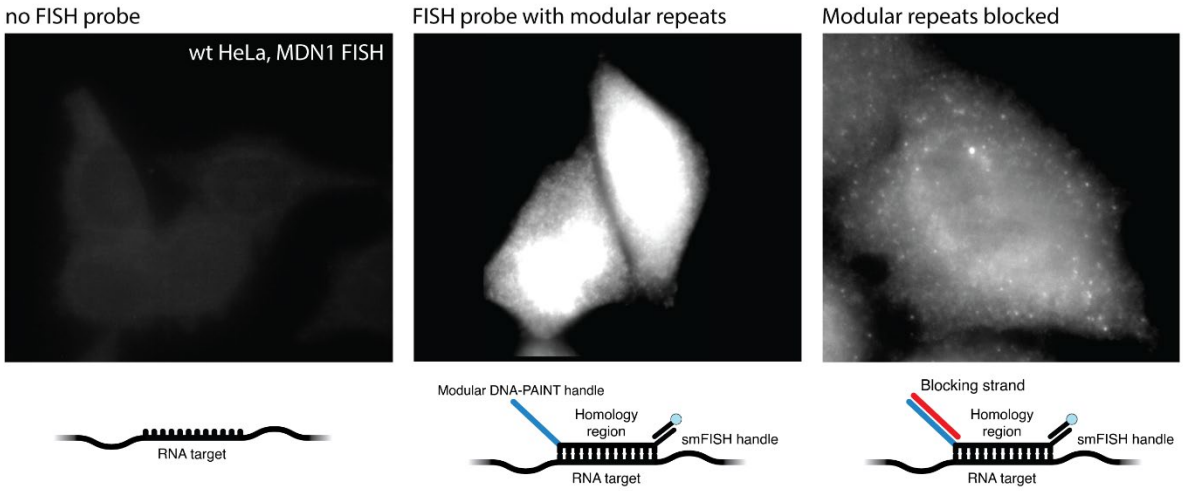

Supplementary Fig. S6 Module-based probe-induced RNA-FISH background.

Comparison between the background induced through FISH probes extended with the modular repeat DNA-PAINT handles. Left: negative control of a wt Hela cell with no FISH probes added, Middle: background induced by using the modular repeat extended FISH probes, Right: background is reduced when blocking the modular repeat extension by incubating the FISH probes with a fully complementary DNA strand prior to hybridization. Contrast and brightness are equal across panels.

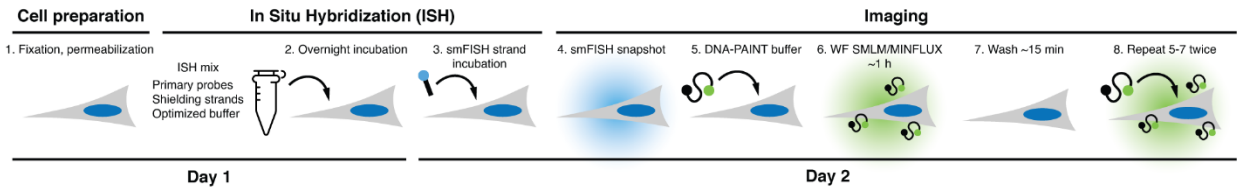

Supplementary Fig. S7 Graphical protocol of RNA-FISH DNA-PAINT.

Graphical protocol of RNA-FISH DNA-PAINT. The protocol takes 2 days (without considering cell seeding, which is cell-line dependent). Imaging can be performed immediately, or up to 2 days after sample preparation as described in the Methods. Longer times lead to a decrease in sample labelling efficiency and fluorescence background.

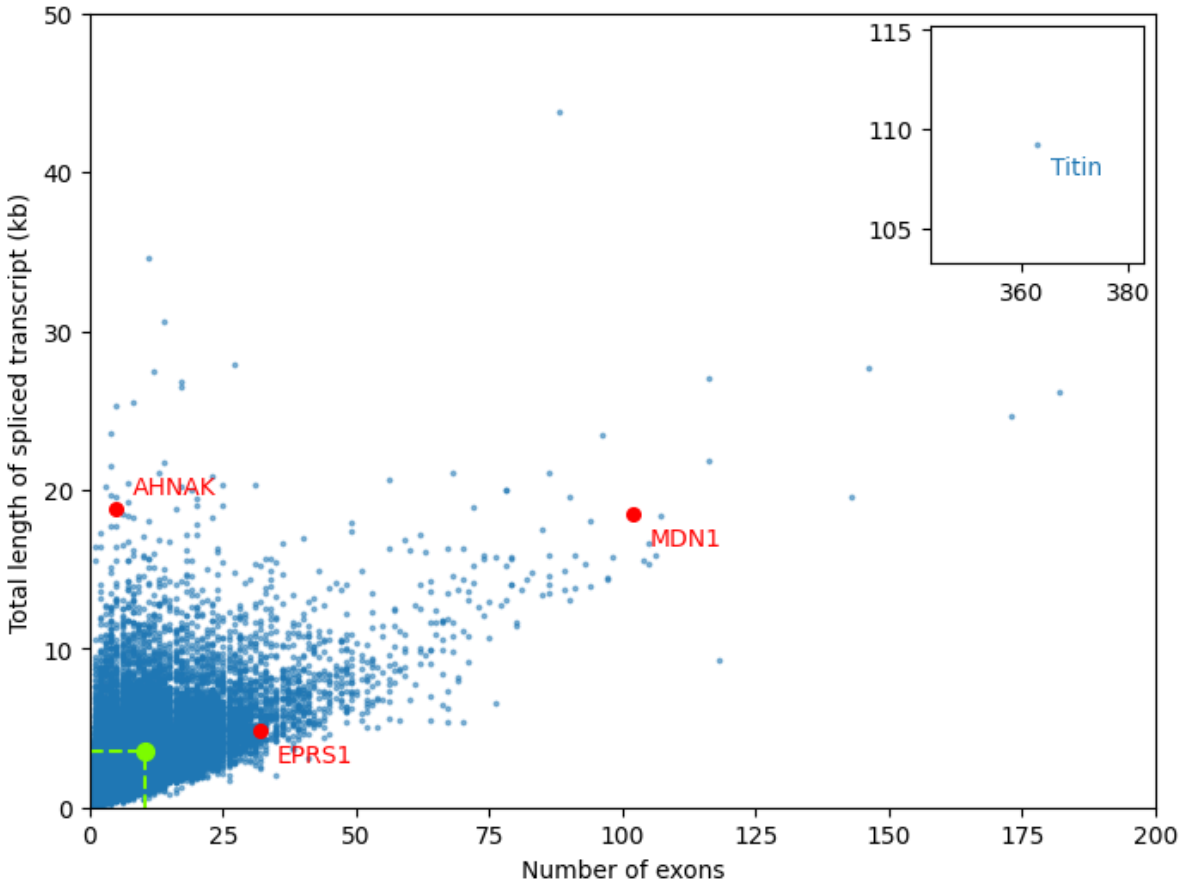

Supplementary Fig. S8 Gene length versus number of exons in the human genome.

Overview of number of spliced trascript length versus number of exons for the main isoform (as indicated by the Gencode APPRIS notation of main functional isoform or Transcript Support Level of 1) of all protein-coding human genes. The genes chosen in this study are highlighted, as is the mean of all genes (green).

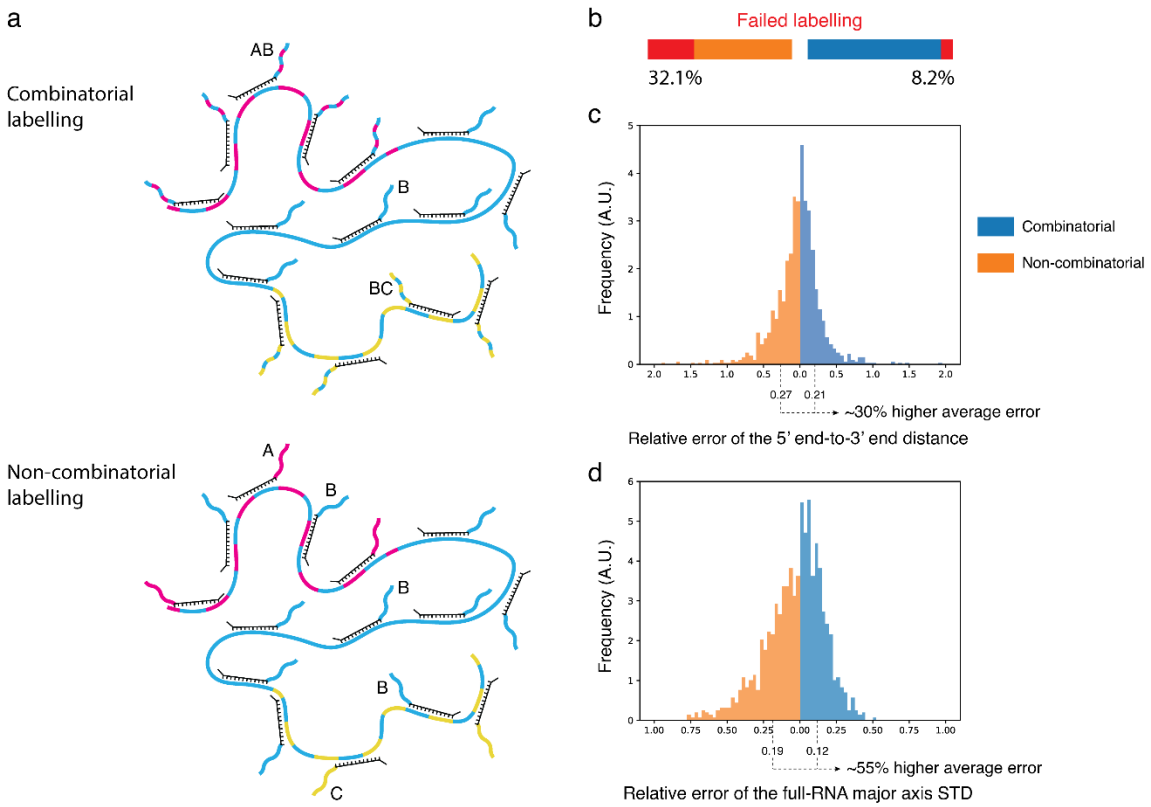

Supplementary Fig. S9: Combinatorial versus non-combinatorial multiplexing comparison

Comparison of the performance of a combinatorial multiplexing strategy and non-combinatorial multiplexing strategy. **a**. Top: combinatorial multiplexing strategy analyzed, bottom: non-combinatorial multiplexing strategy analyzed. In each case, the RNA transcript is subdivided into three segment (magenta-cyan, cyan, yellow-cyan). In the combinatorial case, each probe targeting the "combinatorial" regions (magenta-cyan and yellow-cyan) will bind to the magenta imager strand and the cyan imager strand. In the non-combinatorial case, each probe of a "combinatorial" region binds only one type of imager, effectively halving the number of probes for each imager strand. 1000 RNAs were simulated (random walk), each 5 kb long and with 100 probes equi-spaced along its length, assuming a 20% labelling efficiency and an average of 15 localizations with 5 nm sigma stemming from each probe. **b**. In the non-combinatorial case, the reduced number of probes combined with the stochasticity of probe binding increases the probability of not detecting any magenta or yellow signal by 4-fold. **c-d**. The under-labelling also affects the metrics reported from the transcript like 5' end-to-3' end distance (by about 30%, **c**) or major axis standard deviation of the entire RNA (cyan signal, by about 50%, **d**. Relative error $= |\mathrm{metric}_{\mathrm{combi\ or\ non-combi}} - \mathrm{metric}_{\mathrm{true}}|/\mathrm{metric}_{\mathrm{true}}$, where $\mathrm{metric}_{\mathrm{combi\ or\ non-combi}}$ refers to the value of the metric (5' end-to-3' end distance or major axis standard deviation) extracted from the simulated localizations in the combi or the non-combi case, while $\mathrm{metric}_{\mathrm{true}}$ refers to the true value of that metric in that simulation. The results presented hold true for any combination of simulation parameters, however, as they are a consequence of the under-sampling of non-combinatorial labelling.

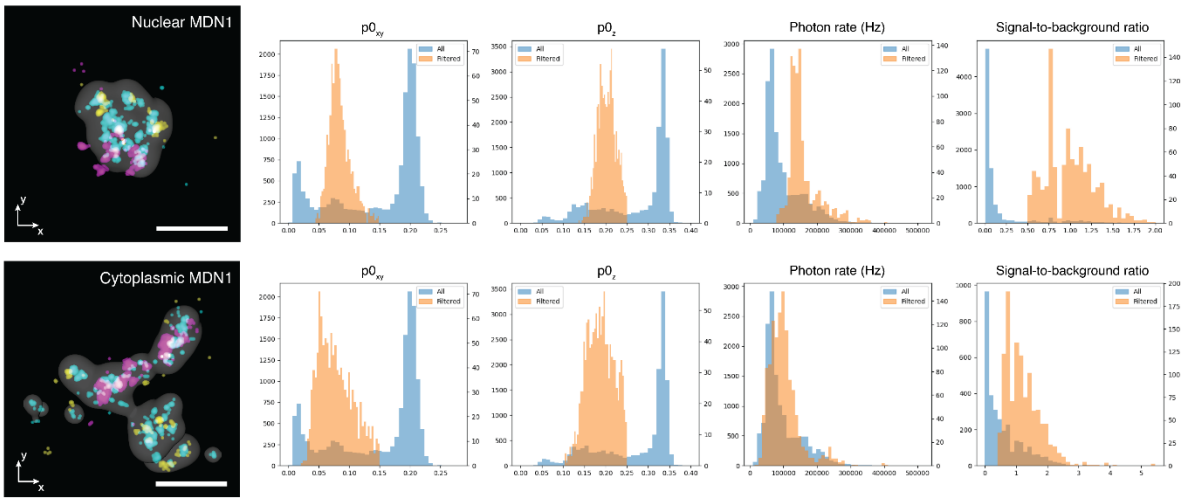

Supplementary Fig. S10 3D MINFLUX filtering parameters

Typical parameters and thresholds used for the filtering of 3D MINFLUX localizations. $p_{0\,xy}$ ($n_{0,vortex}/N_{vortex}$, the ratio of the photons from the central vortex in the last iteration and all vortex exposures in the last iteration), $p_{0\,z}$ ($n_{0,top\ hat}/N_{top\ hat}$, the ratio of the photons from the central top hat in the last iteration and all top hat exposures in the last iteration) and SBR (signal-to-background ratio). The photon rate (in Hz) can be used to filter double-blinking events, which are however also addressed by the p_0 ratios.

Supplementary Tables

Handle species	Matches with ImA	Matches with ImB	Matches with ImC	End matches	ΔG discrepancy (kcal/mol)	Wanted/ unwanted ΔG gap (kcal/mol)	ΔG self (kcal/mol)	ΔG ImA (kcal/mol)	ΔGImB (kcal/mol)	ΔG ImC (kcal/mol)
HnA	> 9	< 8	< 8	> 2	/	> 2	> -0.3	< -9.5	/	/
HnB	> 9	< 7	< 7	> 2	/	> 2	> -0.3	/	< -9.2	/
HnC	> 9	< 7	< 7	> 2	/	> 2	> -0.3	/	/	< -9.2
HnAB	> 9	> 9	/	/	< 0.5	> 2	> -0.3	< -9.2	< -9.2	/
HnBC	/	> 8	> 8	/	< 0.5	> 2	> -0.4	/	< -9.2	< -9.2
HnAC	> 8	< 8	> 8	/	< 0.5	> 2	> -0.4	< -9.2	/	< -9.2
HnABC	> 5	> 5	> 5	/	< 0.6	/	> -0.6	< -9.2	< -9.2	< -9.2

Supplementary Table 1 Filtering parameters for mismatching handles screening.

List of filters used during mismatching handle screening. “Matches with ImA/B/C” refers to matches between the imager and handle sequences aligned in frame (no secondary structure considered). “End matches” refers to a minumum number of consecutive matches at the 5’ and 3’. “ΔG discrepancy” refers to the maximum difference between the highest and lowest energies of the desired bindings (hence the handle must bind at least two imagers for this value to be available). “Wanted/unwanted ΔG gap” refers to the minimum difference between the highest energy (weakest binding) among desired bindings and the lowest energy (strongest binding) among undesired binding (hence the handle must not bind at least one imager for this value to be available). “ΔG self” refers to the energy of self-interaction, while “ΔG ImA/B/C” refers to the energy of binding between the handle and the imager.

Experiment	Imaging parameters	Imaging buffer	Microscope
Initial imager screening	20 ms, 100k frames, 45 W/cm^2	ImA- or ImB- or ImC-Cy3b: 10 nM, B+PCA/PCD/trolox, 12.5 mM $MgCl_2$	Elyra 7
Figure 2, SI Figure 4-5 (6 color mismatching)	150 ms, 25k/25k/25k frames, 380 W/cm^2	ImA/B/C-Cy3b: 5/2/10 nM, B+PCA/PCD/trolox, 12.5 mM $MgCl_2$	Custom setup, PCO edge 26
Figure 2 (6 col modular)	100 ms, 25k/25k/30k frames, 380 W/cm^2	R1/3/5-Cy3b: 500/750/1500 pM, B+PCA/PCD/trolox, 12.5 mM $MgCl_2$	Custom setup, PCO edge 26
Figure 2 (9 col modular)	100 ms, 25k/25k/35k frames, 380 W/cm^2	R1/3/5-Cy3b: 320/480/640 pM, B+PCA/PCD/trolox, 50 mM $MgCl_2$	Custom setup, PCO panda 4.2 bi
Widefield cell experiments	150 ms, 25k frames per round, ~400 W/cm^2	ImA/B/C-Cy3b: 10/5/15 nM, 1xPBS + 500 mM NaCl + PCA/PCD/trolox	Elyra 7

Supplementary Table 2 Imaging conditions of the widefield experiments.

Experimental conditions for widefield experiments. For the screening, each origami was measured with only one strand in solution, meaning for the mixed handles (HnAB, HnBC, HnAC) two separate experiments were done. The other experiments are Exchange PAINT experiments done over 3 rounds of imaging (R1/ImA -> R3/ImB -> R5/ImC) in the respective conditions.

Handle name	Notes	Sequence (5'->3'), including linker and padding
HnA	6 color mismatching, HnA8 in the screen	A **TATGTTACAAGGCCT** CG
HnB	6 color mismatching, HnB7 in the screen	T **TAGTCTCCCCCTCAT** CC
HnC	6 color mismatching, HnC7 in the screen	T **TGGTTCGATAATACT** AG
HnAB	6 color mismatching, HnAB3 in the screen	T **TATTTATTGGCGCAT** TT
HnBC	6 color mismatching, HnBC5 in the screen	T **TAGTTGTATCCGAGT** TT
HnAC	6 color mismatching, HnAC6 in the screen	T **TGGGTGTGGAGGCGT** AT
6xR1	6 color modular	TC **TCCTCCT**CCTCCTCCTCCTCCT
6xR3	6 color modular	TC **CTCTCTC**TCTCTCTCTC
6xR5	6 color modular	CC **CTTCTTC**TTCTTCTTCTTCTTC
3xR1+3xR3	6 color modular	TC **TCCTCCT**CCTCCT**CTCTCTC**
3xR3+3xR5	6 color modular	TC **CTCTCTC**TCTCCTTCTT**CTTCTT C**
3xR5+3xR1	6 color modular	CC **CTTCTTC**TTCTTCCTCC**TCCTCCT**
5xR1	9 color modular	TC **TCCTCCT**CCTCCTCCTCCT
7xR3	9 color modular	TC **CTCTCTC**TCTCTCTCTCTC
5xR5	9 color modular	CC **CTTCTTC**TTCTTCTTCTTC
1xR3+3xR1	9 color modular	TC **CTCTC**TCCTCC**TCCTCCT**
1xR1+3xR3	9 color modular	TC **TCCTC**CT**CTCTCTC**
1xR5+3xR3	9 color modular	CC **CTTCTTC**CCTCT**CTCTCTC**
1xR3+3xR5	9 color modular	TC **CTCTCTC**CTTCTT**CTTCTTC**
1xR1+3xR5	9 color modular	TC **TCCTCCT**TCTT**CTTCTTC**
1xR5+3xR1	9 color modular	CC **CTTCT**TCCTCC**TCCTCCT**

Supplementary Table 3 List of handle sequences.

List of the handles (mismatching and modular) used in this work. Each handle includes a dinucleotide linker (5' for modular sequences, 3' for mismatching sequences) and mismatching sequences have a 5' extra nucleotide as padding as in (*36*). Both linked and padding nucleotides were computed in NUPACK to minimize changes in the energies of self-interaction (for mismatching handles only) and of interaction with the imagers (for both handle types). Binding motifs are bold and underlined. For modular handles, the corresponding motifs are colored and shared nucleotides are in black; spacing nucleotides are highlighted in gray.

	ImA		**ImB**		**ImC**		GC fraction (%)
	$\Delta G_{binding}$ (kcal/mol)	Mismatches	$\Delta G_{binding}$ (kcal/mol)	Mismatches	$\Delta G_{binding}$ (kcal/mol)	Mismatches	
HnA	-9.65	4	-6.26	9	-6.95	9	40.00
HnB	-5.89	10	-9.63	4	-5.48	11	53.33
HnC	-6.58	10	-6.25	10	-9.85	3	33.33
HnAB	-9.72	5	-9.98	5	-6.86	9	33.33
HnBC	-6.57	8	-10.24	5	-10.47	4	40.00
HnAC	-10.14	6	-6.12	9	-9.72	6	66.66
GC fraction (%)	46.67		40		33.33		

Supplementary Table 4 List of thermodynamic parameters.

List of thermodynamic parameters for the imager-handle pairs presented. Each imager-handle combination reports the predicted binding energy in kcal/mol (calculated with NUPACK, calculated for 25°C, 50 mM Na^+ and 10 mM Mg^{2+} with model “dna04-nupack3” and ensemble “some-nupack3”) and number of mismatches for the aligned sequences. The last row/column contains the % GC content of the sequence in the column/row.

Product	5' mod.	Oligo sequence	3' mod.	Supplier	Conjugate
Cy3b-ImA-BHQ2	Amine	AGGCGTCATCACATA	BHQ2	Biosearch Technologies	Cy3b-NHS ester
Cy3b-ImB-BHQ2	Amine	ATGCGGAAAAGACTA	BHQ2	Biosearch Technologies	Cy3b-NHS ester
Cy3b-ImC-BHQ2	Amine	AGTCTTATACAACCA	BHQ2	Biosearch Technologies	Cy3b-NHS ester
ATTO643-ImA- IWFQ	Amine	AGGCGTCATCACATA	IWFQ	IDT	ATTO643-maleimide
ATTO643-ImB-IWFQ	Thiol	ATGCGGAAAAGACTA	IWFQ	IDT	ATTO643-maleimide
ATTO643-ImC- IWFQ	Amine	AGTCTTATACAACCA	IWFQ	IDT	ATTO643-maleimide
ATTO647N-ImB-IWFQ	Thiol	ATGCGGAAAAGACTA	IWFQ	IDT	ATTO647N-maleimide
ATTO655-ImA- IWFQ	Thiol	AGGCGTCATCACATA	IWFQ	IDT	ATTO655-maleimide
ATTO655-ImB- IWFQ	Thiol	ATGCGGAAAAGACTA	IWFQ	IDT	ATTO655-maleimide
ATTO680-ImB-IWFQ	Thiol	ATGCGGAAAAGACTA	IWFQ	IDT	ATTO680-maleimide
ATTO700-ImB-IWFQ	Thiol	ATGCGGAAAAGACTA	IWFQ	IDT	ATTO700-maleimide
ATTO647N-ImB-BHQ3	Thiol	ATGCGGAAAAGACTA	BHQ3	IDT	ATTO647N-maleimide
ATTO655-ImB-BHQ3	Thiol	ATGCGGAAAAGACTA	BHQ3	IDT	ATTO655-maleimide
ATTO680-ImB-BHQ3	Thiol	ATGCGGAAAAGACTA	BHQ3	IDT	ATTO680-maleimide
ATTO700-ImB-BHQ3	Thiol	ATGCGGAAAAGACTA	BHQ3	IDT	ATTO700-maleimide
R1-Cy3b		AGGAGGA	Amine	Sigma Aldrich	Cy3b-NHS ester
R3-Cy3b		GAGAGAG	Amine	Sigma Aldrich	Cy3b-NHS ester
R5-Cy3b		GAAGAAG	Amine	Sigma Aldrich	Cy3b-NHS ester

Supplementary Table 5 List of imager strand conjugations.

List of all performed conjugations. IWFQ is the Iowa Black FQ quencher.

	ImA (10^6 M^{-1} s^{-1})	**ImB** (10^6 M^{-1} s^{-1})	**ImC** (10^6 M^{-1} s^{-1})
HnA	0.730 ± 0.016	0.096 ± 0.028	0.003 ± 0.002
HnB	0.028 ± 0.005	1.622 ± 0.034	0.005 ± 0.001
HnC	0.018 ± 0.004	0.018 ± 0.008	0.787 ± 0.011
HnAB	0.784 ± 0.011	0.836 ± 0.016	0.006 ± 0.002
HnBC	0.035 ± 0.006	1.273 ± 0.017	0.141 ± 0.003
HnAC	0.532 ± 0.018	0.137 ± 0.016	0.423 ± 0.023

Supplementary Table 6 Association rate constant between fluorogenic imager-handle pairs.

Association rate constants (k_{on}) for the fluorogenic imager-handle family. ±: s.e.m.

	ImA (s^{-1})	**ImB** (s^{-1})	**ImC** (s^{-1})
HnA	1.05 ± 0.03	1.01 ± 0.28*	1.69 ± 0.5*
HnB	1.56 ± 0.23*	0.88 ± 0.03	0.94 ± 0.24*
HnC	1.79 ± 0.28*	0.73 ± 0.40*	0.95 ± 0.02
HnAB	1.11 ± 0.02	1.76 ± 0.05	1.86 ± 0.31*
HnBC	1.55 ± 0.17*	0.56 ± 0.02	2.73 ± 0.05
HnAC	0.70 ± 0.07	1.38 ± 0.28*	0.32 ± 0.09

Supplementary Table 7 Dissociation rate constant between fluorogenic imager-handle pairs.

List of k_{off} values for the imager-handle pairs presented ± s.e.m. Values marked by (*) have high errors as these combination kave low k_{on} values.

3 Discussion

3.1 A tool for DNA-PAINT combinatorial multiplexing applied to mRNA imaging and MINFLUX

In my PhD, I aimed at becoming a proficient and well-rounded microscopist, as well as to develop a tool for multiplexed DNA-PAINT imaging and to apply it on a novel sample of interest. In Section 2.1, I describe a MINFLUX prototype which I used and maintained in my PhD. I also show the preparation of samples, like DNA origami or nuclear pore samples, which were relevant for the entirety of my work. In Section 2.2 I show the core of my work, the design and realization of the combinatorial DNA-PAINT concept and its application to mRNA imaging.

3.1.1 MINFLUX at low signal-to-background ratio

The experience acquired with MINFLUX imaging and principles was instrumental to successfully perform MINFLUX DNA-PAINT RNA-FISH imaging in the nucleus. The signal-to-background (SBR) ratio in this compartment is especially low (typically ~1) due to several factors: the nucleus is a fully 3D environment (unlike DNA origamis or cellular membranes), so background due to diffusing imager strand or unspecific binding can come from any direction surrounding the confocal detection volume and not only from in-plane positions; also, the nucleus is a very dense environment due to the presence of chromatin and other components (Bona et al., 2019), meaning there is a large amount of surface that supports transient, unspecific binding of imager strands, which in the fluorogenic strand case might also imply unquenching. Several improvements of MINFLUX were necessary to perform robust, high-quality nuclear imaging: first, a theoretical result (Maya, Balzarotti et al., unpublished) showed that, at low SBR and when the duration of SMLM blinking events is independent of the emitted number of photons (such as in DNA-PAINT, in which binding time is dictated by the DNA sequence and unlike, for example, PALM, where event time is dictated by bleaching), a large MINFLUX pattern size provides optimal precision. This is an unintuitive result, since the widespread MINFLUX information theory implies that a smaller pattern size leads to higher localization precision, however, this applies only under fixed photons conditions. In the DNA-PAINT scenario, this works triple duty: not only we know that using a larger pattern size gives us better precision, but larger patterns also result in higher SBR (since the molecule will be far from the zero of some

of the MINFLUX beams, leading to larger photon counts while background stays unchanged). This condition leads to obtaining higher localization precision in a larger area around the true molecule position and downplays the importance of perfect convergence on top of the molecule for iterative MINFLUX. However, convergence on top of the molecule still needs to succeed, and this is difficult in high background scenarios like the nucleus, since background fluorescence near the confocal volume will affect the live position estimation of the binding event and possibly make the iterative MINFLUX convergence fail. This was solved by implementing a proportional-integral feedback loop within the convergence procedure on our MINFLUX microscope (Appendix). As opposed to the feedforward approach described in the introduction, a feedback loop approach continuously estimates the position of the fluorophore and gradually approaches it through the PI parameters of the loop. Feedback loops behave like low-pass filters, by only correcting for steady, true errors and is resilient to random background fluctuations. The feedforward approach would instead integrate the background into its estimation and, possibly, fail. Using DNA origami samples with different amounts of free fluorophore in solution, I proved that the two strategies perform equally well at high SBR, but the feedback loop is significantly more robust and precise at low SBR. The combination of these improvements allowed MINFLUX DNA-PAINT RNA-FISH imaging to happen.

3.1.2 Combinatorial DNA-PAINT

Section 2.2 shows combinatorial DNA-PAINT, an original approach to DNA-PAINT multiplexing which lowers the number of rounds necessary for imaging. While not strictly necessary to perform RNA-FISH super-resolved imaging, the technique is a welcome addition, as it cuts down on experimental complexity and, in the context of MINFLUX, where long-term drift can be detrimental, minimizing the number of washing steps is preferred. Combinatorial DNA-PAINT also reduces imaging time and provides insurance against unspecific binding by utilizing the colocalization of multiple signals on the same target.

Combinatorial DNA-PAINT aims to apply the powerful concept of combining labels, or barcoding, to DNA-PAINT super-resolution signals. Usually, the power of such approaches lies in the implicit assumption that each signal can be associated with negligible error to its source. For example, in MERFISH (Chen et al., 2015), a technique that allows massive combinatorial multiplexing of RNA-FISH targets, the

signal from each round of imaging is a sparse diffraction-limited signal and the sequential signals from multiple rounds can be overlapped and registered with certainty. As discussed in the Supplementary Note in Section 2.2, however, combinatorial DNA-PAINT is a more challenging scenario. By definition of super-resolution microscopy, we are trying to resolve objects closer to each other than the diffraction limit of light and, if a given label becomes too dense in the sample, this imposes a limit on the speed of imaging since imager strand concentration needs to be lowered to avoid the overlap of neighboring single-molecule signals. If all signals are assumed to be below the diffraction limit from each other, we derive that combinatorial DNA-PAINT does not provide a speed advantage beyond that of reducing the number of washing steps (but neither would any combinatorial strategy). If the assumption that some signals should not overlap can be made, however, then combinatorial DNA-PAINT does provide an imaging speed advantage, the factor of which depends on how the targets are known to be grouped. This applies, for example, for multiple targets whose sub-cellular localization is known to be non-overlapping, such as a nuclear target and a mitochondrial target. Especially in the context of cellular “spatial proteomics” (Schueder et al., 2024; Unterauer et al., 2024), such separation can be readily harvested to improve imaging speed greatly through combinatorial DNA-PAINT.

3.2 mRNA ultrastructure

RNA imaging of different transcripts gave us interesting insights into the ultrastructure of mRNPs in cells. First of all, we could recapitulate the reported result of an increased 5’ end-to-3’ end distance between nuclear and cytoplasmic MDN1 mRNAs (Adivarahan et al., 2018). However, super-resolution imaging provides more information. Overall mRNP size increases upon export also for the EPRS1 transcript, without a significant increase in 5’ end-to-3’ end distance. This change can only be observed since DNA-PAINT super-resolution returns a shape, as opposed to a 1D distance measurement between mRNA regions from diffraction-limited approaches. We do not detect any change in size for AHNAK1, which is on par with MDN1 in size before and after export. The fact MDN1 and EPRS1, which are the two intron-dense RNAs of our pool, undergo decompaction upon export is in line with recent models (Gromadzka et al., 2016; Pacheco-Fiallos et al., 2023) which assume nuclear mRNA compaction to be EJC-mediated. We also notice a larger size for MDN1 compared to

EPRS1 in each compartment, which is in line with MDN1 being approximately three times longer than EPRS1, and shows mRNP size to be proportional to RNA length for RNAs of similar intron density and not, for example, a fixed size. We partially confirm the expectation from electron microscopy of the average nuclear mRNP size to be between 30 and 70 nm (Pacheco-Fiallos et al., 2023). While “size” is ill-posed terminology when talking about a super-resolution blinking event density, a reference of twice the standard deviation along the major axis can be used, as it contains most of the mRNA signal. We observe nuclear EPRS1 and MDN1 particles fall in the higher part of the expected range or slightly exceed it, while AHNAK1 particles are larger. Estimations from electron microscopy inform us about the average, most represented particles, which are closer in length to EPRS1 than to the other RNAs we investigated. Rare and large AHNAK1 particles, for example, would not significantly skew the estimation, could be filtered during cryo-EM processing, or even be selected against by the purification method. Furthermore, the size of the mRNP measured with our method might contain contributions from flexible, isolated loops of mRNA which escape the core of the mRNP, and which would not provide enough contrast to be visible in electron microscopy.

Another shape descriptor we measured is the aspect ratio, with predictions of globular (Pacheco-Fiallos et al., 2023) or more elongated particles (Metkar et al., 2018) both present in the literature. While our data is 2D, aspect ratio measurements still hold and we show a mixed result: intron-rich nuclear particles adhere the closest to the globular model but are still elongated, with aspect ratios from 1 to 4, while other particles tended to have even higher aspect ratios. Overall, we observe elongated rather than spherical particles, meaning that the rounded nuclear mRNPs observed in electron microscopy could be an artifact of purification, sample preparation, or electron microscopy processing. We also do not detect a tendency of longer mRNAs to adopt more rodlike shapes (Faraway et al., 2025), as MDN1 nuclear particles are as elongated as the shorter EPRS1 mRNPs, possibly suggesting intron density to play a larger role in the globularity of the particle instead.

What can we say about the shape and ultrastructure of mRNAs in cells in the end? Nuclear mRNAs appear to be 1) elongated rather than globular and 2) likely randomly organized at small scales. The first feature is visible in the high aspect ratios as well as the visually complex shapes every transcript species assumes. This is in line with

the results of recent sequencing-based approaches (Metkar et al., 2018), and our images do fit in a “flexible rod” model rather than a globular model (Bonneau et al., 2023; Pacheco-Fiallos et al., 2023). The second feature is visible in both widefield and MINFLUX data as a grouping of signals: the 5’, middle and 3’ segments of the particles tend to group and to form “blobs” in which the signal of the segment is, on average, closer to itself than to the signal of other segments. This is, again, in line with sequencing-based approaches that found simple scaling laws based on primary sequence distance at short distance scales (Metkar et al., 2018). Apart from the intron-poor AHNAK1, cytoplasmic mRNPs appear to be larger and more elongated than nuclear ones, pointing to a reduced degree and different mode of compaction.

3D MINFLUX imaging provides an unprecedented view of mRNA, which is unfortunately stunted by MINFLUX’s limited throughput. With just a few particles for MDN1 and AHNAK1 in our dataset, we can only confirm several of the observations from widefield imaging: decompaction of MDN1 upon export, globular shapes for nuclear MDN1 as opposed to elongated cytoplasmic MDN1, similar shapes and sizes for AHNAK1 in the two compartments. We do, however, see in the MINFLUX images that most particles show complex, sometimes branched, shapes, often featuring “holes” deprived of mRNA signal which could hint at the presence of RNA-binding proteins and are not possible to capture with averaging approaches like electron microscopy or sequencing. It is now imperative to expand the technique and image other mRNP components, to study the regulation of these complex shapes and the relative localization of its players in the cellular context.

3.3 Future of combinatorial DNA-PAINT and DNA-PAINT RNA-FISH

Combinatorial DNA-PAINT provides a unique type of labelling, with signals from neighboring molecules which can overlap in one channel but not in another. This contains information which should be included to solve the clustering problem. The BaGoL algorithm (Fazel et al., 2022), which uses Bayesian clustering of localizations to optimally solve the clustering problem, can be extended to accept multi-channel data and would provide an increase in the effective resolution of the technique, given its excellent performance for single-channel data.

Also, the higher the degree of multiplexing, the higher the benefits of combinatorial DNA-PAINT. We limited ourselves to three types of imager, in the fluorogenic case, because of limitations imposed by imager length and number of mismatches on binding combinations, and in the speed-optimized case, so as to use purine-only imager strands and reap the k_{on} benefits of this choice (Schueder et al., 2019). However, more imagers can be used. Six speed-optimized imagers have been abundantly used in the literature (Strauss & Jungmann, 2020; Unterauer et al., 2024), and three more have been recently reported (Banerjee et al., 2025). Even considering only binary combinations of labels, this would allow 15- and 36-target imaging with 6 and 9 imagers respectively, greatly improving the multiplexing power of the technique and matching the needs of state-of-the-art highly-multiplexed protein imaging works (Schueder et al., 2024; Unterauer et al., 2024), where each binder must be carefully validated. When applied to RNA imaging, these strategies would allow higher multiplexing, either of more mRNAs in the same experiment, or of more regions of a given mRNA, akin to DNA tracing studies (Beckwith et al., 2025), which would provide a true polymer view of mRNA.

Multiplexing based on fluorogenic strands can also be improved. If imaging speed is a concern, imager strands with shorter binding times can be designed using the pipeline that was developed by enforcing weaker binding energies. If more multiplexing capabilities are desired, one can attempt to create more imager strands by first using the pipeline to screen for appropriate sequences and then using a high-throughput screening strategy to select the best performing sequences. In this regard, the MUSCLE technique (Aguirre Rivera et al., 2024) provides a great platform for such single-molecule kinetics screening, that would simultaneously also provide a rich dataset to study the effect of nucleotide mismatches on DNA binding kinetics, something which is still missing from DNA models (Zhang et al., 2018). Finally, our strands are not speed-optimized, as at least three nucleotide types are needed according to our mathematical model and this makes it impossible to avoid intramolecular base pairing, thus reducing the k_{on} of the strands. However, if commercially-available nucleotides analogues are included, such as 2-deoxynebularine (Eritja et al., 1986), then purine-only and pyrimidine-only strands are possible, while still retaining the purinic/pyrimidinic structure to assist with intramolecular base-stacking.

On the side of RNA-FISH studies, many improvements will be and are being made. As shown in the Supplementary Information in Section 2.2, we used the fluorogenic strand implementation of combinatorial DNA-PAINT because the repetitive docking strands sequences of speed-optimized DNA-PAINT showed unspecific binding under RNA-FISH conditions. However, preliminary experiments with primary RNA-FISH probes sporting intermediate adapters which after RNA-FISH hybridization bring repeating DNA-PAINT handles, similarly to SUM-PAINT (Unterauer et al., 2024), have shown no unspecific binding and allow to harvest the higher k_{on} and higher ceiling for multiplexing of these sequences.

A limitation of our work is the investigation of only three transcript species which, while spanning a wide range of gene features, are few and often pathological in some regard (abnormal length, abnormal intron density, etc.). An avenue to extend to more transcripts, which we are using, is to employ so called “bulk libraries”. These libraries contain probes against several transcripts, which were chosen to have similar expression levels within a library but different combinations of length and intron density across libraries. This allows not only to probe multiple transcripts, providing stronger evidence for biological claims, but also to obtain several times more particles per experiment, increasing throughput, which is especially beneficial for MINFLUX imaging. Preliminary experiments with libraries for long genes with high intron density (e.g., MDN1) or low intron density (e.g., AHNAK1) recapitulate results for nuclear/cytoplasmic size and aspect ratio obtained in Section 2.2. These libraries will also allow to explore the features of the more average transcripts, those of medium length and moderate intron density, which were notably excluded from our initial choices. The use of synthetic genes, with a programmed number and distribution of introns, could also provide an elegant platform for checking specific hypotheses.

As more particles will be available, more refined tools to analyze mRNP ultrastructure will be needed. The simple parameters chosen in our study provided a straightforward and intuitive way to describe particles but lack the capability to describe more complex shapes. Especially since the custom widefield system has now 3D imaging capabilities, using a large suite of shape descriptors, for which there are precedents and tools (Hugelier et al., 2024; Unterauer et al., 2024), will provide a suitable description of mRNP shape complexity.

While obtaining super-resolved pictures of mRNA is exciting and the goal of this work, it will always be desired to image proteins simultaneously to obtain insight of the entire mRNP. Preliminary work in the lab by me and others on recent labelling techniques, like exchangeable HaloTag ligands (Kompa et al., 2023) and self-blinking dyes (Holland et al., 2024) has allowed us to perform RNA-FISH-protein co-imaging also of challenging targets such as the EJC component eIF4A3 or the THO complex component THOC5, both of which are highly abundant proteins, which are difficult to image with standard approaches like STORM due to the blinking duty cycle of the fluorophores. eIF4A3 is also a protein which has been shown not to be addressable via nanobodies when part of mRNPs (Pacheco-Fiallos et al., 2023), meaning these more advanced labelling strategies based on small molecules are needed to see it and, possibly, other inner mRNP components like SR proteins or hnRNPs.

In conclusion, I have developed a tool to simplify multiplexed DNA-PAINT imaging and provided the basis for imaging mRNA at sub-transcript resolution and nanometer spatial precision in cells. While mainly a work focused on developing a method, we gathered first insight into the ultrastructure of mRNA in mRNPs. As with any method, however, the questions that arise are more than the ones that are answered. For example, we did not observe significant nuclear compaction for the AHNAK1 transcript. How does this affect its nuclear diffusion and retention time, its propensity to degradation and its export through the nuclear pore complex? Can this observation be extended to other intron-poor and intron-less transcripts? Would a synthetic AHNAK1 gene with same intron number but different intron distribution display the same behavior? Since the 5’ and 3’ ends of mRNA seem to occupy defined subregions in the mRNP, do they also locate at a preferential position in the mRNP, and does this have a functional role? Do mRNP size and shape depend on intron density, and if so with which scaling law? Are the (unintuitive) non-convex and branched shapes we observed physiological for mRNAs, or are they the result of the presence of binding proteins or complexes which prevent RNA-FISH probe labelling? I hope this tool will provide an avenue to answer these questions and, overall, simplify highly multiplexed, high resolution DNA-PAINT imaging of any target of interest.

4 Appendix

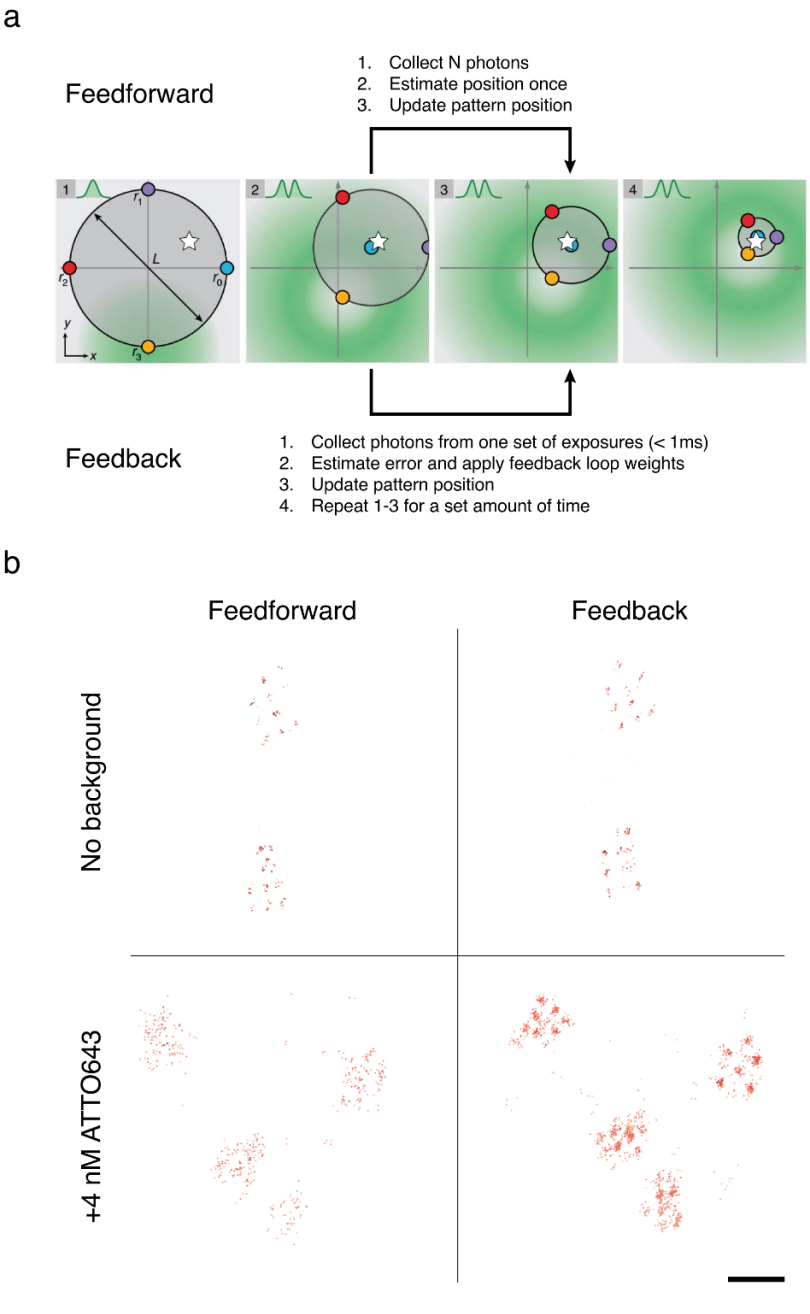

Comparison of feedforward and feedback-based iterative MINFLUX convergence. (**A**): iterative MINFLUX diagram from (Gwosch et al., 2020) with explanation of feedforward and feedback convergence. (**B**): xy projection of 3D MINFLUX DNA-PAINT measurements of 20 nm-grid DNA origami (4 nM ImB-ATTO643). The same region was imaged using feedforward and feedback loop convergence approaches, with or without the addition of 4 nM ATTO643 in solution as background. While in the absence of background both approaches yield high-quality images, background causes feedforward convergence to fail. Feedback loop convergence still succeeds, with the lower precision compared to the background-free scenario being due to lower SBR. Scale bar = 50 nm.

4.1 Confirmation of manuscript submission

The manuscript described in section 2.1, “A Fast Interferometric Beam Shaper for Multi-Emitter 3D MINFLUX”, was published on bioRxiv on 15 February 2024, DOI: https://doi.org/10.1101/2023.12.09.570565.

The manuscript described in section 2.2, “Super-resolved imaging of mRNA ultrastructure in cells”, was published on bioRxiv on 23 January 2026, DOI: https://doi.org/10.64898/2026.01.23.701081 and was submitted to Nature Methods on 18 December 2025.

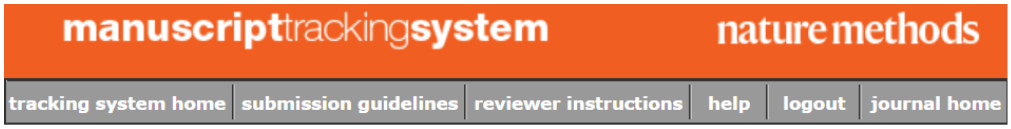

Detailed Status Information

Manuscript #	NMETH-A64102
Current Revision #	0
Submission Date	18th Dec 25
Current Stage	All Reviewers Assigned
Title	Super-resolved imaging of mRNA ultrastructure in cells
Manuscript Type	Article
Collection	N/A

5 References

Adivarahan, S., Livingston, N., Nicholson, B., Rahman, S., Wu, B., Rissland, O. S., & Zenklusen, D. (2018). Spatial Organization of Single mRNPs at Different Stages of the Gene Expression Pathway. *Molecular Cell*, *72*(4), 727-738.e5. https://doi.org/10.1016/j.molcel.2018.10.010

Aguirre Rivera, J., Mao, G., Sabantsev, A., Panfilov, M., Hou, Q., Lindell, M., Chanez, C., Ritort, F., Jinek, M., & Deindl, S. (2024). Massively parallel analysis of single-molecule dynamics on next-generation sequencing chips. *Science*, *385*(6711), 892–898. https://doi.org/10.1126/science.adn5371

Antolovic, I. M., Burri, S., Bruschini, C., Hoebe, R. A., & Charbon, E. (2017). SPAD imagers for super resolution localization microscopy enable analysis of fast fluorophore blinking. *Scientific Reports*, *7*(1), 44108. https://doi.org/10.1038/srep44108

Asada, R., Dominguez, A., & Montpetit, B. (2023). Single-molecule quantitation of RNA-binding protein occupancy and stoichiometry defines a role for Yra1 (Aly/REF) in nuclear mRNP organization. *Cell Reports*, *42*(11), 113415. https://doi.org/10.1016/j.celrep.2023.113415

Balzarotti, F., Eilers, Y., Gwosch, K. C., Gynnå, A. H., Westphal, V., Stefani, F. D., Elf, J., & Hell, S. W. (2017). Nanometer resolution imaging and tracking of fluorescent molecules with minimal photon fluxes. *Science*, *355*(6325), 606–612. https://doi.org/10.1126/science.aak9913

Banerjee, A., Anand, M., Srivastava, M., Vidwath, V. S., & Ganji, M. (2025). *High-Speed Multiplexed DNA-PAINT Imaging of Nuclear Organization Using an Expanded Sequence Repertoire* (p. 2024.12.21.629871). bioRxiv. https://doi.org/10.1101/2024.12.21.629871

Beckwith, K. S., Brunner, A., Morero, N. R., Jungmann, R., & Ellenberg, J. (2025). Nanoscale DNA tracing reveals the self-organization mechanism of mitotic chromosomes. *Cell*, *188*(10), 2656-2669.e17. https://doi.org/10.1016/j.cell.2025.02.028

Berrevoets, E. S., Kessler, L. F., Balakrishnan, A., Okuda, E. K., Müller-McNicoll, M., Rieger, B., Stallinga, S., & Heilemann, M. (2025). Smart 3D super-resolution microscopy reveals the architecture of the RNA scaffold in a nuclear body. *Nature Communications*, *16*(1), 10689. https://doi.org/10.1038/s41467-025-65723-x

Betzig, E. (1995). Proposed method for molecular optical imaging. *Optics Letters*, *20*(3), 237–239. https://doi.org/10.1364/OL.20.000237

Betzig, E., Patterson, G. H., Sougrat, R., Lindwasser, O. W., Olenych, S., Bonifacino, J. S., Davidson, M. W., Lippincott-Schwartz, J., & Hess, H. F. (2006). Imaging Intracellular Fluorescent Proteins at Nanometer Resolution. *Science*, *313*(5793), 1642–1645. https://doi.org/10.1126/science.1127344

Bona, M. D., Mancini, M. A., Mazza, D., Vicidomini, G., Diaspro, A., & Lanzanò, L. (2019). Measuring Mobility in Chromatin by Intensity-Sorted FCS. *Biophysical Journal*, *116*(6), 987–999. https://doi.org/10.1016/j.bpj.2019.02.003

Bonneau, F., Basquin, J., Steigenberger, B., Schäfer, T., Schäfer, I. B., & Conti, E. (2023). Nuclear mRNPs are compact particles packaged with a network of proteins promoting RNA–RNA interactions. *Genes & Development*, *37*(11–12), 505–517. https://doi.org/10.1101/gad.350630.123

Bossi, M., Fölling, J., Belov, V. N., Boyarskiy, V. P., Medda, R., Egner, A., Eggeling, C., Schönle, A., & Hell, S. W. (2008). Multicolor Far-Field Fluorescence Nanoscopy through Isolated Detection of Distinct Molecular Species. *Nano Letters*, *8*(8), 2463–2468. https://doi.org/10.1021/nl801471d

Chen, K. H., Boettiger, A. N., Moffitt, J. R., Wang, S., & Zhuang, X. (2015). Spatially resolved, highly multiplexed RNA profiling in single cells. *Science*, *348*(6233), aaa6090. https://doi.org/10.1126/science.aaa6090

Chung, K. K. H., Zhang, Z., Kidd, P., Zhang, Y., Williams, N. D., Rollins, B., Yang, Y., Lin, C., Baddeley, D., & Bewersdorf, J. (2022). Fluorogenic DNA-PAINT for faster, low-background super-resolution imaging. *Nature Methods*, 1–6. https://doi.org/10.1038/s41592-022-01464-9

Cnossen, J., Hinsdale, T., Thorsen, R. Ø., Siemons, M., Schueder, F., Jungmann, R., Smith, C. S., Rieger, B., & Stallinga, S. (2020). Localization microscopy at doubled precision with patterned illumination. *Nature Methods*, *17*(1), 59–63. https://doi.org/10.1038/s41592-019-0657-7

Deguchi, T., Iwanski, M. K., Schentarra, E.-M., Heidebrecht, C., Schmidt, L., Heck, J., Weihs, T., Schnorrenberg, S., Hoess, P., Liu, S., Chevyreva, V., Noh, K.-M., Kapitein, L. C., & Ries, J. (2023). Direct observation of motor protein stepping in living cells using MINFLUX. *Science*, *379*(6636), 1010–1015. https://doi.org/10.1126/science.ade2676

Domínguez-Sánchez, M. S., Barroso, S., Gómez-González, B., Luna, R., & Aguilera, A. (2011). Genome Instability and Transcription Elongation Impairment in Human Cells Depleted of THO/TREX. *PLOS Genetics*, *7*(12), e1002386. https://doi.org/10.1371/journal.pgen.1002386

Eilers, Y., Ta, H., Gwosch, K. C., Balzarotti, F., & Hell, S. W. (2018). MINFLUX monitors rapid molecular jumps with superior spatiotemporal resolution. *Proceedings of the National Academy of Sciences*, *115*(24), 6117–6122. https://doi.org/10.1073/pnas.1801672115

Eritja, R., Horowitz, Daniel. M., Walker, Peter. A., Ziehler-Martin, J. P., Boosalis, Michael. S., Goodman, Myron. F., Itakura, K., & Kaplan, Bruce. E. (1986). Synthesis and properties of oligonucleotides containing 2'-deoxynebularine and 2'-deoxyxanthosine. *Nucleic Acids Research*, *14*(20), 8135–8153. https://doi.org/10.1093/nar/14.20.8135

Faraway, R., Zenklusen, D., & Plaschka, C. (2025). Mechanisms of Messenger RNA Packaging and Export. *Annual Review of Cell and Developmental Biology*, *41*(1), 479–504. https://doi.org/10.1146/annurev-cellbio-101123-045256

Fazel, M., Wester, M. J., Schodt, D. J., Cruz, S. R., Strauss, S., Schueder, F., Schlichthaerle, T., Gillette, J. M., Lidke, D. S., Rieger, B., Jungmann, R., & Lidke, K. A. (2022). High-precision estimation of emitter positions using Bayesian grouping of localizations. *Nature Communications*, *13*(1), 7152. https://doi.org/10.1038/s41467-022-34894-2

Femino, A. M., Fay, F. S., Fogarty, K., & Singer, R. H. (1998). Visualization of Single RNA Transcripts in Situ. *Science*, *280*(5363), 585–590. https://doi.org/10.1126/science.280.5363.585

Geuens, T., Bouhy, D., & Timmerman, V. (2016). The hnRNP family: Insights into their role in health and disease. *Human Genetics*, *135*(8), 851–867. https://doi.org/10.1007/s00439-016-1683-5

Gimber, N., Strauss, S., Jungmann, R., & Schmoranzer, J. (2022). Simultaneous Multicolor DNA-PAINT without Sequential Fluid Exchange Using Spectral Demixing. *Nano Letters*, *22*(7), 2682–2690. https://doi.org/10.1021/acs.nanolett.1c04520

Gromadzka, A. M., Steckelberg, A.-L., Singh, K. K., Hofmann, K., & Gehring, N. H. (2016). A short conserved motif in ALYREF directs cap- and EJC-dependent assembly of export complexes on spliced mRNAs. *Nucleic Acids Research*, *44*(5), 2348–2361. https://doi.org/10.1093/nar/gkw009

Gwosch, K. C., Pape, J. K., Balzarotti, F., Hoess, P., Ellenberg, J., Ries, J., & Hell, S. W. (2020). MINFLUX nanoscopy delivers 3D multicolor nanometer resolution in cells. *Nature Methods*, *17*(2), Article 2. https://doi.org/10.1038/s41592-019-0688-0

Hell, S. W., & Wichmann, J. (1994). Breaking the diffraction resolution limit by stimulated emission: Stimulated-emission-depletion fluorescence microscopy. *Optics Letters*, *19*(11), 780–782. https://doi.org/10.1364/OL.19.000780

Hess, S. T., Girirajan, T. P. K., & Mason, M. D. (2006). Ultra-High Resolution Imaging by Fluorescence Photoactivation Localization Microscopy. *Biophysical Journal*, *91*(11), 4258–4272. https://doi.org/10.1529/biophysj.106.091116

Holland, K. L., Plutkis, S. E., Daugird, T. A., Sau, A., Grimm, J. B., English, B. P., Zheng, Q., Dave, S., Rahman, F., Xie, L., Dong, P., Tkachuk, A. N., Brown, T. A., Singer, R. H., Liu, Z., Galbraith, C. G., Musser, S. M., Legant, W. R., & Lavis, L. D. (2024). *A series of spontaneously blinking dyes for super-resolution microscopy* (p. 2024.02.23.581625). bioRxiv. https://doi.org/10.1101/2024.02.23.581625

Huang, B., Wang, W., Bates, M., & Zhuang, X. (2008). Three-Dimensional Super-Resolution Imaging by Stochastic Optical Reconstruction Microscopy. *Science*, *319*(5864), 810–813. https://doi.org/10.1126/science.1153529

Huang, K., Demirci, F., Batish, M., Treible, W., Meyers, B. C., & Caplan, J. L. (2020). Quantitative, super-resolution localization of small RNAs with sRNA-PAINT. *Nucleic Acids Research*, *48*(16), e96. https://doi.org/10.1093/nar/gkaa623

Hugelier, S., Tang, Q., Kim, H. H.-S., Gyparaki, M. T., Bond, C., Santiago-Ruiz, A. N., Porta, S., & Lakadamyali, M. (2024). ECLiPSE: A versatile classification technique for structural and morphological analysis of 2D and 3D single-molecule localization microscopy data. *Nature Methods*, *21*(10), 1909–1915. https://doi.org/10.1038/s41592-024-02414-3

Jungmann, R., Avendaño, M. S., Woehrstein, J. B., Dai, M., Shih, W. M., & Yin, P. (2014). Multiplexed 3D cellular super-resolution imaging with DNA-PAINT and Exchange-PAINT. *Nature Methods*, *11*(3), Article 3. https://doi.org/10.1038/nmeth.2835

Jungmann, R., Steinhauer, C., Scheible, M., Kuzyk, A., Tinnefeld, P., & Simmel, F. C. (2010). Single-Molecule Kinetics and Super-Resolution Microscopy by Fluorescence Imaging of Transient Binding on DNA Origami. *Nano Letters*, *10*(11), 4756–4761. https://doi.org/10.1021/nl103427w

Klar, T. A., & Hell, S. W. (1999). Subdiffraction resolution in far-field fluorescence microscopy. *Optics Letters*, *24*(14), 954–956. https://doi.org/10.1364/OL.24.000954

Kompa, J., Bruins, J., Glogger, M., Wilhelm, J., Frei, M. S., Tarnawski, M., D'Este, E., Heilemann, M., Hiblot, J., & Johnsson, K. (2023). Exchangeable HaloTag Ligands for Super-Resolution

Fluorescence Microscopy. *Journal of the American Chemical Society*, *145*(5), 3075–3083. https://doi.org/10.1021/jacs.2c11969

Liu, S., Hoess, P., & Ries, J. (2022). Super-Resolution Microscopy for Structural Cell Biology. *Annual Review of Biophysics*. https://doi.org/10.1146/annurev-biophys-102521-112912

Long, J. C., & Caceres, J. F. (2008). The SR protein family of splicing factors: Master regulators of gene expression. *Biochemical Journal*, *417*(1), 15–27. https://doi.org/10.1042/BJ20081501

Metkar, M., Ozadam, H., Lajoie, B. R., Imakaev, M., Mirny, L. A., Dekker, J., & Moore, M. J. (2018). Higher-Order Organization Principles of Pre-translational mRNPs. *Molecular Cell*, *72*(4), 715-726.e3. https://doi.org/10.1016/j.molcel.2018.09.012

Oleksiievets, N., Sargsyan, Y., Thiele, J. C., Mougios, N., Sograte-Idrissi, S., Nevskyi, O., Gregor, I., Opazo, F., Thoms, S., Enderlein, J., & Tsukanov, R. (2022). Fluorescence lifetime DNA-PAINT for multiplexed super-resolution imaging of cells. *Communications Biology*, *5*(1), 1–8. https://doi.org/10.1038/s42003-021-02976-4

Pacheco-Fiallos, B., Vorländer, M. K., Riabov-Bassat, D., Fin, L., O'Reilly, F. J., Ayala, F. I., Schellhaas, U., Rappsilber, J., & Plaschka, C. (2023). mRNA recognition and packaging by the human transcription–export complex. *Nature*, *616*(7958), 828–835. https://doi.org/10.1038/s41586-023-05904-0

Pühringer, T., Hohmann, U., Fin, L., Pacheco-Fiallos, B., Schellhaas, U., Brennecke, J., & Plaschka, C. (2020). Structure of the human core transcription-export complex reveals a hub for multivalent interactions. *eLife*, *9*, e61503. https://doi.org/10.7554/eLife.61503

Reinhardt, S. C. M., Masullo, L. A., Baudrexel, I., Steen, P. R., Kowalewski, R., Eklund, A. S., Strauss, S., Unterauer, E. M., Schlichthaerle, T., Strauss, M. T., Klein, C., & Jungmann, R. (2023). Ångström-resolution fluorescence microscopy. *Nature*, *617*(7962), Article 7962. https://doi.org/10.1038/s41586-023-05925-9

Rothemund, P. W. K. (2006). Folding DNA to create nanoscale shapes and patterns. *Nature*, *440*(7082), Article 7082. https://doi.org/10.1038/nature04586

Rust, M. J., Bates, M., & Zhuang, X. (2006). Sub-diffraction-limit imaging by stochastic optical reconstruction microscopy (STORM). *Nature Methods*, *3*(10), 793–796. https://doi.org/10.1038/nmeth929

Sahl, S. J., Matthias, J., Inamdar, K., Khan, T. A., Weber, M., Becker, S., Griesinger, C., Broichhagen, J., & Hell, S. W. (2023). *Direct optical measurement of intra-molecular distances down to the Ångström scale* (p. 2023.07.07.548133). bioRxiv. https://doi.org/10.1101/2023.07.07.548133

Sasaki, H. M., Kishi, J. Y., Wu, C., Beliveau, B. J., & Yin, P. (2022). *Quantitative multiplexed imaging of chromatin ultrastructure with Decode-PAINT* (p. 2022.08.01.502089). bioRxiv. https://doi.org/10.1101/2022.08.01.502089

Sau, A., Schnorrenberg, S., Huang, Z., Bandyopadhyay, D., Sharma, A., Gürth, C.-M., Dave, S., & Musser, S. M. (2025). Overlapping nuclear import and export paths unveiled by two-colour MINFLUX. *Nature*, *640*(8059), 821–827. https://doi.org/10.1038/s41586-025-08738-0

Schlichthaerle, T., Strauss, M. T., Schueder, F., Auer, A., Nijmeijer, B., Kueblbeck, M., Jimenez Sabinina, V., Thevathasan, J. V., Ries, J., Ellenberg, J., & Jungmann, R. (2019). Direct Visualization of Single Nuclear Pore Complex Proteins Using Genetically-Encoded Probes for

DNA-PAINT. *Angewandte Chemie International Edition*, *58*(37), 13004–13008. https://doi.org/10.1002/anie.201905685

Schmied, J. J., Raab, M., Forthmann, C., Pibiri, E., Wünsch, B., Dammeyer, T., & Tinnefeld, P. (2014). DNA origami–based standards for quantitative fluorescence microscopy. *Nature Protocols*, *9*(6), Article 6. https://doi.org/10.1038/nprot.2014.079

Schnitzbauer, J., Strauss, M. T., Schlichthaerle, T., Schueder, F., & Jungmann, R. (2017). Super-resolution microscopy with DNA-PAINT. *Nature Protocols*, *12*(6), Article 6. https://doi.org/10.1038/nprot.2017.024

Schueder, F., Lara-Gutiérrez, J., Beliveau, B. J., Saka, S. K., Sasaki, H. M., Woehrstein, J. B., Strauss, M. T., Grabmayr, H., Yin, P., & Jungmann, R. (2017). Multiplexed 3D super-resolution imaging of whole cells using spinning disk confocal microscopy and DNA-PAINT. *Nature Communications*, *8*(1), Article 1. https://doi.org/10.1038/s41467-017-02028-8

Schueder, F., Rivera-Molina, F., Su, M., Marin, Z., Kidd, P., Rothman, J. E., Toomre, D., & Bewersdorf, J. (2024). Unraveling cellular complexity with transient adapters in highly multiplexed super-resolution imaging. *Cell*, *187*(7), 1769-1784.e18. https://doi.org/10.1016/j.cell.2024.02.033

Schueder, F., Stein, J., Stehr, F., Auer, A., Sperl, B., Strauss, M. T., Schwille, P., & Jungmann, R. (2019). An order of magnitude faster DNA-PAINT imaging by optimized sequence design and buffer conditions. *Nature Methods*, *16*(11), Article 11. https://doi.org/10.1038/s41592-019-0584-7

Shaib, A. H., Chouaib, A. A., Imani, V., Chowdhury, R., Georgiev, S. V., Mougios, N., Monga, M., Reshetniak, S., Mihaylov, D., Chen, H., Fatehbasharzad, P., Crzan, D., Saal, K.-A., Trenkwalder, C., Mollenhauer, B., Outeiro, T. F., Preobraschenski, J., Becherer, U., Moser, T., … Rizzoli, S. O. (2022). *Expansion microscopy at one nanometer resolution* (p. 2022.08.03.502284). bioRxiv. https://doi.org/10.1101/2022.08.03.502284

Sharonov, A., & Hochstrasser, R. M. (2006). Wide-field subdiffraction imaging by accumulated binding of diffusing probes. *Proceedings of the National Academy of Sciences*, *103*(50), 18911–18916. https://doi.org/10.1073/pnas.0609643104

Singer, R. H., & Ward, D. C. (1982). Actin gene expression visualized in chicken muscle tissue culture by using in situ hybridization with a biotinated nucleotide analog. *Proceedings of the National Academy of Sciences*, *79*(23), 7331–7335. https://doi.org/10.1073/pnas.79.23.7331

Singh, G., Pratt, G., Yeo, G. W., & Moore, M. J. (2015). The Clothes Make the mRNA: Past and Present Trends in mRNP Fashion. *Annual Review of Biochemistry*, *84*, 325–354. https://doi.org/10.1146/annurev-biochem-080111-092106

Stoldt, S., Maass, F., Weber, M., Dennerlein, S., Ilgen, P., Gärtner, J., Canfes, A., Schweighofer, S. V., Jans, D. C., Rehling, P., & Jakobs, S. (2025). Super-resolution microscopy of mitochondrial mRNAs. *Nature Communications*, *16*(1), 6391. https://doi.org/10.1038/s41467-025-61577-5

Strauss, S., & Jungmann, R. (2020). Up to 100-fold speed-up and multiplexing in optimized DNA-PAINT. *Nature Methods*, *17*(8), Article 8. https://doi.org/10.1038/s41592-020-0869-x

Uno, S., Kamiya, M., Yoshihara, T., Sugawara, K., Okabe, K., Tarhan, M. C., Fujita, H., Funatsu, T., Okada, Y., Tobita, S., & Urano, Y. (2014). A spontaneously blinking fluorophore based on

intramolecular spirocyclization for live-cell super-resolution imaging. *Nature Chemistry*, *6*(8), Article 8. https://doi.org/10.1038/nchem.2002

Unterauer, E. M., Boushehri, S. S., Jevdokimenko, K., Masullo, L. A., Ganji, M., Sograte-Idrissi, S., Kowalewski, R., Strauss, S., Reinhardt, S. C. M., Perovic, A., Marr, C., Opazo, F., Fornasiero, E. F., & Jungmann, R. (2024). Spatial proteomics in neurons at single-protein resolution. *Cell*, *187*(7), 1785-1800.e16. https://doi.org/10.1016/j.cell.2024.02.045

Wang, J., Zhang, Y., Zhang, T., Tan, W. T., Lambert, F., Darmawan, J., Huber, R., & Wan, Y. (2024). RNA structure profiling at single-cell resolution reveals new determinants of cell identity. *Nature Methods*, *21*(3), 411–422. https://doi.org/10.1038/s41592-023-02128-y

Watts, J. M., Dang, K. K., Gorelick, R. J., Leonard, C. W., Bess Jr, J. W., Swanstrom, R., Burch, C. L., & Weeks, K. M. (2009). Architecture and secondary structure of an entire HIV-1 RNA genome. *Nature*, *460*(7256), 711–716. https://doi.org/10.1038/nature08237

Wolff, J. O., Scheiderer, L., Engelhardt, T., Engelhardt, J., Matthias, J., & Hell, S. W. (2023). MINFLUX dissects the unimpeded walking of kinesin-1. *Science*, *379*(6636), 1004–1010. https://doi.org/10.1126/science.ade2650

Wu, T., Cheng, A. Y., Zhang, Y., Xu, J., Wu, J., Wen, L., Li, X., Liu, B., Dou, X., Wang, P., Zhang, L., Fei, J., Li, J., Ouyang, Z., & He, C. (2024). KARR-seq reveals cellular higher-order RNA structures and RNA–RNA interactions. *Nature Biotechnology*, *42*(12), 1909–1920. https://doi.org/10.1038/s41587-023-02109-8

Young, A. P., Jackson, D. J., & Wyeth, R. C. (2020). A technical review and guide to RNA fluorescence in situ hybridization. *PeerJ*, *8*. https://doi.org/10.7717/peerj.8806

Zaza, C., Joseph, M. D., Dalby, O. P. L., Walther, R. F., Kołątaj, K., Chiarelli, G., Pichaud, F., Acuna, G. P., & Simoncelli, S. (2025). Super-resolution imaging in whole cells and tissues via DNA-PAINT on a spinning disk confocal with optical photon reassignment. *Nature Communications*, *16*(1), 4991. https://doi.org/10.1038/s41467-025-60263-w

Zhang, J. X., Fang, J. Z., Duan, W., Wu, L. R., Zhang, A. W., Dalchau, N., Yordanov, B., Petersen, R., Phillips, A., & Zhang, D. Y. (2018). Predicting DNA hybridization kinetics from sequence. *Nature Chemistry*, *10*(1), Article 1. https://doi.org/10.1038/nchem.2877